Piraeus University of Applied Science

Department of Mechanical Engineering

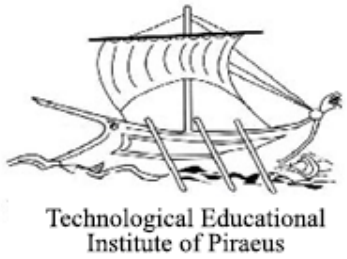

Simulation of Flow and CFD Predictions of Cavitation Inside Prototype Diesel Fuel Nozzles

Achilleas Pappas

January 2016

Abstract

This thesis discusses the prediction and the analysis of cavitation inside prototype diesel fuel nozzles. Several prototype nozzles were constructed based on a standard model and later on, a CFD model for each nozzle was created, with the aid of commercial software.

Standard CFD models and equations were used, provided by the used software. The model selection focused on achieving good accuracy by using the less possible computer power. In addition, the main focus was given in the mesh construction, as it was considered to be the most vital part for accurate CFD prediction. Although, there is a noticeable difference between the initial simulations compared to the latest ones in mesh quality, the mesh is considered good enough to achieve acceptable results even at the initial cases.

The main goal of each nozzle was to eliminate cavitation that occurred on the first model. The main model developed cavitation due to its geometry, as the fluid had to follow a steep change at its direction. Thus, several bypass tubes were introduced, between the area of cavitation and a higher pressure area, to eliminate cavitation inception.

However, none of the used alternative geometries were able to eliminate cavitation inception at the point of interest. Also, in one of the final cases, it was found, that a chocked flow was developed which is the main reason that all of the cases failed to achieve its goal.

Table of Content

Abstract 2
Table of Content 3
Part I: Literature Review 6
1 Fluid Mechanics 7
1.1 Introduction 7
1.2 Control Volume 8
1.2.1 Conservation of Mass (Continuity Equation) 8
1.2.2 Conservation of Momentum 9
1.2.3 Conservation of Energy (Bernoulli's Equation) 11
1.3 Flow Types 13
1.3.1 Laminar Flow 13
1.3.2 Turbulent Flow 13
1.3.3 Transient Flow 13
1.4 Condition of Flow 14
1.4.1 Steady Flow 14
1.4.2 Unsteady Flow 14
1.5 Flow Trajectory 14
1.5.1 Streamlines 14
1.5.2 Pathlines 16
1.5.3 Streaklines 16
1.6 Flow Numbers 17
1.6.1 Reynolds Number 17
1.6.2 Schmidt Number 17
1.6.3 Péclet number 18
1.7 Boundary Layer 18
1.7.1 Displacement Thickness 19
1.7.2 Boundary Layer Flow 20
2 The Physical Phenomenon of Cavitation 21
2.1 Introduction 21
2.2 Phase Transformation 21
2.3 Forms of Vapor Cavities 22
2.3.1 Sheet Cavities 22
2.3.2 Transient Isolated bubbles 22

2.3.3 Cavitating Vortices 22
2.4 Cavitation Nuclei 22
2.4.1 Liquid - Vapor Interfaces 23
2.4.2 Equilibrium of a Nucleus 23
2.4.3 Nucleus Evolution 25
2.5 Rayleigh - Plesset Equation 25
2.6 Heat and Mass Diffusion on Cavitation 28
2.6.1 Thermal Effect on Nuclei 28
2.6.2 Gas Diffusion 29
2.7 Cavitation Inception 30
2.8 Bubble Collapse 31
2.8.1 Speed of collapse 31
2.8.2 Pressure Field 33
2.8.3 Shape Distortion near a Surface 34
2.8.4 Cavitation Damage 36
3 Computational Fluid Dynamics 37
3.1 Introduction 37
3.2 Conservation Equations 38
3.3 Finite Volume Solvers 39
3.3.1 Finite Difference Method (FDM) 39
3.3.2 Finite Element Method (FEM) 40
3.3.3 Finite Volume Method (FVM) 41
3.4 Turbulence Modeling 46
3.4.1 RANS-based Models 47
3.4.2 Large Eddy Simulations 55
3.5 Multiphase Modeling 55
3.5.1 Mixture Model 55
3.5.2 Eulerian Model 56
3.5.3 VOF Model 56
3.6 Meshing 56
3.6.1 Cell Shapes 57
3.7 Mesh Quality 58
3.7.1 Near Wall Modeling 58
3.7.2 Skewness 60
3.7.3 Aspect Ratio 60

3.7.4 Smoothness 61
Part II: Experimental Procedure 62
4 Geometry Review 63
4.1 Control Volume 64
5 Solver Setup 65
Part III: Results Overview 69
6 Results 70
6.1 Case I: Single Hole 70
6.1.1 Geometry Overview 70
6.1.2 Mesh Overview 70
6.1.3 Results 71
6.2 Case II: Single Bypass 73
6.2.1 Geometry Overview 73
6.2.2 Mesh Overview 73
6.2.3 Results 74
6.3 Case III: Single Bypass (Short) 76
6.3.1 Geometry Overview 76
6.3.2 Mesh Overview 77
6.3.3 Results 77
6.4 Case IV: Triple Bypass (Short) 79
6.4.1 Geometry Overview 79
6.4.2 Mesh Overview 80
6.4.3 Results 80
6.5 Case V: Triple Bypass (Wide) 82
6.5.1 Geometry Overview 82
6.5.2 Mesh Overview 83
6.5.3 Results 83
7 Conclusion 89
References 91
Documentation 93

Part I:
Literature Review

1 Fluid Mechanics

1.1 Introduction

A fluid, by definition is a substance that continually deforms under an applied force. Generally, the word "fluid" refers both at liquid, gas and plasma material phases, although it is more commonly used to describe the liquid phase of a material. Fluids are characterized by viscosity, a feature that can be found especially at fluids, which describes the "ability" of a fluid to flow. Gas and liquid phases can be separated by the deference of the viscosity on each material phase. Generally, gases tend to have viscosity of lower scale compared to fluids, as the resistance of deformation in a gas it's much smaller.

Fluid Mechanics is the study of a fluid, either in motion or at rest and its interaction with the surroundings such as boundaries, solid objects or other fluids (White, 2010). Fluid mechanics can be divided into two major branches, fluid statics that studies incompressible fluids at rest, and fluid dynamics that deals with fluids in a flow.

Fluid dynamics have a wide range of application which includes calculation of the forces generated by aerodynamics of a vehicle like an aircraft or a racing car, determining flow aspects at fluid grids such as water and fuel grids and generally prediction of the flow and its consequences in a system. The solution of fluid dynamics problems typically involves calculation fluids properties such as pressure, flow rate, temperature etc. as those are functions of space and time.

Research on fluid mechanics, dates back to 250 B.C. when Archimedes discovered the fundamental principles of hydrostatics and dynamics by discovering the buoyant force applied to an emerged solid. Around 120 B.C. Greek school at Alexandria attempted to construct hydraulic machinery. Later, at Middle Ages Islamic scientist Abu Rayhan Biruni (973-1048) and Al-Hazini (1115-1130), were the first to apply experimental methods in the field of fluid statics. Meanwhile, Banu Musa brothers introduced a number of automatic controls in fluid mechanics. At 17^{th} century, the major scientific research on fluid dynamics had already began by many eminent scientist such Evangellista Torricelli, Laude-Louis Navier, Blaise Pascal, Isaac Newton, Daniel Bernoulli, Leonhard Euler, George Strokes and many more, which discovered the fundamental principles of fluid dynamics and formed the field as we know it today.

1.2 Control Volume

Control Volume (CV) is either a finite fixed (Eulerian Type) or moving, attached to the fluid (Lagrangian type) volume, which is being used in fluid dynamics and thermodynamics (Anderson Jr., 2010). Control Volume's shape and placement, is highly depended of case's geometry as it is placed in a way that simplifies psychical laws, applied to fluid inside the volume.

At steady state a control volume is an area in which the mass and the energy[1] remain constant as the mass entering the CV is equal to the mass leaving the CV (Borgnakke, et al., 2008). Also, the surface enclosing the control volume is referred to as the control surface.

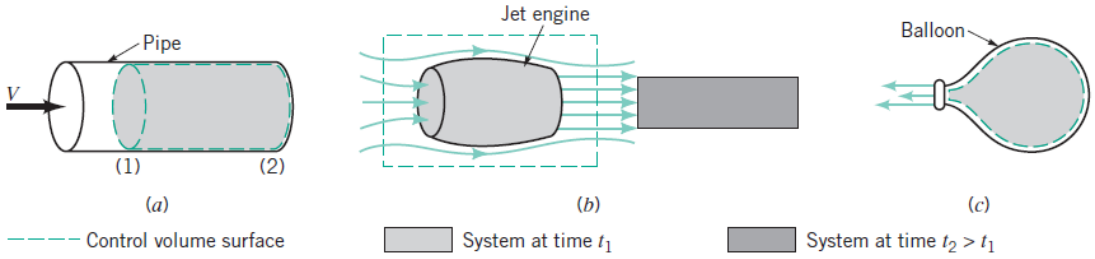

Figure 1.1 Typical CV examples: (a) fixed CV, (b) fixed or moving CV, (c) deforming CV

1.2.1 Conservation of Mass (Continuity Equation)

One of principles applied to a Control Volume is the mass conservation principle. In order to analyze that principle, a small region of a fixed control volume with area A and normal unit vector $\hat{n}$ has to be considered.

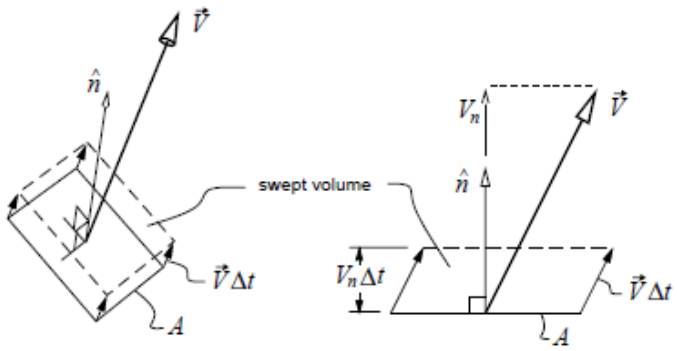

Figure 1.2 Small region of a Eulerian CV with normal unit vector $\hat{n}$

The plane of the fluid particles that are on the surface at time t, will move off the surface at time $t + \Delta T$, sweeping out a volume give by (Anderson Jr., 2010):

$$\Delta V = V_n A \Delta t \tag{1}$$

[1] The energy is considered steady in absence of heat transfers work

Also, the mass of the fluid passing though that volume is:

$$\Delta m = \rho \Delta V = \rho V_n A \Delta T \tag{2}$$

Thus, the mass flow rate is defined as the time rate of the mass described at equation (2) and the mass flux as the mass flow per area.

$$\begin{cases} \dot{m} = \lim\limits_{\Delta t \to 0} \dfrac{\Delta m}{\Delta t} = \rho V_n A & mass\ flow \\ \dfrac{\dot{m}}{A} = \rho V_n & mass\ flux \end{cases} \tag{3}$$

By applying the conservation of mass principle to an Eulerian control volume it is understandable that the mass flow into the CV is equal to the rate of mass coming in the volume. Using this relation:

$$\frac{d}{dt} \iiint \rho \, dV = - \oiint \rho \vec{V} \cdot \hat{n} \, dA \tag{4}$$

Considering the time derivative into the equation (4) and by using the Gauss' Theorem the following equation is formed:

$$\iiint \left[\frac{\partial \rho}{\partial t} + \nabla \cdot \left(\rho \vec{V} \right) \right] dV = 0 \tag{5}$$

Finally, by applying the equation (5) at every point in the flow, the whole quantity of the integral has to be equal to zero, which results to the renowned Continuity Equation (Anderson Jr., 2010).

$$\frac{\partial \rho}{\partial t} + \nabla \cdot \left(\rho \vec{V} \right) = 0 \tag{6}$$

The steady flow version of the Continuity Equation can be described as:

$$\nabla \cdot \left(\rho \vec{V} \right) = 0 \tag{7}$$

In the case of a low-speed flow, the density is considered constant and the equation (6) takes the simple form of the zero velocity vector field (Anderson Jr., 2010).

$$\nabla \cdot \vec{V} = 0 \tag{8}$$

1.2.2 Conservation of Momentum

According to Newton's second law of motion, when a force is applied into a mass that moves under the affect of the force, the momentum of the mass is changing.

$$\frac{d\vec{P}}{dt} = \vec{F} \tag{9}$$

Also, when a fluid is moving, it isn't carrying only mass along its path, but also momentum. The momentum carried across the flow is called momentum flow and is a vector function (Anderson Jr., 2010).

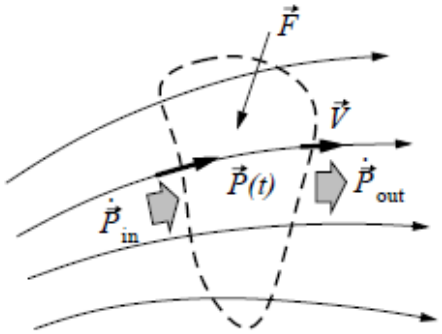

Figure 1.3 Momentum flow at a control volume

When the Newton's second law is applied an Eulerian type control volume, as seen in Figure 1.3, equation (9) evolves accordingly.

$$\frac{d\vec{P}}{dt} + \dot{\vec{P}}_{out} - \dot{\vec{P}}_{in} = \vec{F} \tag{10}$$

Both $\dot{\vec{P}}_{in}$ and $\dot{\vec{P}}_{out}$ terms are evaluated by the surface integral of the momentum flux over CV's boundary. Also, $\vec{P}$ term by definition is the instantaneous momentum inside the CV. Thus, the following parity eventuates.

$$\begin{cases} \vec{P}(t) = \iiint \rho\vec{V}\, dV \\ \dot{\vec{P}}_{out} - \dot{\vec{P}}_{in} = \oiint \rho(\vec{V}\cdot\hat{n})\, dA \end{cases} \tag{11}$$

By analyzing the forces acting on control volume, it is concluded that two types of forces are appearing. Body forces and surface forces (Anderson Jr., 2010).

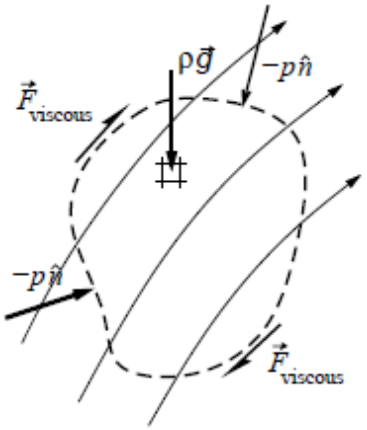

Figure 1.4 Forces acting on a control volume

Body forces, is acting upon fluid passing through the control volume. Most common case of that kind of force is the force due to gravitational acceleration. Surface forces are acting up the surface of the control volume. The last ones can be separated into pressure forces and viscous forces.

$$\begin{cases} \vec{F}_{gravity} = \iiint \rho \vec{g}\, dV \\ \vec{F}_{pressure} = \oiint -p\hat{n}\, dA \end{cases} \tag{12}$$

By substituting all (6)(10), (11) and (12) equations to Newton's second law equation (9), the Integral Momentum Equation is formed.

$$\frac{d}{dt}\iiint \rho\vec{V}\, dV + \oiint \rho(\vec{V}\cdot\hat{n})\, dA = \iiint \rho\vec{g}\, dV + \oiint -p\hat{n}\, dA + \vec{F}_{viscous} \tag{13}$$

All contour integrals terms in equation (13) can subjected to Gauss's Theorem and converted to line integrals. For example, pressure force integral can be transformed to :

$$\oiint -p\hat{n}\, dA = \iiint \nabla\cdot p\, dV \tag{14}$$

Also, vector quantities can be analyzed into a sum of three dimension elements. For example $\vec{V} = u\hat{\imath} + v\hat{\jmath} + w\hat{k}$.

In conclusion, by applying Gauss' Theorem, it is possible to analyze Integral Momentum Equation (13) into a differential form consisting of three equations for different vector. Including the viscous terms in the momentum balance the Navier Strokes equations derives (Bakker, 2006).

$$\frac{\partial(\rho u)}{\partial t} + \nabla\cdot\left(\rho u\vec{V}\right) = -\frac{\partial p}{\partial x} + \rho g_x + (F_x)_{viscous} \tag{15}$$

$$\frac{\partial(\rho v)}{\partial t} + \nabla\cdot\left(\rho v\vec{V}\right) = -\frac{\partial p}{\partial y} + \rho g_y + \left(F_y\right)_{viscous} \tag{16}$$

$$\frac{\partial(\rho w)}{\partial t} + \nabla\cdot\left(\rho w\vec{V}\right) = -\frac{\partial p}{\partial z} + \rho g_z + (F_z)_{viscous} \tag{17}$$

1.2.3 Conservation of Energy (Bernoulli's Equation)

Conservation of energy simply states, that inside a control volume the total energy at any given point is constant which means that the total energy of two points are equal following the first law of thermodynamics. As a matter of fact, conservation of energy theorem doesn't take into account thermal losses and losses due to friction which either takes place due to the viscosity of the liquid or as the fluid is in touch with other solid elements.

$$\begin{cases} \frac{1}{2}\rho u^2 & Kinematic\ energy \\ P & Pressure \\ gh & Dynamic\ energy \end{cases} \tag{18}$$

As a result, Bernoulli's equation is a sum of the total energy conserved at any point.

$$\frac{1}{2}\rho u^2 + P + gh = c \tag{19}$$

Bernoulli's equation is effective under the assumptions of a steady, low Mach number flow which is the case of an ideal fluid (Bakker, 2006).

Conservation of Internal Energy

Again, following the first law of thermodynamics, the rate of change of energy of a fluid particle is equal to the rate of heat addition plus the rate of work done. At this instance, potential energy e.g. gravitation, is treated separately and is included in the source term. By the term internal energy, is meant of the change in energy as a result of work done by viscous stresses and heat conduction subtracting the kinetic energy of the flow (Anderson Jr., 2010).

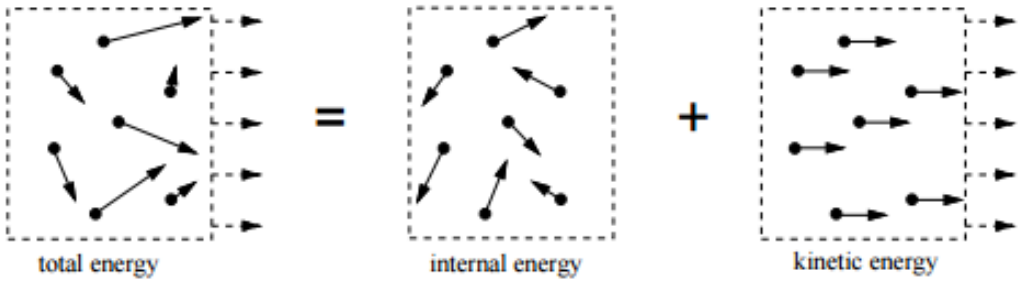

Figure 1.5 Total energy in a flow

Thus, the internal energy equation derives:

$$\frac{\partial(\rho i)}{\partial t} + \nabla \cdot (\rho i \mathbf{u}) = -p\,\nabla \cdot \boldsymbol{u} + \nabla \cdot (\mathrm{k}\nabla \mathrm{T}) + \Phi + S_i \tag{20}$$

Also, an alternative of the internal energy equation is used, expressed with the term enthalpy, giving the total enthalpy equation.

$$h_0\left[\frac{\partial p}{\partial t} + \nabla \cdot \left(\rho \vec{V}\right)\right] + \rho\left(\frac{\partial h_0}{\partial t} + \vec{V} \cdot \nabla \mathrm{h}_0\right) = \frac{\partial p}{\partial t} + \rho \dot{g} + p\vec{g} \cdot \vec{V} \tag{21}$$

Where, h_0 the total enthalpy expressed by:

$$h_0 = h + 1/2\,(u^2 + v^2 + w^2) = E + p/\rho$$

And h, specific enthalpy $h = i + p/\rho$

1.3 Flow Types

1.3.1 Laminar Flow

Laminar flow is the first stage of a flow and the simplest one. In laminar flow fluid's particles are moving in parallel layers with no lateral mixing. Any movement not parallel to the flow's direction is being absorbed by fluids viscous. Laminar flow tends to occur in lower velocities and is being highly depending of fluid's viscosity. Laminar flow is described by Newton's Law for viscosity which states that the shear stress is equal to dynamic viscosity times local share velocity (White, 2010).

$$\tau = \mu \frac{\partial u}{\partial y} \tag{22}$$

This equation states that shear stress among fluid's layers maximized when the local velocity is perpendicular to fluid's velocity.

1.3.2 Turbulent Flow

Turbulent flow is the most common case of flow as it occurs in random patterns. It is characterized by rapid variation of pressure and local flow velocities that are constantly change in space and time. Turbulent flow consists of large number of eddies and curls and most of the times it occurs at higher velocities.
As the nature of turbulent flow is completely random, it is hard to predict or being modeled[2]. However, the shear stress of turbulent flow can be calculated by an equation similar to Newton's law for viscosity (White, 2010).

$$\tau = (\mu + \varepsilon) \frac{\partial u}{\partial y} \tag{23}$$

The Greek letter ε represents the additional turbulence's resistance of movement.

1.3.3 Transient Flow

Transient flow is the transitional phase between laminar and turbulent flow. Transient flow triggers when the velocity of the fluid extends over a certain "triggering" limit. It consists of a small number of eddies that tend to increase over time which results in turbulent flow (White, 2010). Transient flow usually is considered as part of turbulent phase.

[2] Nobel Laureate Richard Feynman described turbulence as "the most important unsolved problem of classical physics".

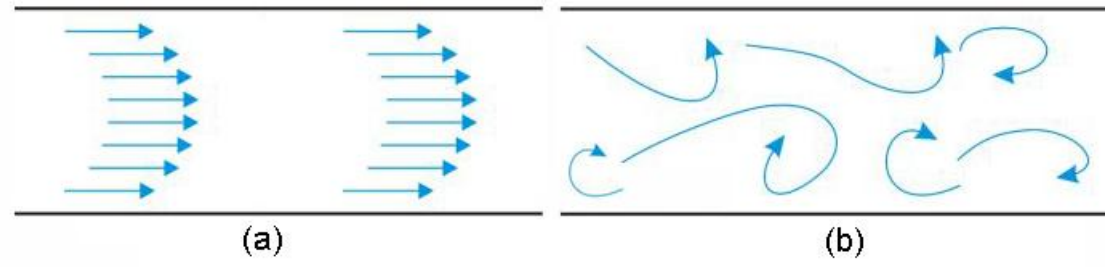

Figure 1.6 Flow Types: (a) Laminar flow, (b) Turbulent flow

1.4 Condition of Flow

1.4.1 Steady Flow

At a steady flow, the velocity at any given point in space does not vary in time. Laminar flows are most likely to be steady but in reality all flows are not steady at some sense. Although, the randomness of a turbulent flow, theoretically it can become steady if the velocity stays the same through time. The govern equations of steady problems have one dimension less (the dimension of time), thus partial derivative of time are equal to zero (Koronakis, 2009).

$$\frac{\partial \varrho}{\partial t} = 0\,, \qquad \frac{\partial \bar{V}}{\partial t} = 0, \qquad \frac{\partial P}{\partial t} = 0 \quad etc.$$

1.4.2 Unsteady Flow

An unsteady flow is the one that the velocity varies through time at, at least one point. By definition, turbulent flow is unsteady. In some flows, the unsteady element can be periodic but at most occasions the unsteady characteristic of a flow is completely random.

1.5 Flow Trajectory

Motion of fluid is characterized by three-dimensional movement into space. Although, at steady states, a flow is considered to be repetitive throw one dimension, in reality the flow is three-dimensional and a velocity vector field can be considered.

1.5.1 Streamlines

Streamlines, are theoretical curves, in a three-dimensional space. By assuming a flow with a velocity $\vec{u} = (u, v, w)$ and streamlines velocity $\vec{x}_s = (x_s, y_s, z_s)$, a streamline has to satisfy the following equation:

$$\frac{d\vec{x}_s}{ds} \times \vec{u}(\vec{x}_s) = 0 \tag{24}$$

Those curves tangent are parallel to fluid's local velocity at each applied point. By using streamlines, it is possible to observe the direction of a massless fluid particle at any given moment (Granger, 1995). A bundle of nearby, similar streamlines in a close loop constitute a stream tube.

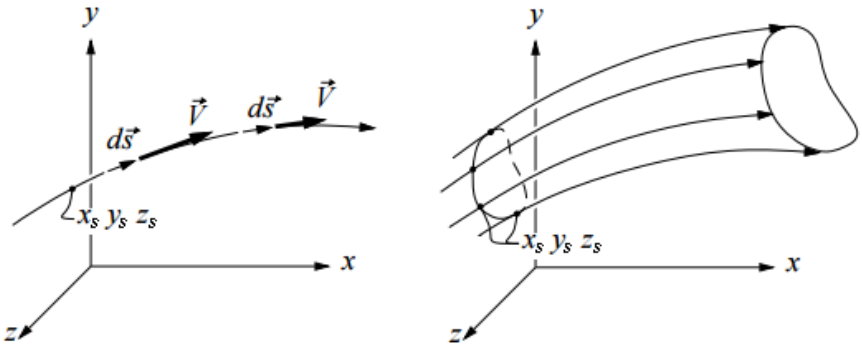

Figure 1.7 Streamline and stream tube in a 3D space

Euler's Equation along a Streamline

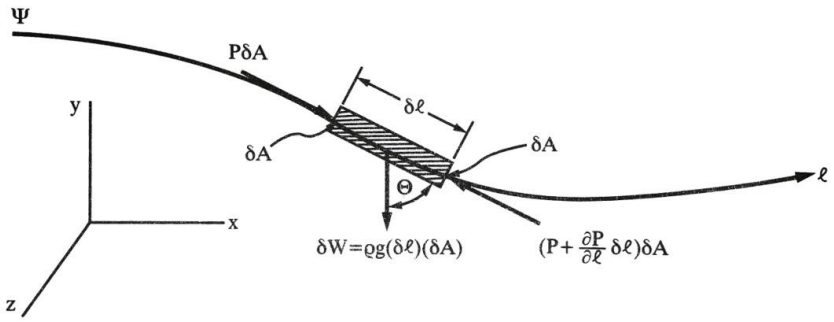

Figure 1.8 Analyses of a fluid element on a streamline

Euler's equation along a streamline derives by applying Newton's second law of motion (9) to a moving element along a streamline. Considering an element with length δl, section δA and the force of gravity as the only body force, the net force acting on the fluid element can be written as:

$$F_s = \frac{\partial p}{\partial l}\Delta l \Delta A - \rho \Delta l \Delta A g \cos\Theta \tag{25}$$

By applying Newton's second law in force's direction equation (25) derives:

$$\rho \Delta l \Delta A \frac{DV}{dt} = \frac{\partial p}{\partial l}\Delta l \Delta A - \rho \Delta l \Delta A g \cos\Theta \tag{26}$$

Also, by geometry:

$$\cos\Theta = \lim_{\Delta l \to 0} \frac{\Delta z}{\Delta l} = \frac{dz}{dl} \tag{27}$$

Thus, from equation (26), derives the Euler's equation along a streamline.

$$\frac{\partial V}{\partial t} + V\frac{\partial V}{\partial l} = -\frac{1}{\rho}\frac{\partial p}{\partial l} - g\frac{dz}{dl} \tag{28}$$

Considering $d\vec{s}$ as a three dimensional vector $d\vec{s} = \hat{\imath}\mathrm{dx} + \hat{\jmath}\mathrm{dy} + \hat{\mathrm{k}}\mathrm{dz}$ and by combining equation (28) and streamlines equation (24), the most popular form of Euler's equation derives, which has the velocity vector always directed along the streamline (White, 2010).

$$\rho\left[\frac{\partial V}{\partial t} + V\frac{\partial V}{\partial l}\right] = -\frac{\partial p}{\partial l} - \rho g\frac{dz}{dl} \tag{29}$$

1.5.2 Pathlines

Pathlines are the trajectories of independent fluid particles (Anderson Jr., 2010). In general, a pathline can be described as the path a fluid particles flows through space as a function of time. Pathlines are described by the following equation set:

$$\begin{cases} \dfrac{d\vec{x}_P}{dt} = \vec{u}_P(\vec{x}_p, t) \\ \vec{x}_P(t_0) = \vec{x}_{P0} \end{cases} \tag{30}$$

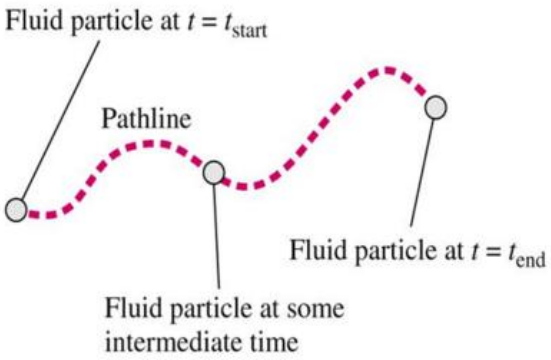

Figure 1.9 Fluid pathline

1.5.3 Streaklines

Streaklines are the loci of points of all fluid particles that have passed through a particular point inside the flow (Anderson Jr., 2010). Streaklines are commonly used to visualize flow trajectory at experiments by using color additives steadily injected at a point or by using special smoke derivatives inside wind tunnels. A streakline can be described by:

$$\begin{cases} \dfrac{d\vec{x}_P}{dt} = \vec{u}_P(\vec{x}_p, t) \\ \\ \vec{x}_P(t = \tau_P) = \vec{x}_{P0} \end{cases} \tag{31}$$

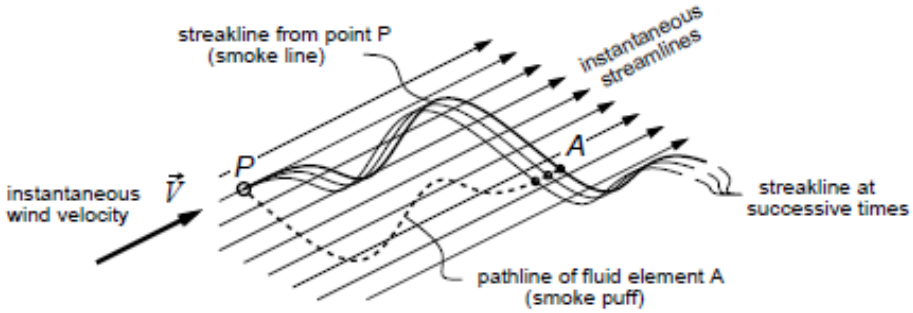

Figure 1.10 Streakline inside a wind tunnel

1.6 Flow Numbers

1.6.1 Reynolds Number

Reynolds number (Re) is a dimensionless quantity that indicates the type of the flow. It is expressed by the division of inertial forces by viscous forces.

$$Re = \frac{inertial\ forces}{viscous\ forces} = \frac{\rho u L}{\mu} = \frac{uL}{\nu} \tag{32}$$

Where L, is a characteristic linear dimension e.g. the travelled length of the fluid in the case of an open channel or the hydraulic diameter in a pipe system.
Critical Reynolds values have been found for most common cases as seen at Table 1.1. However, in practice, due to the chaotic nature of turbulent and transient flows, even the smallest change like in the surface roughness or the shape can result in a much different result in the flow. Thus, Reynolds number cannot be used as a sufficient method to determine the type of the flow but it is widely used (Fox, et al., 2005).

	Laminar Flow	Transient Flow	Turbulent Flow
Internal Flow	$Re \leq 3000$	$3000 \leq Re < 8000$	$Re > 8000$
External Flow	$Re \leq 2 \cdot 10^5$	$2 \cdot 10^5 \leq Re < 5 \cdot 10^5$	$Re > 5 \cdot 10^5$

Table 1.1 Flow type according to Reynolds number

1.6.2 Schmidt Number

Schmidt number is a dimensionless number that defines the relation between the viscosity (momentum diffusivity) and mass diffusivity. Physically, it relates the relative thickness of the hydrodynamic layer compared to mass-transfer boundary layer.

$$Sc = \frac{viscous\ diffusion\ rate}{mass\ diffusion\ rate} = \frac{\nu}{D} = \frac{\mu}{\rho D} \tag{33}$$

Where D the mass diffusivity rate. Also, there is the turbulent Schmidt number, which describes the ration of the rates of turbulent transport of momentum and the turbulent transport of mass (Bergman, et al., 2011).

$$Sc_t = \frac{eddy\ viscosity}{eddy\ diffusivity} = \frac{v_t}{K} \tag{34}$$

1.6.3 Péclet number

Péclet number is a dimensionless number expressing the ration of the rate of advection of a physical quantity by the flow to the rate of diffusion of the same quantity driven by an appropriate gradient (Bergman, et al., 2011)

$$Pe = \frac{advective\ transport\ rate}{diffusive\ transport\ rate} = \frac{uL}{D} = Re \cdot Sc \tag{35}$$

When Péclet number is high, something usual for common applications, the dependency of the flow upon downstream locations is diminished. In such way, variables of the flow tend to become properties with a single direction. Thus, simpler computational models can be used (Patankan, 1980).

1.7 Boundary Layer

The boundary layer is a fundamental part in a flow and has a very important part in fluid dynamics. When a fluid flows over an object e.g. a plate, an airfoil or a cylinder, the layer of the fluid that flows over the object surface has a reduced velocity due to friction as it is in touch with the surface. Thus, upper fluid layers have a reduced velocity too, due to inertia. As a result, while the distance from the surface is increased, layers velocity tends to become equal to fluids velocity.

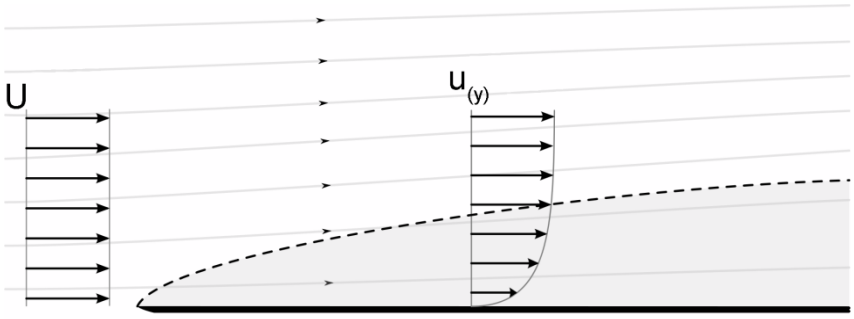

Figure 1.11 Boundary layer over a plate

The boundary layer thickness is defined as the distance from the surface at which the fluid velocity is approximately the same as the upstream velocity, typically where $u = 0.99U$ (Young, et al., 2010).

1.7.1 Displacement Thickness

In order to make boundary layer analysis simpler, the term displacement thickness has been introduced. To remodel the boundary layer from a parabola shape to a rectangular one like an inviscid flow, an increased thickness has to be applied to keep the flow rate the same as seen in Figure 1.12. A result like this can be achieved by displacing the plate below the boundary layer. Considering the plate's thickness equal to b:

$$\delta^* bU = \int_0^\infty (U-u)b\,dy$$

$$\Rightarrow \delta^* = \int_0^\infty \left(1-\frac{u}{U}\right) dy \tag{36}$$

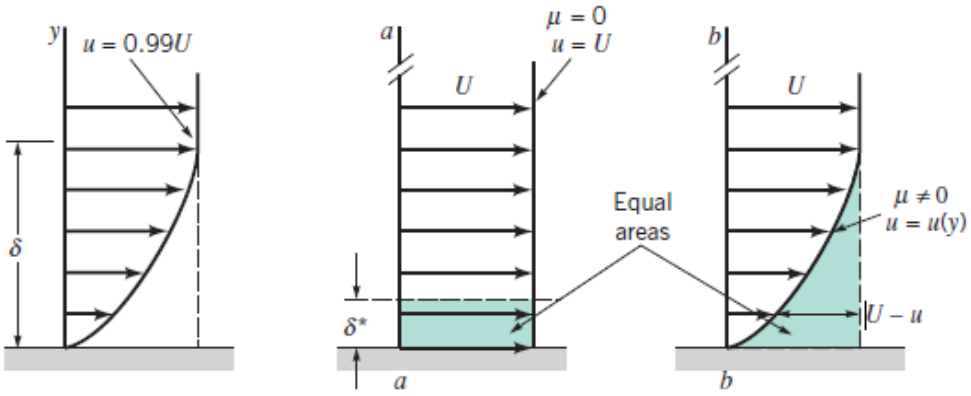

Figure 1.12 Boundary layer thickness: (a) standard boundary, (b) boundary layer displacement thickness

The main reason of boundary layer existence is the viscosity which results in inertia at different sections of the fluid. In general, the thickness of the boundary layer tends to be smaller when the viscosity is lower or when the Reynolds number of the flow is higher. In higher Re flows inertia forces outclass the friction forces, thus the affect of viscosity is negligible and the continuum equations can be solved considering a non viscous flow ($\mu = 0$) (Koronakis, 2001).

1.7.2 Boundary Layer Flow

Boundary layer consists, not only with a laminar phase of flow, but also a turbulent one. After travelling a critical length the flow transits to a turbulent phase, similar to the one described in chapter 1.3.2 which consists of eddies of random size and direction. The transition occurs with a transient flow phase and at the same values as mentioned in Table 1.1. However as turbulent flow is too irregular, a sufficient critical length value cannot be calculated with acceptable precision.

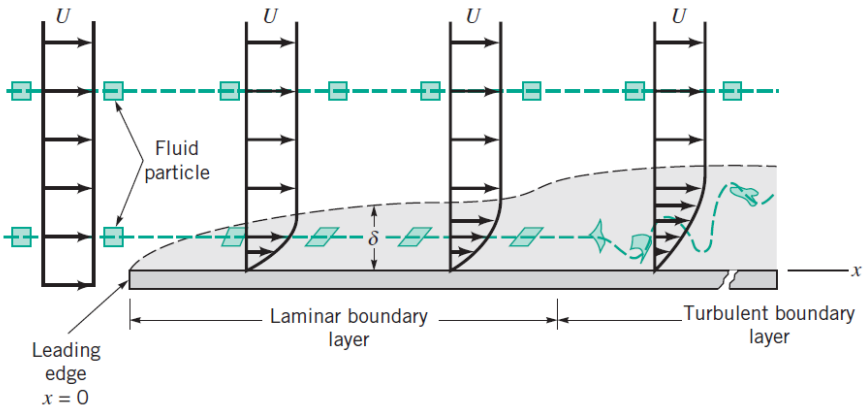

Figure 1.13 Boundary layer over a plate

After laminar phase, due to swirls that occur, the random transportation of momentum and matter from a layer to another, results to an exponential grow of the sublayer (Koronakis, 2001).

Lastly, at the bottom of boundary element, there is a laminar sublayer that also called viscous sublayer. Viscous sublayer extends for less than a millimeter. In this area, viscous forces are large enough to absorb any movement not parallel to flows direction and keep a laminar flow steady.

2 The Physical Phenomenon of Cavitation

2.1 Introduction

Cavitation is the phenomenon of appearance, of bubble vapor inside a liquid medium. It is a significant cause of wear at various engineering contexts causing surface fatigue as a result of collapsing bubbles at the surface of the object. Most common examples due to cavitation are at pumps, fuel injectors, impellers, propellers and control valves (Franc, 2008).

Cavitation was introduced by Osborne Reynolds in 1894 who contacted the experiment of a fluid moving through a venture tube. Bernoulli's equation states that the pressure is decreased when the velocity of the flow increases, this at high flow rates, the liquid in the throat begins to spawn bubbles.

2.2 Phase Transformation

Cavitation is a phenomenon similar to boiling. It occurs when a liquid is subjected to a rapid change of pressure caused by external forces acting on the fluid or by the flow's geometry. In general, voids spawn due to high local flow velocity.

In most cases, only a small amount of heat is required for formation of vapor. Thus, the medium (liquid) shows only a slightly difference in temperature after the formation of the vapor and the phase transformation is practically isothermal. The difference (see Figure 2.1) in temperature before and after the formation of the vapor is called thermal delay (Franc, et al., 2005).

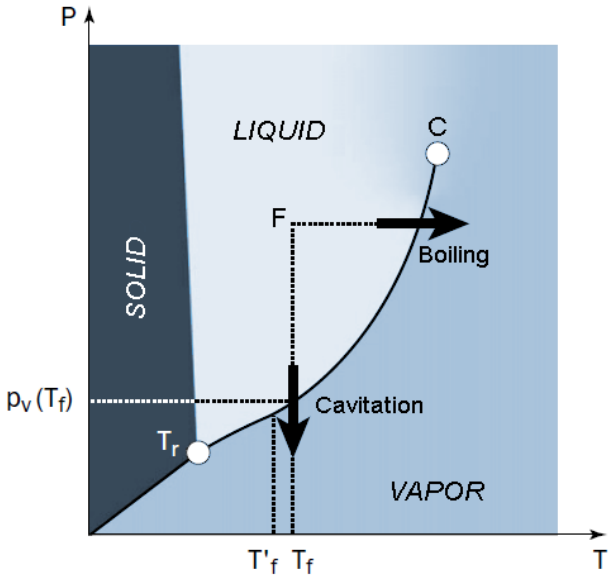

Figure 2.1 Phase Diagram

Furthermore, it is worth mentioning that in almost static conditions, cavitation might occur at pressures lower than critical values.

2.3 Forms of Vapor Cavities

2.3.1 Sheet Cavities

Sheet or attached cavitation is a region of vapor which remains at the same region of the body and it attached over it. This type of cavitation is formed as a result of pressure drop due to body's geometry and often incept at the leading edge of the body(Kuiper, 2012).

2.3.2 Transient Isolated bubbles

This type of vapor cavities appears in a region of low pressure as a result of the rapid growth of tiny air nuclei contained in the fluid. Most of the times the cavities are carried alongside the flow tend to disappear when the local area pressure is above critical levels (Franc, et al., 2005).

2.3.3 Cavitating Vortices

Cavitation vortices appear in the low-pressure core of vortices in turbulent wakes or in tip vortices of propeller blades and foils (Franc, et al., 2005). However, such type of cavitation is not erosive it can produce noise which are a significant subject for ship detection and military applications. The dynamics of cavitating tip vortices are not yet understood completely. Also, tip vortices are an important issue for model testing because they are strongly depended from Reynolds number(Kuiper, 2012).

2.4 Cavitation Nuclei

Every fluid and material in particular, consist various structure defects. In fluids structure defects come in form of tiny spherical bubbles which are called cavitation nuclei and have a great importance in cavitation inception as they are the triggering points of it. Nuclei radius ranges from a few to several hundred micrometers. Despite the small size, nuclei can hold together due to surface tension (S).

Those bubbles are formed by small gas and vapor inclusions. They can be found either on surface of the fluid which are produced by gas trapped in small wall crevices, or in a bulk form inside the liquid that are produced by a various mechanisms of energy disposition. However, the most effective way to produce nuclei is by increasing the pressure at a saturated liquid.

Once nuclei are presented in the liquid, they can evolve by two ways. Firstly, free nuclei that are not attached to a wall are being rise due to buoyancy. Secondly, all nuclei are subjected to gas diffusion with the dissolved gasses presented in the surrounded liquid. Diffusion time is nearly a second and is considered large, compared a bubble collapse which takes milliseconds.

The void from the presence of nuclei is typically small and does not affect liquids density or sound speed. Roughly the void fraction is calculated at $0.52 \cdot 10^{-4}$ for a boosted number of nuclei per unit volume (Franc, et al., 2005).

2.4.1 Liquid - Vapor Interfaces

Cavitation flows, like other two-phase liquid-gas flow, are characterized by the presence of various interfaces. However, the nature of the cavitation results in a much different behavior when the medium is under external perturbations as cavitation vapor is a pretty unstable phenomenon and can collapse or incept under certain conditions like a pressure alteration. Furthermore, the density of the two-phase flow is altered significantly for to the same reason.

Concerning the exchange between vapor and liquid, the mass flowrate across the interface is proportional to the normal velocities of either liquid or vapor, relative to the interface. Mass convention law across the interface results in the equation (37) (37)[3].

$$\dot{m} = \rho_l \left(V_{ln} - \frac{dn}{dt} \right) = \rho_v \left(V_{vn} - \frac{dn}{dt} \right) \tag{37}$$

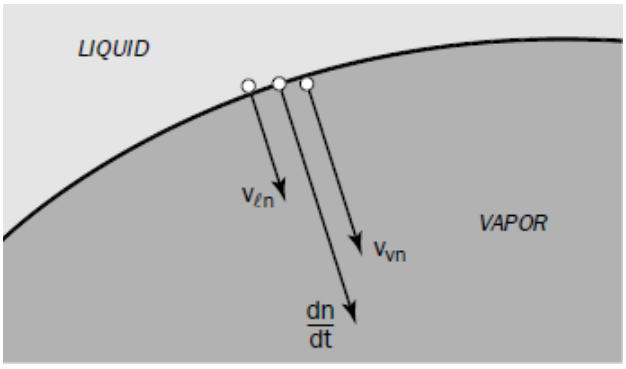

Figure 2.2 The liquid - vapor interface

By assuming that the mass flowrate between the interface in negligible[4] the three normal velocities are of equal size and the interface is usually a material surface made of the same fluid particles at different instants.

For spherical bubbles whose radius (R) is a function of time, the normal velocity of the interface is equal to dR/dt and in the case of $\dot{m} = 0$ all normal velocities are equal. Also, in the case of a study cavity which is surrounded by a flowing liquid the normal velocity of the interface is equal to zero and in the case of $\dot{m} = 0$ the normal velocities of both liquid and vapor are also zero. Thus, the liquid the velocity of the liquid of the outside flow is tangential to the cavity wall (Franc, et al., 2005).

2.4.2 Equilibrium of a Nucleus

By considering a small enough nucleus in order to consider negligible the hydrostatic pressure $P = 2\rho g R$ compared to the pressure difference corresponding to the surface tension $2S/R$ the radius of the nucleus must not be larger than $\sqrt{S/\rho g}$.

[3] Symbol dn/dn refers to the normal velocity of the interface.
[4] Mass flowrate between vapor and liquid phases equal to zero, is an assumption that is usually made.

Thus, outer nucleus pressure has to be equal the inner pressure minus pressure corresponding to the surface tension:

$$p_{\infty} = p_g + p_v - \frac{2S}{R} \tag{38}$$

However, nucleus may be subjected into small perturbations which have to be taken into account when calculating the radius. The radius ranges from $R' = R$ to $R' = R(1+\varepsilon)$[5] . Also, equation (38) is subjected to the phenomena of heat transfer and gas diffusion at the interface, so the pressure change has to be fast enough to ensure that gas diffusion is negligible and the mass of gas constant. At the same time, the transformation has to be isothermal, so the pressure change speed has to be slow enough to allow the heat to transfer between liquid and vapor (Brennen, 2005).

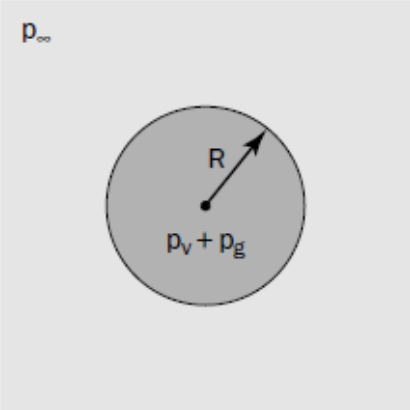

Figure 2.3 Nucleus Equilibrium

Considering that in isothermal transformations, the gas pressure is inversely proportional to the volume the equation (38), in relation with the initial state (denoted by subscript 0) can be written as follows:

$$p_{\infty 0} = p_{g0}\left[\frac{R_0}{R}\right]^3 + p_v - \frac{2S}{R} \tag{39}$$

By solving the equation (39), two mechanisms can be recognized. Firstly, the bubble size tends to increase due the internal pressure of the bubble. Secondly, surface tension effect can result in a minimum pressure of the nucleus. Acknowledging that a nucleus, in a gas-liquid fluid, is characterized by the mass of gas, which is assumed constant, a critical value of liquid pressure can be specified that will allow computation of bubble radius (Franc, 2006). Thus, defining a nucleus can be done by referring to critical values of radius and pressure of the liquid. Those critical values are given by (Brennen, 2005):

[5]Parameter ε is significantly small, $\varepsilon \ll 1$.

$$\begin{cases} R_c = R_0 \sqrt{\dfrac{3p_{g0}}{2S/R_0}} \\ p_c = p_v - \dfrac{4S}{3R_c} \end{cases} \tag{40}$$

2.4.3 Nucleus Evolution

Critical values of pressure and radius described at section 2.4.2 represents a remarkable feature. As can be seen in Figure 2.4 which shows a graph of critical values of pressure and radius, two sections can be mentioned.

The first one is at the left of critical radius. At this part, equilibrium is stable. If a pressure change occurs, the nucleus radius will grow or decline accordingly and a new equilibrium will be reached.

In the other hand, when the nucleus is larger than the critical value, the equilibrium is unstable and every variation in pressure will result in an indefinitely growth of the nuclei without reaching a new equilibrium, which will result in the formation of a cavitation bubble. If the applied pressure p_∞ is lower than the critical pressure p_c, the nucleus is destabilized and becomes a macroscopic bubble (Franc, 2006).

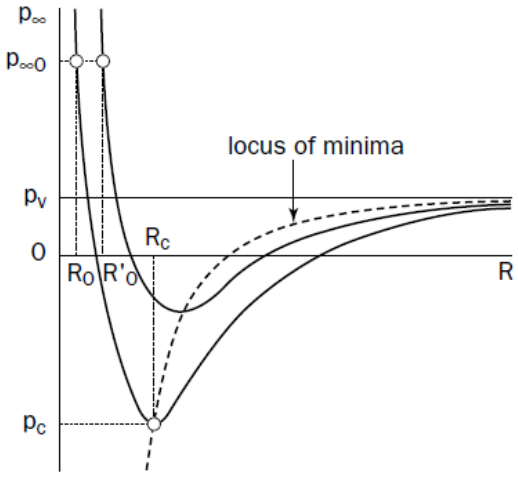

Figure 2.4 Spherical nucleus critical values

2.5 Rayleigh - Plesset Equation

The Rayleigh – Plesset equation is a differential equation which governs the dynamics of a spherical bubble inside a liquid medium. It was introduced by John Strutt, 3rd Baron Rayleigh in 1917 and was applied by Milton Plesset in 1949 on travelling cavitation bubbles (Brennen, 1995). The Rayleigh – Plesset Equation is derived from Navier – Stocks equation under assumption of spherical symmetry. In general, it is a widely used equation in fluid dynamics field and is often used to describe the time-varying bubble radius.

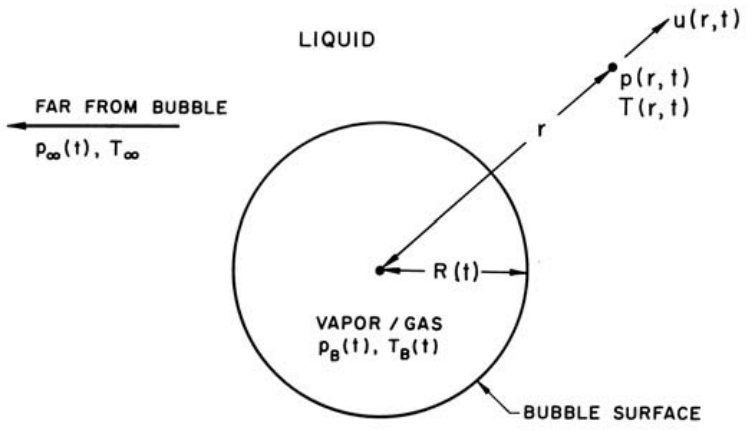

Figure 2.5 Spherical bubble in a liquid

By considering a bubble with homogenous contest of pressure$P_B(t)$, temperature $T_B(t)$ and radius $R(t)$, in a liquid with a controlled pressure $P_\infty(t)$, constant density ρ_L and temperature T_∞, without considering the temperature gradient, conservation of mass dictates, for a point of distance r of bubbles center, that :

$$u(t,r) = \frac{F(t)}{r^2} \tag{41}$$

Where $F(t)$ is related to bubbles radius by a kinematic boundary condition of bubbles surface, in the case of zero mass transfer across the interface, as seen in equation (42).

$$F(t) = R^2 \frac{dR}{dt} \tag{42}$$

Even when evaporation is occurring at the interface, the rate of bubble volume increase should be equal to the volume rate of vapor production. Therefore, by considering the saturated vapor density ρ_V[6] at temperature T_B, the mass rate of evaporation is equal to the mass flow of liquid inward relative to the interface.

$$u(R,t) = \frac{dR}{dt} - \frac{\rho_V(T_B)}{\rho_L}\frac{dR}{dt} = \left[1 - \frac{\rho_V(T_B)}{\rho_L}\right]\frac{dR}{dt} \tag{43}$$

$$F(t) = \left[1 - \frac{\rho_V(T_B)}{\rho_L}\right] R^2 \frac{dR}{dt} \tag{44}$$

Navier-Stokes equation for motion in r direction for a Newtonian liquid is given by:

$$-\frac{1}{\rho_L}\frac{\partial p}{\partial r} = \frac{\partial u}{\partial t} + u\frac{\partial u}{\partial r} - \nu_L\left[\frac{1}{r^2}\frac{\partial}{\partial r}\left(r^2\frac{\partial u}{\partial r}\right) - \frac{2u}{r^2}\right] \tag{45}$$

[6] It is worth mention that in most cases, the saturated vapor density is much smaller compared to the liquid density, $\rho_L \gg \rho_V$, therefore the equation (42) can be(43) adequate.

Knowing that $u = F(t)/r^2$ equation (45) becomes:

$$-\frac{1}{\rho_L}\frac{\partial p}{\partial r} = \frac{1}{r^2}\frac{dF}{dt} - \frac{2F^2}{r^5} \tag{46}$$

After applying the condition $\lim_{r\to\infty} p(r) = p_\infty$

$$\frac{p - p_\infty}{\rho_L} = \frac{1}{r}\frac{dF}{dt} - \frac{1}{2}\frac{F^2}{r^4} \tag{47}$$

Finally, in order to determine the boundary condition of the bubble analysis, a control volume has to be placed, which will contain a section of the interface and will have an infinitely thin thickness, as seen in Figure 2.6.

The net force on this lamina in the radially outward direction per unit area is:

$$\sigma_{rr}|_{r=R} + p_B - \frac{2S}{R} \tag{48}$$

In the absence of mass transport across the interface this force is equal to zero. Thus, by combining the equations (47), (48) and by taking into account that tension is equal to $\sigma_{rr} = -p + 2\mu_L\frac{\partial u}{\partial r}$. The generalized version of Rayleigh – Plesset equation for bubble dynamics is yield.

$$\frac{p_B(t) - p_\infty(t)}{\rho_L} = R\frac{d^2R}{dt^2} + \frac{3}{2}\left(\frac{dR}{dt}\right)^2 + \frac{4\nu_L}{R}\frac{dR}{dt} + \frac{2S}{\rho_L R} \tag{49}$$

By knowing $p_\infty(t)$ and $p_B(t)$, equation (49) can be solved to find $R(t)$ at any given moment (Brennen, 1995). Also, when considering negligible conditions affecting the bubble such as surface tension and viscosity, solving equation (49) by high-order analytical approximations the result will be Young – Laplace equation (38) (Obreschkow, et al., 2012).

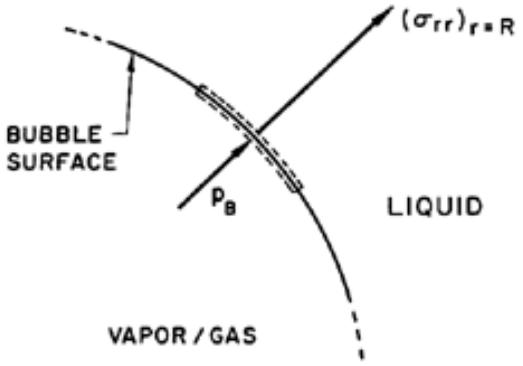

Figure 2.6 Section of the spherical bubble surface

2.6 Heat and Mass Diffusion on Cavitation

2.6.1 Thermal Effect on Nuclei

Despite the assumption of isothermal transformation and the constant temperature at vapor-liquid system, which in fact, is quite accurate, a temperature difference due to phase change. The temperature difference, is generally extremely small due to the usual large difference between gas and liquid heat capacity.

In section 2.4.2 the assumption of a fast pressure change has been made, thus the transfer of energy will not be able to occur. In this occasion, the transformation is not isothermal but adiabatic. In result the critical radius and pressure equations will change accordingly (Franc, et al., 2005).

$$\begin{cases} R_c' = R_0\left[\dfrac{3\gamma p_{g0}}{2S/R_0}\right]^{1/(3\gamma-1)} \\ p_c' = p_v - \left[1-\dfrac{1}{3\gamma}\right]\dfrac{2S}{R_c'} \end{cases} \tag{50}$$

Although, this model is not accurate enough since the vapor pressure is subjected to temperature. A better heat transfer analyses has been introduced by (Plesset, et al., 1960).

Considering a nucleus which contains non-condensable gas and undergoes a pressure drop, without a phase change phenomenon occurring, the energy balance equation of gas forms as follows:

$$\left[\frac{4}{3}\,\pi R^3\right]\rho_g C_{Vg}\Delta T = \Delta Q - p[4\pi R^2 \Delta R] \tag{51}$$

The left-hand side of equilibrium represents the internal energy of the gas and the right-hand side. Also, a thermal boundary layer develops due to temperature difference, which determines the amount of heat transferred from liquid to bubble. Thus, according to Fourier's law, the amount of heat transferred can be estimated by the following equation.

$$\Delta Q \approx \lambda_l \frac{\Delta T}{\sqrt{a_l \Delta t}} 4\pi R^2 \Delta t = \sqrt{\lambda_l \rho_l C_{pl}}\,\sqrt{\Delta t}\,4\pi R^2 \Delta T \tag{52}$$

Thus, an estimation of temperature variation can be made accordingly.

$$\begin{cases} \Delta T \approx \dfrac{\Delta T_{ad}}{1+\sqrt{\dfrac{\Delta t}{\Delta t_r}}} \\ \Delta T_{ad} = -\dfrac{3p\Delta R}{R\rho_g C_{Vg}} \\ \Delta t_r = \dfrac{\left(\rho_g C_{Vg} R\right)^2}{9\lambda_l \rho_l C_{Pl}} \end{cases} \tag{53}$$

Where, ΔT_{ad} is the temperature variation in the adiabatic case where $\Delta Q = 0$ and Δt_r is a characteristic time. The transformation can be considered as adiabatic when the internal energy variation is much larger than the exchange of heat or if the transit time is much smaller than the characteristic time. Furthemore, if the characteristic time is much larger than the transit time, according to equation (53), temperature difference is equal to zero, the transformation is considered as isothermal which means that the available time for the phenomenon of heat transfer is large enough that a thermal equilibrium can be reached (Franc, et al., 2005).

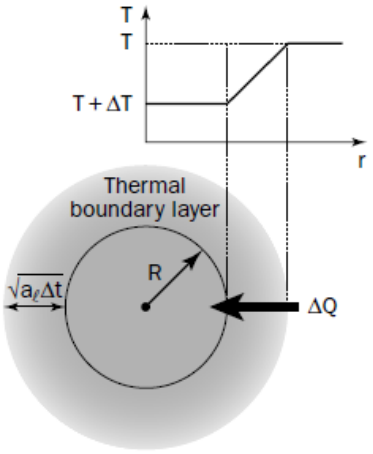

Figure 2.7 Thermal boundary layer of a nucleus

However, in some liquids that are being called thermosensitive, the temperature drop due to cavitation is not negligible. The phenomenon strongly depends upon fluids physical properties such as heat capacity, liquid to vapor ratio density heat conductivity, lantern heat of vaporization eth. (Franc, 2006).

2.6.2 Gas Diffusion

In a liquid, gas can be presented either as a form of dissolved gas or trapped in free nuclei (Brennen, 2005). Henry's law, describes the diffusion equilibrium between a liquid and the atmosphere above it

$$C_{si} = H_i(T)p_i \tag{54}$$

Where p_i is the partial pressure of a gas in the atmosphere and C_{si} the concentration of the gas, at saturation in the liquid. However, a mass flux exists if diffusion

equilibrium is not achieved. Thus, Flick's law of diffusion determines the mass flux equal to:

$$\overrightarrow{q_i} = -D_i \vec{\nabla} C_i \tag{55}$$

Therefore, by combining equations (54) and (55), the balance of mass transfer gives the classic equation of diffusion

$$\frac{\partial C_i}{\partial t} = D_i \Delta C_i \tag{56}$$

In case of a spherical nucleus in a static liquid where equilibrium (38) is satisfied, the diffusion equilibrium is given by:

$$C_s = H p_g \tag{57}$$

2.7 Cavitation Inception

In general, cavitation inception occurs when the largest critical pressure in a nucleus population is reached. According to equation set (40), this condition is referred to the nuclei with the largest radius. This threshold pressure p_s, is being called susceptibility pressure of the liquid.

In a cavitating flow, a non-dimensional parameter called cavitation number can be used as a scaling parameter at a given point r. This parameter is defined by dynamical parameters and not geometrical ones. However it cannot be determined as a scaling parameter for non-cavitating flows (Franc, et al., 2005).

$$\sigma_v = \frac{p_r - p_v(T)}{\Delta p} \tag{58}$$

Δp refers to a pressure difference that characterizes the system at a operating temperature T, thus its forms is changed according to the application.

In the case of cavitation inception, the cavitation value just before inception constitutes a threshold which is smaller than a cavitating flow, $\sigma_v > \sigma_{vi}$. This threshold depends on the usual factors considered in fluid mechanics e.g. the flow geometry, thermal parameters, turbulence level, viscosity eth.

Furthermore, at numerical modeling, cavitation number at inception is estimated by the following equation:

$$\begin{cases} \sigma_{vi} = -Cp_{min} \\ Cp = \dfrac{p_M - p_r}{\Delta p} \end{cases} \tag{59}$$

Where Cp is the pressure coefficient at a point M. When cavitation inception occurs the pressure should be equal to $p_s = p_{min}$. In that case, the condition for cavitation inception takes the following non-dimensional form:

$$\sigma_{vi} = -Cp_{min} - \Delta\sigma_s \tag{60}$$

Where $\Delta\sigma_s$ stands for the relative susceptibility underpressure:

$$\Delta\sigma_s = \frac{p_v - p_s}{\Delta p} \tag{61}$$

When the largest nuclei are destabilized and eliminated the $\Delta\sigma_s$ is increased which results in an increase at the resistance to cavitation of the liquid. In the case of increasing the pressure difference of the system, $\Delta\sigma_s$ is increased and cavitation is much more likely to occur (Franc, 2006).

2.8 Bubble Collapse

When a cavitation bubble collapses, it is consider as a macroscopic bubble with infinite radius. The procedure of bubble collapse generates noise and shock waves which are a significant subject for naval and military applications as the noise generated cannot be found at non cavitation flows, thus ships can be detected by that noise. At the same time, when a bubble, that it is attached at a surface, collapses, significant damage can be done at the surface, as force applied compared to the application area is of high magnitude.

2.8.1 Speed of collapse

As discussed in chapter 2.4.3, a nucleus has the potential to expand to a cavitation bubble. This bubble has a radius magnitude of 100 times its original (nucleus) size. At that point when a critical value of radius is reached (this is the largest possible radius for a spherical cavitation bubble), the collapse procedure will initiate (Brennen, 1995). From that moment, the time it needs for the bubble to collapse is being called the Rayleigh time and denoted with the Greek letter τ.

$$\tau = \sqrt{\frac{3}{2}\frac{\rho}{p_\infty - p_v}} \int_R^{R_0} \left[\frac{R_0^3}{R_3} - 1\right]^{-\frac{1}{2}} dR \tag{62}$$

In general, a bubble of 1 cm radius exposed to 1 bar pressure will collapse under 1 ms (Franc, et al., 2005). Considering that $\sqrt{\frac{\pi}{6}}\frac{\Gamma(5/6)}{\Gamma(4/3)} \approx 0.915$, where Γ is the factorial gamma function $\Gamma(n) = (n-1)!$, the characteristic collapse, Rayleigh time can be formed as follows:

$$\tau \cong 0.915 R_0 \sqrt{\frac{\rho}{p_\infty - p_v}} \tag{63}$$

By ignoring the effects of viscosity, non-condensable gas and surface tension, a model capable of describing the global feature of the first bubble collapse for an inviscid fluid can be made.

The Rayleigh - Plesset equation (49), can be also written:

$$\rho\left[R\ddot{R}+\frac{3}{2}\dot{R}^2\right]=p_v-p_\infty(t)+p_{g0}\left(\frac{R_0}{R}\right)^{3\gamma}-\frac{2S}{R}-4\mu\frac{\dot{R}}{R} \tag{64}$$

Also by knowing that

$$R\ddot{R}+\frac{3}{2}\dot{R}^2=\frac{1}{2\dot{R}R^2}\frac{d}{dt}\left[\dot{R}^2R^3\right] \tag{65}$$

the Rayleigh - Plesset equation will give:

$$\rho R^2R^3=-\frac{\dot{2}}{3}(p_\infty-p_v)(R^3-R_0^3) \tag{66}$$

As the fraction $t/\tau\to 1$, the radius tend to 0 and the radial inwards motion accelerates without limit (Franc, et al., 2005). Thus, by solving equation (66) in respect to the rate of radius' change, the calculation of the radius at any given moment during collapse is possible.

$$\frac{dR}{dt}=-\sqrt{\frac{2}{3}\frac{p_\infty-p_v}{\rho}\left[\frac{R_0^3}{R^3}-1\right]} \tag{67}$$

The relation between $R(t)$ and $\dot{R}(t)$can be seen in Figure 2.8. Although, the mean collapse velocity is R_0/τ (Franc, et al., 2005), the speed of the interface tends to infinity as the end of collapse approaches. Also, the interface velocity forms as follows for $R\to 0$.

$$|\dot{R}|\cong\sqrt{\frac{2}{3}\frac{p_\infty-p_v}{\rho}}\left[\frac{R_0}{R}\right]^{3/2}\cong 0.747\frac{R_0}{\tau}\left[\frac{R_0}{R}\right]^{3/2} \tag{68}$$

Plus, at the end of collapse, the radius evolves according to the law:

$$\frac{R}{R_0}\cong 1.87\left[\frac{\tau-t}{\tau}\right]^{2/5} \tag{69}$$

At this point, an estimation about the velocity of the collapse can be made. For $R/R_0=1/20$, the velocity of the collapse is $\dot{R}\approx 720\,m/s$ (Franc, et al., 2005). These values are of the order of half of the speed of sound in water. Thus, liquid

compressibility has to be taken into account as $t \to \tau$. Also, if surface tension is taken into account, the collapse should be slightly accelerated.

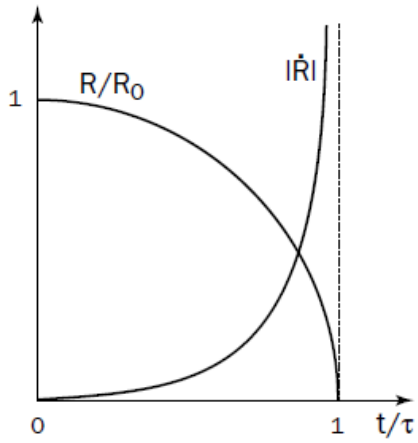

Figure 2.8 Evolution of $R(t)$ and $\dot{R}(t)$ during bubble collapse

2.8.2 Pressure Field

The pressure field of the collapsed bubble can be calculated by equation (47).

$$\Pi(r,t) = \frac{p(r,t) - p_\infty}{p_\infty - p_v} = \frac{R}{3r}\left[\frac{R_0^3}{R^3} - 4\right] - \frac{R^4}{3r^4}\left[\frac{R_0^3}{R^3} - 1\right] \tag{70}$$

A maximum non-dimensional pressure is being observed as soon as $R < 0.63R_0$ is fulfilled.

$$\begin{cases} \Pi_{max} = \dfrac{\left[\dfrac{R_0^3}{4R^3} - 1\right]^{4/3}}{\left[\dfrac{R_0^3}{R^3} - 1\right]^{1/3}} \\ \dfrac{r_{max}}{R} = \left[\dfrac{3R_0^3}{R_0^3 - 4R^3} - 1\right]^{1/3} \end{cases} \tag{71}$$

Also, when the ratio $R/R_0 \to 0$ an approximation of equation (71) can be made.

$$\begin{cases} \Pi_{max} = 0.157\left[\dfrac{R_0}{R}\right]^3 \\ \dfrac{r_{max}}{R} = 1.59 \end{cases} \tag{72}$$

In conclusion, pressure field equations can help us understand the magnitude of the phenomenon of bubble collapse. For example, for $R/R_0 = 1/20$ and $p_\infty - p_v = 1$ bar, $p_{max} = 1260$ bars, which is, indeed, a very high pressure and is located close to the bubble interface. Due to the violence of the bubble collapse phenomenon, the conservation of the liquid volume tends to concentrate liquid motion to a smaller

and smaller region, as the phenomenon evolves. Also it can be noted that the pressure inside the bubble is constant and does not offer any resistance to the liquid motion(Franc, et al., 2005).

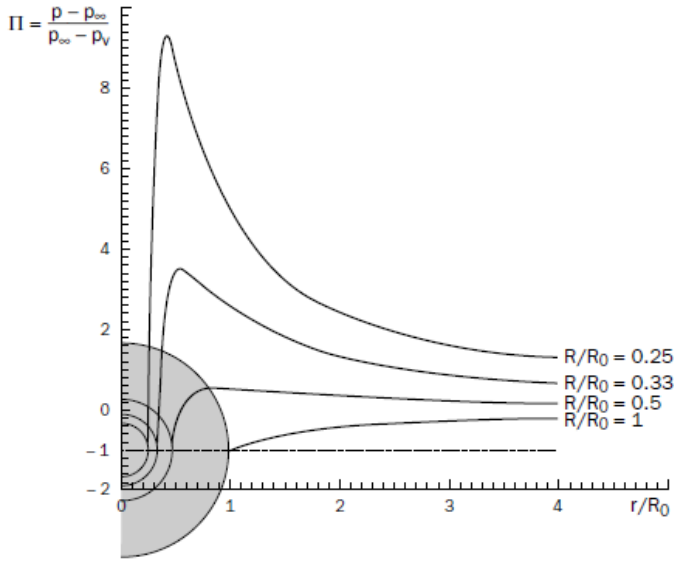

Figure 2.9 Pressure field during bubble collapse

2.8.3 Shape Distortion near a Surface

When a bubble is subjected to large values of interface acceleration at the end of the collapse, non-spherical perturbations are acting on it. Especially, when the surroundings of the bubble is asymmetrical e.g. a wall, as a result of different pressure applied at the interface, a high speed micro-jet is being created directed toward the surface. Another case of asymmetry is the neighboring bubbles in a cavitation cloud (Brennen, 1995).

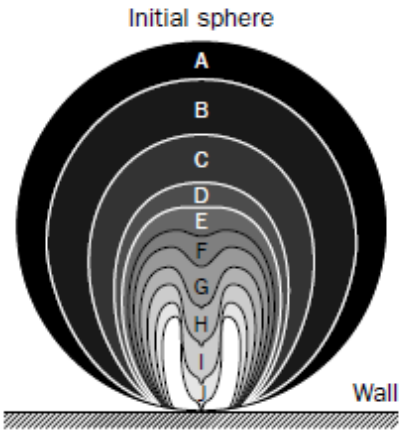

Shape	Time	Velocity (m/s)
A	0.63	7.7
B	0.885	19
C	0.986	42
D	1.013	65
E	1.033	100
F	1.048	125
G	1.066	129
H	1.082	129
I	1.098	128
J	1.119	128

Figure 2.10 Shape of a collapsing bubble near a wall and numerical results according to Plesset and Chapman (1971)

According to Blake's analytical approach, a model can be made for an evolving bubble at a non-symmetric flow field. However, it is not possible to apply the

momentum theorem directly to the fluid and body system, due to the non uniform convergence of integrals relative to the fluid momentum (Franc, et al., 2005).

The total liquid momentum in a control volume as seen in Figure 2.11 is:

$$\vec{M} = \iiint_D \rho\, \vec{V}\, dv = \iiint_D \rho \vec{\nabla}\varphi\, dv = \iint_{S+S_0+S_1} \rho\varphi \overrightarrow{v_e}\, dS \tag{73}$$

Where φ is the velocity potential and $\overrightarrow{v_e}$ the outwards unit vector, normal to the surface.

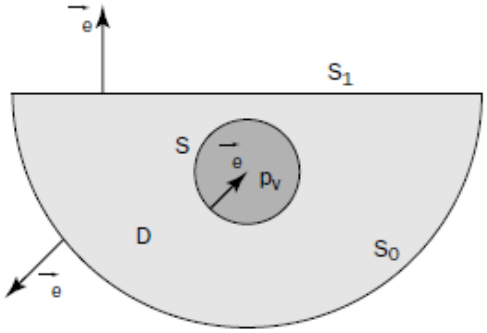

Figure 2.11 Control Volume for Blake's analytical approach

According to the integral form of the momentum equation $d\vec{M}/dt = \vec{F}$, the forces resulting from the pressure on the three boundaries can be calculated by:

$$\vec{F} = -\iint_{S+S_0+S_1} p\overrightarrow{v_e}\, dS \tag{74}$$

With reference to equation (73), a momentum attached only at the bubble, referred as bubble momentum can be calculated by:

$$\begin{cases} \overrightarrow{M_s} = \iint_S \rho\varphi \overrightarrow{v_e}\, dS \\ \\ \dfrac{d\overrightarrow{M_s}}{dt} = \overrightarrow{F_p} \end{cases} \tag{75}$$

Finally, the $\overrightarrow{F_p}$ which is the force due to the presence of the boundary S_1, which changes the bubble momentum $\overrightarrow{M_S}$ is given by (Franc, et al., 2005):

$$\overrightarrow{F_p} = \rho \iint_{S_1} \left[\varphi \frac{\partial \vec{\nabla}\varphi}{\partial v} - \frac{V^2}{2}\overrightarrow{v_e}\right] dS = \rho \iint_{S_1} \left[\frac{V^2}{2}\overrightarrow{v_e} - \frac{\partial \vec{\nabla}\varphi}{\partial v}\right] dS \tag{76}$$

In the case of a solid wall, the flow is axisymmetric and the force $\overrightarrow{F_p}$ has only an axial component. Thus $u_x = 0$ and the velocity potential is given by:

$$\varphi = \frac{q(t)}{4\pi}\{[(x+h)^2 + r^2]^{-1/2} + [(x-h)^2 + r^2]^{-1/2}\} \tag{77}$$

Where, $q(t)$ is the source intensity and h the distance of bubble center to the wall. Thus, the bubbles momentum and forces due to the nearby boundary can be found by:

$$\begin{cases} F_{px} = \dfrac{\rho q^2(t)}{4\pi} \displaystyle\int_0^{\infty} \frac{r^3}{(h^2 + r^2)^3}\, dr = \frac{\rho q^2(t)}{16\pi h^2} \\ \\ M_{Sx} = \displaystyle\int_0^t F_{px}\, dt = \frac{\rho}{16\pi h^2} \int_0^t q^2(t)\, dt \end{cases} \tag{78}$$

2.8.4 Cavitation Damage

Due to micro jets and shock waves generated when a cavitation bubble or a cavitation cloud collapses near a surface, the nearby material is damaged heavily. As the load is repetitive, it leads to the formation and propagation of cracks and in general weakens the material causing fatigue wear.

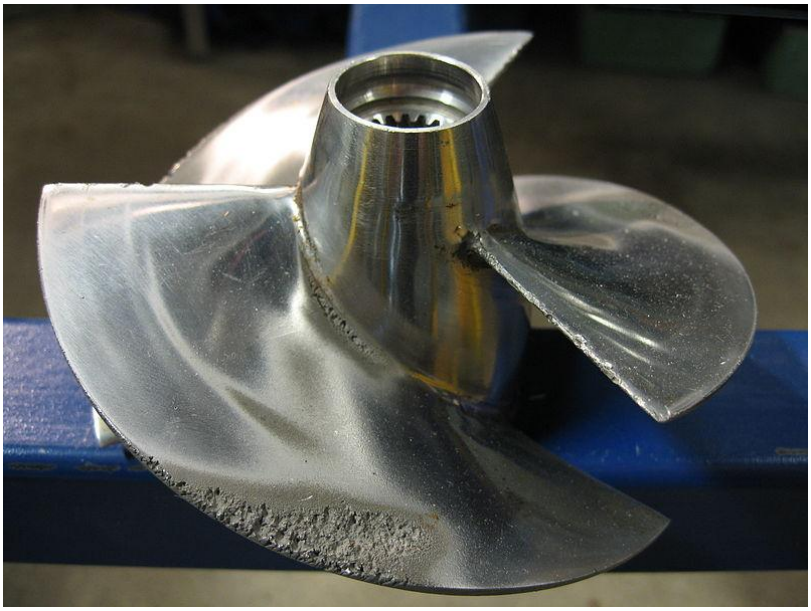

Figure 2.12 Surface fatigue as a result of cavitation damage on a propeller

3 Computational Fluid Dynamics

3.1 Introduction

Computational Fluid Dynamics or, as commonly know, CFD is a branch in fluid mechanics that involves numerical analysis of a system by using algorithms based on mathematical equations (Henk, et al., 1995). This analysis is entirely computer based and can offer numerical solutions at various and complex problems such as fluid flows combined with heat transfer phenomena and chemical reactions taking place into the system. CFD problem solving usually requires high amount of computational power as the calculations are very complex and demanding.

Computational Fluid Dynamics have a very large field of application as it can solve problems that are not possible to be solved accurately by other methods of analysis. It is being used into manufacturing since it can help improve cost efficiency and effectiveness of the product. Some examples that CFD is commonly used is to determine aerodynamics of vehicles, improving performance on heat exchange systems, internal and external combustion engines.

CFD solving procedure has three main stages: (i) the pre-processor stage, (ii) the solver stage and (iii) the post processor stage. In each stage many procedures are taking place, where major aspects of the final results are being determined.

First type of CFD was applied by Lewis Fry Richardson at 1922, who made calculations resembling modern CFD in the sense of discretization. Richardson's work applied much later at 1940 using ENIAC. Beginning at 1957 at Los Alamos National Lab, Francis H. Harlow, a CFD pioneer, led a group of scientists to model the first fluid flow by using three dimensional analyses. This group developed many numerical methods by the time being. Later on many more methods and models introduced by many scientists. Today, multi-order codes are being used in commercial software that can solve problems providing high accuracy with reasonable source consumption.

3.2 Conservation Equations

In chapter 1.2, the basic equations governing the fluid dynamics field have been introduced. In summary, seven different equations are needed in order to complete the system of equations as the main variables are: pressure, velocity at x, y and z axis, temperature, density and enthalpy.

Mass	$\frac{\partial \rho}{\partial t} + \nabla \cdot (\rho \mathbf{u})$
z - momentum	$\frac{\partial (\rho u)}{\partial t} + \nabla \cdot (\rho u \mathbf{u}) = -\frac{\partial p}{\partial x} + \nabla \cdot (\mu \nabla u) + \mathrm{S_{Mx}}$
y - momentum	$\frac{\partial (\rho v)}{\partial t} + \nabla \cdot (\rho v \mathbf{u}) = -\frac{\partial p}{\partial x} + \nabla \cdot (\mu \nabla v) + \mathrm{S_{Mx}}$
z - momentum	$\frac{\partial (\rho w)}{\partial t} + \nabla \cdot (\rho w \mathbf{u}) = -\frac{\partial p}{\partial x} + \nabla \cdot (\mu \nabla w) + \mathrm{S_{Mx}}$
Internal energy	$\frac{\partial (\rho i)}{\partial t} + \nabla \cdot (\rho i \mathbf{u}) = -p\, \nabla \cdot \boldsymbol{u} + \nabla \cdot (k \nabla T) + \Phi + S_i$
State equation	$p = p(\rho, T)$
State equation	$i = i(\rho, T)$

Table 3.1 Summary of equations in conservation form

Acknowledging those equations, general transport equation can be formed:

$$\frac{\partial (\rho \phi)}{\partial t} + \nabla \cdot (\rho \phi \boldsymbol{u}) = \nabla \cdot (\Gamma \nabla \phi) + S_\phi \tag{79}$$

This equation can simply explained in words

Rate of increase of ϕ of fluid element	$+$	Net rate of flow of ϕ out of fluid element (convection)	$=$	Rate of increase of ϕ due to diffusion	$+$	Rate of increase of ϕ due to source

Also, by using the Gauss' divergence theorem (14) the integral form of general conservation equation can be formed, which is the actual equation that CFD programs use to calculate the flow pattern and associated scalar fields (Bakker, 2006).

$$\frac{\partial}{\partial t}\left(\int_{CV} \rho \phi \, dV \right) + \int_A \boldsymbol{n} \cdot (\rho \phi \boldsymbol{u}) \, dA = \int_A \boldsymbol{n} \cdot (\nabla \cdot \phi) \Gamma \, dA + \int_{CV} S_\phi \, dV \tag{80}$$

3.3 Finite Volume Solvers

3.3.1 Finite Difference Method (FDM)

Finite difference method has a similar approach as the concept of finite differences methods approximated by Taylor's theorem at calculus. FDM is the first solver technique that has been used and is the oldest one. Generally it is a technique easy to implement but it is restricted to simple grids and does not conserves mass, momentum and energy on coarse grids (Bakker, 2006).

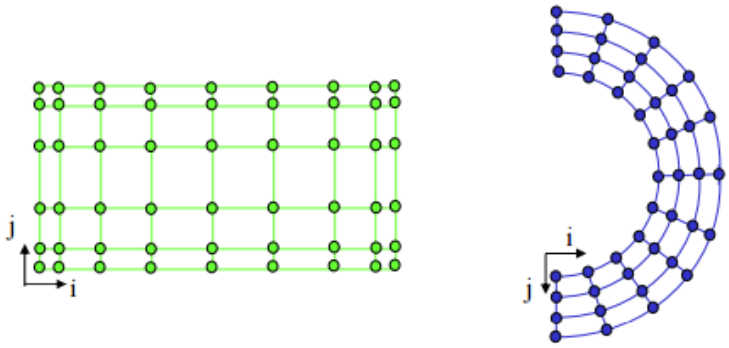

Figure 3.1 Finite difference grid example

Assuming a 2D grid element of length Δx and width Δy, a target variable $u(x, y)$ is depended on variables of square domain $0 \leq x, y \leq 1$. Also, parameters x and y can be expressed as percentage of the domain size target variable can be expressed as $u(i\ \Delta x, j\ \Delta y)$. Thus, the initial values of the target variable $u(x_0, y_0)$ can be referred as $u_{i,j}$ (Tanehill, et al., 1997).

$$u_{i+1,j} = u(x_0 + \Delta x,\ y_0) \qquad u_{i-1,j} = u(x_0 - \Delta x,\ y_0)$$

$$u_{i+1,j} = u(x_0,\ y_0 + \Delta y) \qquad u_{i-1,j} = u(x_0,\ y_0 - \Delta y)$$

In summary, the main idea of the finite difference method is described by:

$$\frac{\partial u}{\partial x} = \lim_{\Delta x \to 0} \frac{u(x_0 + \Delta x,\ y_0) - u(x_0,\ y_0)}{\Delta x} \tag{81}$$

Accuracy

The accuracy, or the error, is defined as the difference between the actual value of the solution and the approximation derived from the used method. At finite difference method, two types of errors are observed. The first one derives from the loss of precision due to rounding at decimal quantities and the second one due to the discretization. Most of the times, error is denoted by letter O.

By expressing equation (81), by using Taylor-series expansion for $u(x_0 + \Delta x, y_0)$ about (x_0, y_0) the "forward" difference can be formed (Tanehill, et al., 1997).

$$\frac{\partial u}{\partial x}\Big)_{x_0,\,y_0} = \frac{u(x_0+\Delta x, y_0)-u(x_0,y_0)}{\Delta x} - \frac{\partial^2 y}{\partial x^2}\Big)_0 \frac{\Delta x}{2!} - \cdots \tag{82}$$

The remaining factors of the expansion can be considered as part of the discretization error.

$$\frac{\partial u}{\partial x}\Big)_{i,j} = \frac{u_{i+1,j}-u_{i,j}}{\Delta x} - O(\Delta x) \tag{83}$$

Where $|O(\Delta x)| \leq K|\Delta x|$ for $\Delta x \to 0$ and K a constant $K \in \mathbb{N}$.

Discretization

In reality, a lot of different approaches based on finite differences method can be used. Each method can successfully support an acceptable solution subjected to computational power economy, simplicity and accuracy. Those different approaches are called stencils and they determine the way logical continuity through time between descritized points is achieved. The algorithm determining that procedure is being called stencil walking or stencil jumping and some of those algorithms tend to be more complex, by using more points in each jump to achieve better results (Tanehill, et al., 1997).

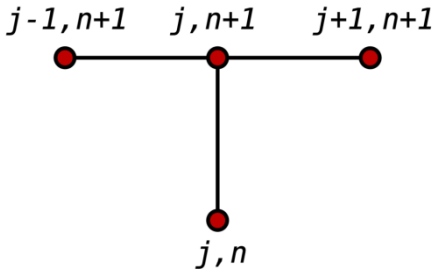

Figure 3.2 Graphic stencil example of a second order forward difference derivative

3.3.2 Finite Element Method (FEM)

Finite element method can be considered as a two dimensions technique with three dimension applications that is mostly used for structural analyses. In the mid- to late 70's it was refined for fluid analyses. It offers a better accuracy at coarse grids and is excellent for diffusion dominated and viscous free surface problems. Although, it can be slow for larger grids and it is not capable for a turbulent flow analyses (Bakker, 2006).

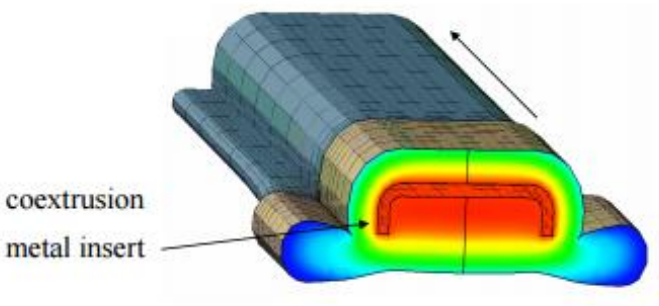

Figure 3.3 Finite element mesh example

A typical work of the finite element method is firstly the division of the whole domain into several subdomains. Each subdomain is represented by a set of equations which determines the boundaries of each element. By this method, a more accurate representation of complex domains is possible. Later, all subdomains' equations are recombined into a global system of equations by transforming local node coordinates to the global domain's nodes.

3.3.3 Finite Volume Method (FVM)

Finite volume method is the most common technique for fluid analyses. FVM base solvers have an advantage in memory use and computed power needed especially for large domains and have high accuracy for high speed and turbulent flows as well as source term dominated flows. Despite other used methods, FVM solvers don't limit the shape of the cells and can achieve mass, momentum and energy conversant even on coarse grids (Bakker, 2006).

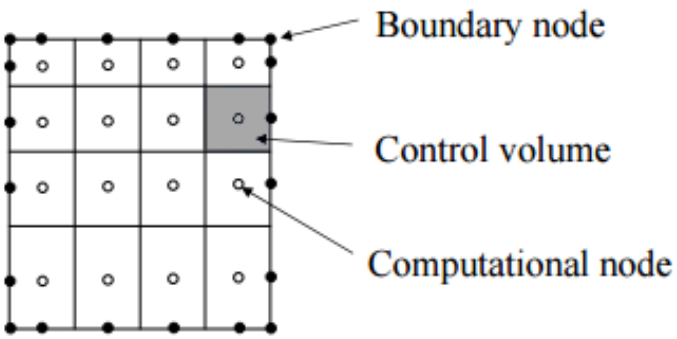

Figure 3.4 Finite volume method grid aspects

When using finite volume method, the domain is divided into a finite number of control volumes. The shells can be unstructured and have various shapes. All equations are applied at the center of the cells which is referred as the "computational node". The boundaries of each control volume are determined by the edges of each cell. However, the values at each control volume face are needed to be possible for the derivative terms to be evaluated, so several assumptions have to be made. By using that method, integral conservation is achieved over the control volume. The solver can be either simultaneous or iterative (Bakker, 2006).

Discretization

Consider a part of grid with a total of 6 cells, as seen in Figure 3.5. All equation applied at the flow, have to discretized for all conserved variables (momentum, energy, pressure etc.) as a linear equation in order to be solved iteratively for all cells in the domain. The general result of linearized equation for variable ϕ is formed as follows: discrete

$$a_P \phi_P = \sum_{nb} a_{nb} \phi_{nb} + b \tag{84}$$

Where a a coefficient describing to transition of the variable between cells and the nb denotion referring to the neighbor cells of cell P. In general, the steps that are taken in order to conclude to a discretized equation are the following:

1. Integration of the equation in each cell
2. Calculation of face values in terms of cell-centered values
3. Collection of like terms

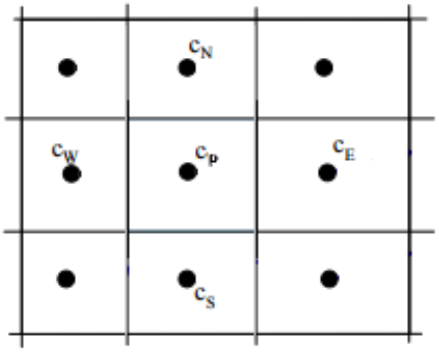

Figure 3.5 Part of grid at finite volume method

Convergence and Residuals

The so called “convergence” is achieved when the variables from a iteration to the next one, becomes small enough that the difference is subjected to errors of the computation. In result, the solution no longer changes with additional iterations and mass, momentum, energy and scalar balances are obtained (Bakker, 2006).

The error or imbalance in conservation equations is measured by residuals, where the absolute residual at point P is defined in equation (85).

$$R_P = \left| a_P \phi_P - \sum_{nb} a_{nb} \phi_{nb} - b \right| \tag{85}$$

To obtain relative error, residuals are commonly scaled relative to local valued of the variable ϕ.

$$R_{P,scalled} = \frac{|a_P\phi_P - \sum_{nb} a_{nb}\phi_{nb} - b|}{|a_P\phi_P|} \quad (86)$$

Furthermore, residuals can be normalized, by dividing them by the maximum residual that have been found at any time during the iterative process.

$$R^{\phi} = \frac{\sum_{all\ cells}|a_P\phi_P - \sum_{nb} a_{nb}\phi_{nb} - b|}{\sum_{all\ cells}|a_P\phi_P|} \quad (87)$$

In general, convergence is achieved when the scaled residuals are in order of *1E-3* to *1E-4* or less (Bakker, 2006).

Relaxation

By applying equation (84), at every iteration, at each cell, a new value of variable ϕ is calculated. In result, an error that would be introduced during the solving procedure will result to oscillations in the flow solution as the error will increase at every iteration. In order to deal with that problem, a factor has to be introduced at the equation that will suppress the unwanted oscillation. That factor is called "under relaxation" factor and is applied for almost all variables ϕ involve at the solution.

$$\phi_P^{new,used} = \phi_P^{old} + U\left(\phi_P^{new,predicted} - \phi_P^{old}\right) \quad (88)$$

In most times, factor U will be lower than the value of 1, that will result in underelaxation. However, by applying under-relaxation factors at the equation (84), the speed of convergence might be slow down. Although, factor U can be equal to 1 where there will be no relaxation, or sometimes, even higher than 1, in order to accelerate the convergence speed. At the last case the stability of the calculation will significantly decreased (Bakker, 2006).

Calculating Face Values

As mentioned in previous chapters some assumptions have to be made in order to calculate the values of ϕ at cells' faces. There some different schemes that are used for that application, while each one keeps a different balance between accuracy and speed.

Higher order schemes tend to be more accurate although, they lack stability and they increase computational time. A common practice is to use more accurate numerical approaches for the first iterations and changes the model for the rest iterations. In that way, a good combination of stability and accuracy is achieved.

First Order Upwind

First order upwind, is the simpler numerical approach. The result is pretty stable although very diffusive and gradients in the flow field tend to be smeared out (Bakker, 2006). By using that model the assumption of the value ϕ at the face being the same as the cell center upstream is made. As the simplest form it is more commonly used for initial iterations.

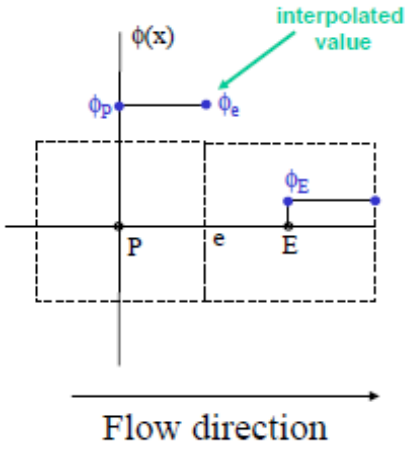

Figure 3.6 First order upwind scheme

Central Differences

At central differences scheme, the value of ϕ at the face is calculated by linear interpolation between the cell centered values. In such way, the result is more accurate than first order upwind although it can lead to oscillations or divergence if the local Peclet number is larger than 2.

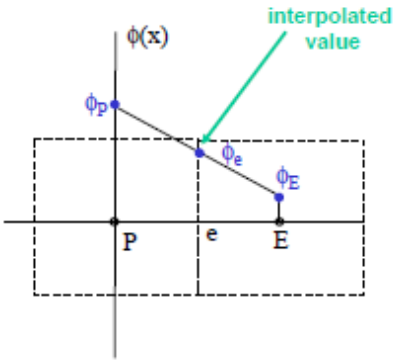

Figure 3.7 Central differences scheme

This approach should only be used for transient calculations accompanied with large eddy simulation (LES) turbulence model[7] and effectively fine mesh in order to keep Peclet number less than 1.

[7] See chapter 3.4.2

Power Law

Power law approach is based on analytical solution of the one-dimensional convection-diffusion equation. The face value is calculated by an exponential equation approximated by a power law equation as follows:

$$\phi_e = \phi_P - \frac{(1 - 0.1Pe)^5}{Pe}(\phi_E - \phi_P) \tag{89}$$

In the case of Peclet number being larger than 10, diffusion is ignored and first order upwind method is used (Bakker, 2006). Power law is better to be used in certain problems that are especially suitable for that method and should not be used as a general approach model.

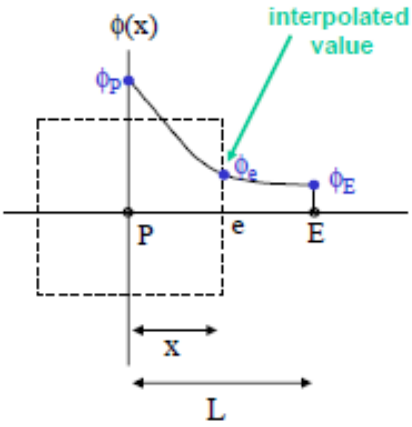

Figure 3.8 Power law scheme

Second Order Upwind

Second order upwind is the most accurate numerical approach for calculating faces' values. It uses the cell value in the two cells upstream to determine the value of ϕ at a face. This method is possible to generate values outside of the range of cell values in regions with strong gradients. In order to solve this issue a common practice is to apply value limiters to generate results within the existing ranges. This combination is the most popular numerical approach as it combines accuracy and stability (Bakker, 2006).

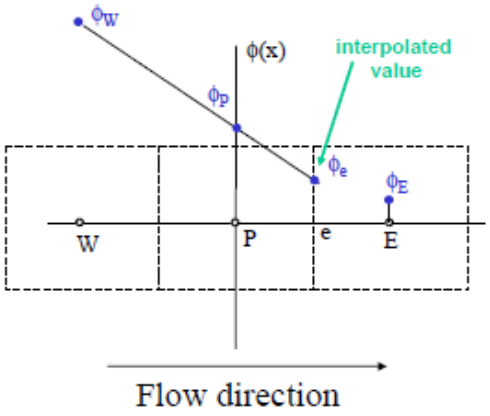

Figure 3.9 Second order upwind scheme

QUICK

QUICK is an acronym for Quadratic Upwind Interpolation for Convective Kinetics and is a very accurate approach but in regions with strong gradients, overshoot and undershoots can occur (Bakker, 2006). This car result in stability issues during the solving procedure. At QUICK a quadratic curve is fitted through two upstream nodes and one downstream node (Bakker, 2006).

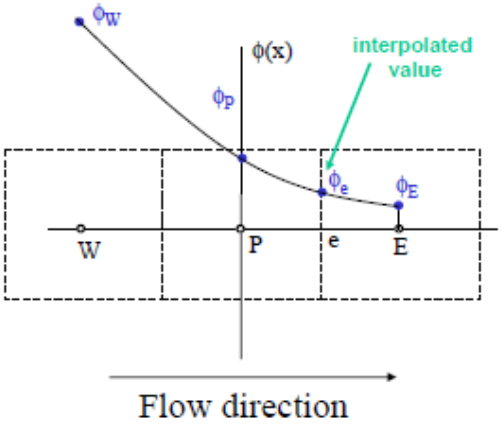

Figure 3.10 QUICK scheme

As in power law approach, QUICK method is better to be used with certain problems that are best solved with that method.

3.4 Turbulence Modeling

Turbulence modeling is the key element in computation fluid dynamics simulations. It contains various equations that can provide results for variables in order for the system of mean flow equations to be considered as closed. Through time, a lot of models have been developed, each one focusing on certain aspect of the flow in order to be more accurate for certain flows.

In turbulence modeling, turbulent fluctuations are not being solved in detail. All models allow the calculation of the mean flow, without calculating the full time-dependent flow field.

3.4.1 RANS-based Models

RANS is an acronym for Reynolds-averaged Navier-Strokes equations. Those are time-averaged equations of motion for a fluid flow. The objective of the turbulence models for the RANS equations is to decompose the Navier-Strokes equations into the mean and fluctuating components.

$$\varphi = \bar{\varphi} + \varphi' \tag{90}$$

The same procedure can be done for both scalar and vector quantities. Accordingly by using that averaging model for continuity momentum equation, the RANS equations derives:

$$\frac{\partial \rho}{\partial t} + \frac{\partial}{\partial x_i}(\rho u_i) = 0 \tag{91}$$

$$\frac{\partial}{\partial t}(\rho u_i) + \frac{\partial}{\partial x_j}(\rho u_i u_j) = -\frac{\partial p}{\partial x_i} + \frac{\partial}{\partial x_j}\left[\mu\left(\frac{\partial u_i}{\partial x_j} + \frac{\partial u_j}{\partial x_i} - \frac{2}{3}\,\delta_{ij}\frac{\partial u_l}{\partial x_l}\right)\right] + \frac{\partial}{\partial x_j}\left(-\rho\overline{u_i' u_j'}\right) \tag{92}$$

A common method to model those equations is by Boussinesq's approach. According Boussinesq's proposition (1877), the Reynolds stresses can be linked to the mean rate of deformation (Bakker, 2006). In that case, viscous stresses are given by:

$$\tau_{ij} = -\rho\overline{u_i' u_j'} = \mu_t\left(\frac{\partial U_i}{\partial x_j} + \frac{\partial U_j}{\partial x_i}\right) \tag{93}$$

Where *i, j* and *k* suffix notations for the *x, y* and *z* directions and μ_t, the turbulent viscosity which is not homogeneous and can varies through space.

Linear Eddy Viscosity Models

Linear eddy viscosity models, model RANS equations by a linear constitutive relationship with the mean flow straining field:

$$-\rho\langle u_i u_j\rangle = 2\mu_t S_{ij} - \frac{2}{3}\rho k\delta_{ij} \tag{94}$$

Where k, the mean turbulent kinetic energy

$$k = \frac{1}{2}(\langle u_1 u_1\rangle + \langle u_2 u_2\rangle + \langle u_3 u_3\rangle) \tag{95}$$

and S_{ij}, the mean strain rate

$$S_{ij} = \frac{1}{2}\left[\frac{\partial U_i}{\partial x_j} + \frac{\partial U_j}{\partial x_i}\right] - \frac{1}{3}\frac{\partial U_k}{\partial x_k}\delta_{ij} \tag{96}$$

Furthermore, the term $\frac{2}{3}\rho k\delta_{ij}$ is required by the tensorial algebra purposes when solving for turbulent models that solves a transport equation for k.

Algebraic Models

Algebraic turbulent models or zero-equation turbulence models are the simplest subcategory of RANS-based models, as they don't require the solution of any additional equation, and are calculated directly from the flow variables. Algebraic models are unable to capture convection and diffusion of turbulent energy. Those models are used for initial phases and for simpler flows and geometries (Chen, 1997).

Most known algebraic models are: Cebeci-Smith model, Balwin-Lomax model, Johnson-King model and the roughness-dependent model

One Equation Models

One equation models solve one turbulent transport equation, usually the turbulent kinetic energy. The most used one-equation model is the Spalart-Allmaras model. Other well known ones are: the original Prandtl's one-equation model, Bladwin-Barth model and Rahman-Agarwa-Siikonen model.

Spalart-Allmaras Model

Spalart-Allmaras model solves a single conservation equation for the turbulent viscosity. In general, Spalart-Allmaras model is good for attached wall-bounded flows and flows with mild separation and recirculation. Despite that, it has a narrow use due to the lack more complex models. The transport equation for $\tilde{v}$ is (Fluent Inc., 2006):

$$\frac{\partial}{\partial t}(\rho\tilde{v}) + \frac{\partial}{\partial x_i}(\rho\tilde{v}u_i) = G_v + \frac{1}{\sigma_{\tilde{v}}}\left\{\frac{\partial}{\partial x_j}\left[(\mu + \rho\tilde{v})\frac{\partial\tilde{v}}{\partial x_j}\right] + C_{b2}\rho\left(\frac{\partial\tilde{v}}{\partial x_j}\right)^2\right\} - Y_v + S_{\tilde{v}} \tag{97}$$

Where G_v is the production of turbulent viscosity and Y_v is the destruction of turbulent viscosity that occurs in the near-wall region due to wall blocking and viscous damping. $S_{\tilde{v}}$ and C_{b2} are constants. $S_{\tilde{v}}$ is a source term. Note that since the turbulence kinetic energy k is not calculated in the Spalart-Allmaras model, the last term in equation (93) is ignored when estimating the Reynolds stresses.

Two-Equation Models

Two-equation turbulence models are the most used types of turbulence models. By definition, they include two transport equations for turbulent properties of the flow. This allows a two equation model to account for convection and diffusion of turbulent energy. Most used two-equation models are analyzed bellow:

$k-\varepsilon$ *Model*

$k-\varepsilon$ model focuses on the mechanisms that affect the turbulent kinetic energy k and the dissipation rate of k, ε. It is a relative simple model and can lead to stable calculations. It is commonly use at it can provide with a reasonable prediction for many flow types. However, it is valid only for fully turbulent flows and is not recommended for swirling and rotating flows as well as flows with strong separation(Bakker, 2006).

The instantaneous kinetic energy $k(t)$ of a turbulent flow is the sum of mean kinetic energy K and the turbulent kinetic energy k:

$$K = \frac{1}{2}(U^2 + V^2 + W^2)$$

$$k = \frac{1}{2}\left(\overline{u'^2} + \overline{v'^2} + \overline{w'^2}\right)$$

$$k(t) = K + k$$

Standard $k-\varepsilon$ Model

The transport equations for k and ε are formed by the following equations respectable (Fluent Inc., 2006):

$$\frac{\partial}{\partial t}(\rho k) + \frac{\partial}{\partial x_i}(\rho k u_i) = \frac{\partial}{\partial x_j}\left[\left(\mu + \frac{\mu_t}{\sigma_k}\right)\frac{\partial k}{\partial x_j}\right] + G_k + G_b - \rho\varepsilon - Y_M + S_k \quad (98)$$

$$\frac{\partial}{\partial t}(\rho\varepsilon) + \frac{\partial}{\partial x_i}(\rho\varepsilon u_i) = \frac{\partial}{\partial x_j}\left[\left(\mu + \frac{\mu_t}{\sigma_\varepsilon}\right)\frac{\partial \varepsilon}{\partial x_j}\right] + C_{1\varepsilon}\frac{e}{k}(G_k + G_{3e}G_b) - C_{2e}\rho\frac{\varepsilon^2}{k} + S_e \quad (99)$$

The term G_k, representing the production of turbulence kinetic energy due to the mean velocity gradients. In a manner of consistent with Boussinesq hypothesis it forms as:

$$G_k = \mu_t S^2 \quad (100)$$

where S is the modulus of the mean rate-of-strain tensor defined by:

$$S \equiv \sqrt{2S_{ij}S_{ij}} \quad (101)$$

The term G_b, is the generation of turbulence kinetic energy due to buoyancy:

$$G_b = \beta g_i \frac{\mu_t}{\mathrm{Pr}_t} \frac{\partial \rho}{\partial x_i} \tag{102}$$

where Pr_t is the turbulent Prandtl number for energy. The default value is 0.85. β, the coefficient of thermal expansion is defined by:

$$\beta = \frac{1}{\rho}\left(\frac{\partial p}{\partial T}\right)_p \tag{103}$$

The term Y_M represents the contribution of the fluctuating dilatation in compressible turbulence to the overall dissipation:

$$Y_M = 2\rho\varepsilon M_t^2 \tag{104}$$

Where M_t the turbulent Mach number defined by $M_t = \sqrt{k/a^2}$ and a the speed of sound $a \equiv \sqrt{\gamma RT}$. Furthermore, the turbulent viscosity μ_t is defined by:

$$\mu_t = \rho C_\mu \frac{k^2}{\varepsilon} \tag{105}$$

The degree to which ε is affected by the buoyancy is determined by the constant C_{3e}:

$$C_{3e} = tanh\left|\frac{v}{u}\right| \tag{106}$$

where v is the component of the flow velocity parallel to the gravitational vector and u the component of the flow velocity perpendicular to the gravitational vector. C_{3e} will become equal to 1 for buoyant shear layers for which the main flow direction is aligned with the direction of the gravity. Instead, C_{3e} will become 0 for buoyant shear layers that are perpendicular to gravitational vector.

Finally, $\sigma_k = 1$ and $\sigma_\varepsilon = 1.3$ are the turbulent Prandtl numbers for k and ε, $C_{1\varepsilon} = 1.44$, $C_{2\varepsilon} = 1.9$, and $C_\mu = 0.09$ are constants and S_k and S_e are source terms.

RNG $k-\varepsilon$ Model

RNG $k-\varepsilon$ model is an improvement from the standard model. It derives from the application of the renormalization group method, a rigorous statistical technique applied to the instantaneous Navier-Stokes equations. It offers better predictions for high streamline curvature and strain rate, improve results for transitional flows and wall heat and mass transfer (Bakker, 2006).

The transport equations for RNG $k-\varepsilon$ model are the following:

$$\frac{\partial}{\partial t}(\rho k) + \frac{\partial}{\partial x_i}(\rho k u_i) = \frac{\partial}{\partial x_j}\left[a_k \mu_{eff} \frac{\partial k}{\partial x_j}\right] + G_k + G_b - \rho\varepsilon - Y_M + S_k \quad (107)$$

$$\frac{\partial}{\partial t}(\rho \varepsilon) + \frac{\partial}{\partial x_i}(\rho \varepsilon u_i) = \frac{\partial}{\partial x_j}\left[a_k \mu_{eff} \frac{\partial \varepsilon}{\partial x_j}\right] + C_{1e}\frac{e}{k}(G_k + G_{3e}G_b) - C_{2\varepsilon}\rho\frac{\varepsilon^2}{k} - R_e + S_e \quad (108)$$

Some of the variables are the same as standard $k-\varepsilon$ model. Although, the term G_b is changing as its term Pr_t is now calculated by the equation $\mathrm{Pr}_t = 1/a$. Furthermore, the effective viscosity is calculated by the result of RNG theory which is a differential equation:

$$d\left(\frac{\rho^2 k}{\sqrt{\varepsilon\mu}}\right) = 1.72\frac{\hat{v}}{\sqrt{\hat{v^3} - 1 + C_v}}d\hat{v} \quad (109)$$

where $\hat{v} = \mu_{eff}/\mu$ and $C_v \approx 100$. Term C_μ reforms to $C_\mu = 0.0845$ following RNG theory. The inverse effective Prandtl numbers, a_k and a_ε, are computed using the following formula derived analytically by the RNG theory:

$$\left|\frac{a - 1.3929}{a_0 - 1.3929}\right|^{0.6321}\left|\frac{a - 2.3929}{a_0 - 2.3929}\right|^{0.3679} = \frac{\mu_{mol}}{\mu_{eff}} \quad (110)$$

Where $a_0 = 1$ and when $\mu_{mol}/\mu_{eff} \ll 1$ (in high-Reynolds-number limit), $a_k = a_e \approx 1.393$. The main difference between the RNG and standard $k-\varepsilon$ models lies in the additional term in the ε equation. The term R_e, can be calculated by the following equation:

$$R_e = \frac{C_\mu \rho \eta^3 \left(1 - \frac{\eta}{\eta_0}\right)}{1 + \beta\eta^3}\frac{\varepsilon^2}{k} \quad (111)$$

Where $\eta \equiv Sk/\varepsilon$, $\eta_0 = 4.38$ and $\beta = 0.012$. Finally, there is an additional modification named RNG swirl modification. This modification provides an option to account for the effects of swirl or radiation by modifying the turbulent viscosity term:

$$\mu_t = \mu_{t0}\, f\left(a_s, \Omega, \frac{k}{\varepsilon}\right) \quad (112)$$

where μ_{t0} is the value of turbulent viscosity calculated witouth the swirl modification like equation (105). Ω is a characteristic swirl number and a_s is a swirl constant that assumes different values depending on whether the flow is swirl-dominated or only mildly swirling.

Realizable $k-\varepsilon$ model

Realizable k$-\varepsilon$ model replaces constants at ε equation with a variable. By doing this, it achieves a better performance for rotation and recirculation flows along with stron streamline curvature. Also, it is able to predict planar and round jets in contrast with previous $k-\varepsilon$ models (Bakker, 2006).

By the term "realizable", it is meant that certain mathematical constrains on the Reynolds stresses are satisfied. The transport equations for realizable $k-\varepsilon$ model forms as follows (Fluent Inc., 2006):

$$\frac{\partial}{\partial t}(\rho k)+\frac{\partial}{\partial x_j}(\rho k u_j)=\frac{\partial}{\partial x_j}\left[\left(\mu+\frac{\mu_t}{\sigma_k}\right)\frac{\partial k}{\partial x_j}\right]+G_k+G_b-\rho\varepsilon-Y_M+S_k \quad (113)$$

$$\frac{\partial}{\partial t}(\rho\varepsilon)+\frac{\partial}{\partial x_j}(\rho\varepsilon u_j)=\frac{\partial}{\partial x_j}\left[\left(\mu+\frac{\mu_t}{\sigma_\varepsilon}\right)\frac{\partial \varepsilon}{\partial x_j}\right]+\rho C_1-\rho C_2\frac{\varepsilon^2}{k+\sqrt{v\varepsilon}}+C_{1e}\frac{\varepsilon}{k}C_{3e}G_b+S_e \quad (114)$$

where $C_1=\max\left[0.43,\frac{\eta}{\eta+5}\right]$ and $\eta=S\frac{k}{\varepsilon}$. The turbulent viscosity model is changed too as the term C_μ forms:

$$C_\mu=\frac{1}{A_0+A_s\frac{kU^*}{e}} \quad (115)$$

where $U^*\equiv\sqrt{S_{ij}S_{ij}+\tilde{\Omega}_{ij}\tilde{\Omega}_{ij}}$, $\tilde{\Omega}_{ij}=\Omega_{ij}-2\varepsilon_{ijk}\omega_k$ and $\Omega_{ij}=\overline{\Omega_{ij}}-\varepsilon_{ijk}\omega_k$. The term $\overline{\Omega_{ij}}$ represents the mean rate-of-rotation tensor viewed in a rotating reference frame with the angular velocity ω_k. Also, $A_0=4.04$, $A_s=\sqrt{6}cos\varphi$ $\varphi=\frac{1}{3}\cos^{-1}(\sqrt{6}W)$, $W=\frac{S_{ij}S_{jk}S_{ki}}{\tilde{S}^3}$, $\tilde{S}=\sqrt{S_{ij}S_{ij}}$ and $S_{ij}=\frac{1}{2}\left(\frac{\partial u_j}{\partial x_i}+\frac{\partial u_i}{\partial x_j}\right)$. The rest variables are the same as standard $k-\varepsilon$ model.

$k-\omega$ Model

$k-\omega$ is another well known two equation model. It is applicable to wall-bounded and free shear flows as it can predict free shear flow spreading rates that are in close agreement with measurements for far wakes, mixing layers, and plane, round and radial jets. Like $k-\varepsilon$ model it uses kinetic energy as one of its PDEs, and ω term which is an inverse time scale that is associated with the turbulence (Fluent Inc., 2006).

Standard $k-\omega$ model

The standard $k-\omega$ model is an empirical model based on $k-\varepsilon$. Its transport equations are:

$$\frac{\partial}{\partial t}(\rho k) + \frac{\partial}{x_i}(\rho k u_i) = \frac{\partial}{x_j}\left(\Gamma_k \frac{\partial k}{\partial x_j}\right) + G_k - Y_k + S_k \tag{116}$$

$$\frac{\partial}{\partial t}(\rho \omega) + \frac{\partial}{x_i}(\rho \omega u_i) = \frac{\partial}{x_j}\left(\Gamma_\omega \frac{\partial \omega}{\partial x_j}\right) + G_\omega - Y_\omega + S_\omega \tag{117}$$

Both Γ_k and Γ_ω represent the effective diffusivity of k and ω respectively:

$$\Gamma_k = \mu + \frac{\mu_t}{\sigma_k} \tag{118}$$

$$\Gamma_\omega = \mu + \frac{\mu_t}{\sigma_\omega} \tag{119}$$

Where σ_k and σ_ω are the turbulent Pradtl numbers for k and ω respectively, where $\sigma_k = \sigma_\omega = 2$. The turbulent viscosity μ_t is computed by combining k and ω as follows:

$$\mu_t = a^* \frac{\rho k}{\omega} \tag{120}$$

The coefficient α^* damps the turbulent viscosity causing a low-Reynolds-number correction. The term G_k, represents the production of turbulence kinetic energy.

$$G_k = -\rho \overline{u_i' u_j'} \frac{\partial u_j}{\partial x_i} = \mu_t S^2 \tag{121}$$

Where S is the modulus of the mean rate-of-strain tensor defined by equation (101). Also, the production of ω is given by:

$$G_\omega = \alpha \frac{\omega}{k} G_k \tag{122}$$

The coefficient a is given by:

$$a = \frac{a_\infty}{a^*}\left(\frac{a_0 + Re_t/R_\omega}{1 + Re_t/R_\omega}\right) \tag{123}$$

where $R_\omega = 2.95$ and $Re_t = \frac{\rho \kappa}{\mu \omega}$. Also, the coefficient a^* is given by:

$$a^* = a_\infty^*\left(\frac{a_0^* + Re_t/R_k}{1 + Re_t/R_k}\right) \tag{124}$$

where $a_0^* = \frac{\beta_i}{3}$, $\beta_i = 0.072$ and $R_k = 6$. The dissipation of k is given by:

$$Y_k = \rho \beta^* f_{\beta^*} k \omega \tag{125}$$

where

$$f_{\beta^*} = \begin{cases} 1 & , \quad x_k \leq 0 \\ \dfrac{1+680x_k^2}{1+400x_k^2}, & x_k > 0 \end{cases} \tag{126}$$

where

$$x_k \equiv \frac{1}{\omega^3}\frac{\partial k}{\partial x_j}\frac{\partial \omega}{\partial x_j} \tag{127}$$

and $\beta^* = \beta_i^*[1+\zeta^* F(M_t)]$, $\beta_i^* = \beta_\infty^* \frac{4/15+(Re_t/R_\beta)^4}{1+(Re_t/R_\beta)^4}$, $\zeta^* = 1.5$, $R_\beta = 8$ and $\beta_\infty^* = 0.09$. The dissipation of ω is given by:

$$Y_\omega = \rho\beta f_\beta \omega^2 \tag{128}$$

where,

$$f_\beta = \frac{1+70\chi_\omega}{1+80\chi_\omega} \tag{129}$$

$$\chi_\omega = \left|\frac{\Omega_{ij}\Omega_{jk}S_{ki}}{(\beta_\infty^*\omega)^3}\right| \tag{130}$$

$$\Omega_{ij} = \frac{1}{2}\left(\frac{\partial u_i}{\partial x_i} - \frac{\partial u_j}{\partial x_i}\right) \tag{131}$$

$$\beta = \beta_i\left[1 - \frac{\beta_i^*}{\beta_i}\zeta^* F(M_t)\right] \tag{132}$$

Finally, the compressibility function, $F(M_t)$, is given by

$$F(M_t) = \begin{cases} 0 & , \quad M_t \leq M_{t0} \\ M^2 - M_{t0}^2, & M_t > M_{t0} \end{cases} \tag{133}$$

And $M_t^2 = 2k/a^2$ and $M_{t0} = 0.25$.

Nonlinear Eddy Viscosity Models

Nonlinear eddy viscosity models use an eddy viscosity coefficient to relate the mean turbulent filed to the mean velocity field in a nonlinear relationship (Chen, 1997).

$$-\rho\langle u_i u_j\rangle = 2\mu_t F_{nl}\left(S_{ij}, \Omega_{ij}, \ldots\right) \tag{134}$$

where F_{nl}, an nonlinear function possible dependent on the mean strain and vorticity fields or even other turbulent variables.

Reynolds Stress Transport Models

Reynolds stress transport models (RST), are higher level models that elaborate turbulence models. At those models, the RANS equations are calculated by solving additional transport equations for the six independent Reynolds stresses. The transport equations derived by Reynolds averaging the product of momentum equations with a fluctuating property while closure requires one equation for turbulent dissipation. However the assumption of isotropic eddy viscosity is avoided. This approach is called "second order closure" and accounts for the directional effects of the Reynolds stress fields (Bakker, 2006). RSM approach is good for accurately prediction of more complex flows as it accounts for streamline curvature, swirls, rotation and high strain rates.

3.4.2 Large Eddy Simulations

Large eddy simulations (LES), are using a different approach compared to RANS-based models, and consider the dependency of flow's large eddies to the geometry of problem. This approach allows an explicitly solution for the large eddies and an implicitly account for the small eddies by using subgrid-scale model (SGS) (Chen, 1997). In general, LES approach can provide with a very accurate solution but is high demanded in terms of computer power.

3.5 Multiphase Modeling

A multiphase flow, is a simultaneous flow of a material with different phases e.g. gas and liquid phase like cavitation or materials with different chemical properties but in the same state e.g. oil droplets in water. In all cases there is a primary and secondary phase where the primary is continuous while the other one is dispersed within the continuous phase (Bakker, 2006).

Inside a two-phase flow, each phase can be laminar or turbulent although the main fluid flow can be turbulent with respect to secondary phase but laminar with respect to vessel. The most common measurement of a two-phase flow is the volume fraction (VOF) which refers to the volume fraction of the secondary phase compared to the primary through space and time.

$$VOF = \frac{Volume\ of\ the\ phase\ in\ a\ cell}{Volume\ of\ the\ cell} \tag{135}$$

3.5.1 Mixture Model

The mixture model is a simplified multiphase model that can be used for multiphase flows that the two phases can move with different velocities, but assume local

equilibrium over short spatial length scales (Fluent Inc., 2006). It can also be used to calculate non-Newtonian viscosity.

The mixture model can model each phase by solving the momentum, continuity, and energy equations for the mixture, the volume fraction equations for the secondary phases, and algebraic expressions for the relative velocities. Typical applications include sedimentation, cyclone separators, particle-laden flows with low loading, and bubbly flows where the gas volume fraction remains low (Fluent Inc., 2006).

The mixture model can only be used with a pressure-based solver and cannot combine cavitation model with LES turbulence modeling. Also, the mixture model cannot provide a solution for inviscid flows and cannot predict solidification or melting (Bakker, 2006).

3.5.2 Eulerian Model

Eulerian model is suitable for fluids that can be considered continuous and interpenetrating, rather than discrete. Typically, one of the phases would be considered to exist as unresolved modeled droplets or bubbles within another. The phases can interact both in terms of the drag and lift forces acting between them, but also in terms of heat and mass transfer, such as inter and intra phase reactions, and wall and bulk boiling. Dispersed particle flows can also be modeled as an Eulerian phase, allowing applications such as granular flows in fluidized bed reactors to be simulated (Abdulmouti, 2014).

In general, Eulerian model is a lightweight multiphase model that solves a single set of transport equations for the momentum, mass and energy transport of a mixture, which is made of a liquid and it's vapor.

3.5.3 VOF Model

VOF model can model two or more immiscible fluids by solving a single set of momentum equations and tracking the volume fraction of each of the fluids throughout the domain. Typical applications of VOF model are the prediction of jet breakup, the motion of large bubbles in a liquid, the motion of liquid after a dam break, and the steady or transient tracking of any liquid - gas interface (Fluent Inc., 2006).

Similarly to Mixture Model, VOF model can only be used with a pressure-based solver. Also, it cannot detect void regions, where no fluid of any type is present.

3.6 Meshing

As discussed at previous chapters, a computational grid is required in order for the equations to be applied at the determined points at the problems geometry and be solved. The grid is the most important aspect of a problem as it can determine the

solution accuracy, the rate of convergence and the computer powered needed to solve the problem. Also, its mesh is unique for each geometry.

A computational grid can be either a 2 dimensional or 3 dimensional depending of the solvers needs. At 3d case, it consists of cells that are the control volume into which the domain is broken up. In the center of the grid, all equations are applied as explained in chapter 3.3.3. Cells, faces and nodes can be grouped together to form a zone such as a wall boundary zone or a fluid cell zone. In general, zones are applied at a problem to be able to determine the boundaries of the geometry or create different style and dense grids in the same domain.

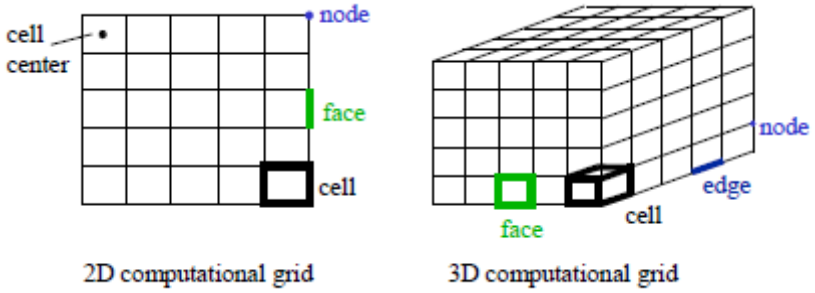

Figure 3.11 Computational grid example

3.6.1 Cell Shapes

Most typical 2D cell shapes are triangles, referred as “tri” and rectangular prisms referred as quadrilaterals or “quads”. Those shapes can follow the curvature of an edge and can get expanded into 3 dimensions to forms 3D grids.

Figure 3.12 2D cell shapes

Moving to 3 dimensions, the shapes of the grid’s cells can be pyramids, triangle based tetrahedral referred as “tet”, hexahedron prisms with quadrilateral base referred as “hex”, wedges or arbitrary polyhedrons with random shape.

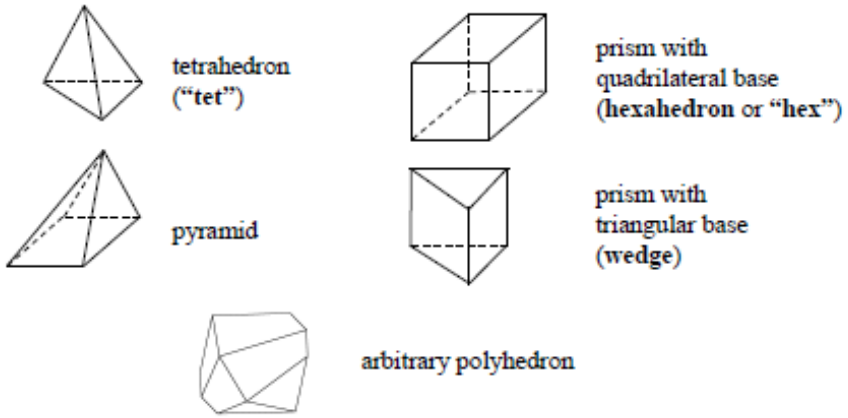

Figure 3.13 3D cell shapes

3.7 Mesh Quality

As discussed a well constructed grid is essential for an accurate and able to converge solution. Thus, the mesh density has to be high enough to capture all relevant flow features.

Preferably, hexahedral elements will achieve a better solution over any other cell shapes and in boundary layers quad, hex and wedge/prism shapes are more appropriate. For an additional accuracy, it will be better if the grid lines are aligned with the flow.

3.7.1 Near Wall Modeling

As discussed in chapter 1.7, due to the effect of viscosity and friction, near walls, a boundary layer is developed. That layer has a very small width and has a tremendous effect on the overall flow.

Near-Wall Model Approach

In order to capture that layer in detail, a higher density mesh has to be developed near walls.

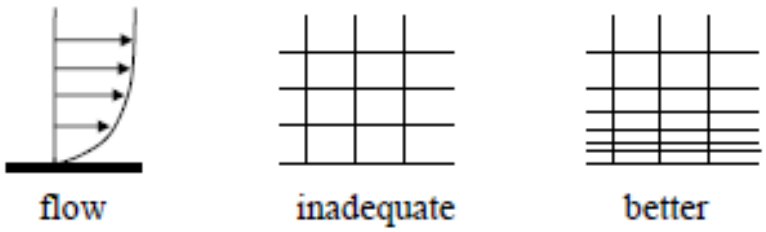

Figure 3.14 Grid near a wall

Y plus or, as noted, y^+ is a non-dimensional number determining whether the influences in the wall-adjacent cells are laminar or turbulent. Hence, y^+, indicates the part of the turbulent boundary layer that they resolve (Salim, et al., 2009).

$$y^+ = \frac{u_* y}{v} \tag{136}$$

Where y, the distance to the nearest wall and u_* the friction velocity given by the following equation:

$$u_* = \sqrt{\frac{\tau_w}{\rho}} \tag{137}$$

Where τ_w and ρ the shear stress and the density at the wall. The wall shear stress is given by solving equation (22) at the wall.

$$\tau_w = \mu \left(\frac{\partial u}{\partial y}\right)_{y=0} \tag{138}$$

The subdivisions of the near-wall region in a turbulent boundary layer can be summarized as follows (Fluent Inc., 2006):

a) $y^+ < 5$: in the viscous sublayer region, velocity profiles is assumed to be laminar and viscous stress dominates the wall shear

b) $5 < y^+ < 60$: buffer region, both viscous and turbulent shear dominates

c) $60 < y^+ < 300$: full turbulent portion or log-law region, corresponds to the region where turbulent shear predominates

By knowing the type of region at any given distance near the wall, the first node and the size of, it can be set appropriately to capture the necessary features of boundary layer.

Wall Function Approach

Another common approach, is by using semi-empirical formulas and functions that in effect "bridge" or link the solution variables at the near-wall cells and the corresponding quantities on the wall. The wall functions compromise laws-of-the-wall for mean velocity, temperature or any other scalar variable and formulas for near-wall turbulent quantities (Fluent Inc., 2006). Each commercial software provides deferent set of equations for wall function.

Wall function approach is being used with hi-Re turbulent models, such as k-ε and k-ω models. Thus, constructing a grid according to y^+ factor is not needed, as an assumption of y^+ is made at the first point above the wall to be at least one order of

magnitude larger. Although, when constructing a mesh, y^+ should be used as an indicator in order for the solver to be able to solve the boundary layer appropriately.

3.7.2 Skewness

Skewness is measured based on the deviation from a normalized equilateral angle as seen in Figure 3.15.

$$Skewness_{quad} = \max\left[\frac{\theta_{max} - 90}{90}, \frac{90 - \theta_{min}}{90}\right] \quad (139)$$

An alternative measurement method that is used for tris and tets is the following

$$Skewness = \frac{optimal\ cell\ size - cell\ size}{optimal\ cell\ size} \quad (140)$$

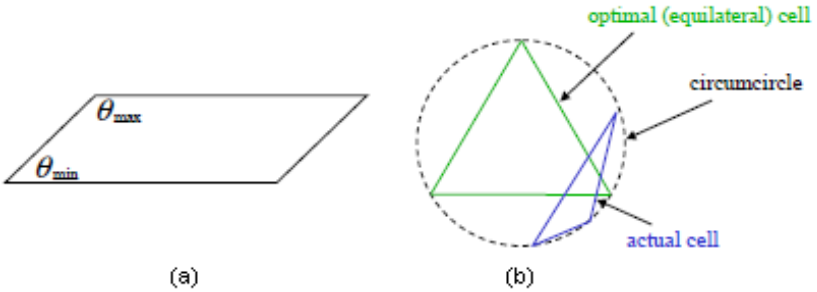

Figure 3.15 Skewness based on: (a) the deviation from a normalized equilateral angle, (b) equilateral volume

Therefore, a common measure of quality is derived, based on equiangule skew:

$$Skewness = \max\left[\frac{\theta_{max} - \theta_e}{180 - \theta_e}, \frac{\theta_e - \theta_{min}}{\theta_e}\right] \quad (141)$$

Where $\theta_e = 60^o$ for triangle and $\theta_e = 90^o$ for square faces or cells.

A general guide for skewness quality is described in Table 3.2. For hex, tri and quad cells, skewness values should not exceed 0.85. For tet cells the value of skewness should not be more than 0.9

Skewness	0-0.25	0.25-0.50	0.50-0.80	0.80-0.95	0.95-0.99	0.99-1.00
Quality	Excellent	Good	Acceptable	Poor	Sliver	Degenerate

Table 3.2 Categorized values of skewness

3.7.3 Aspect Ratio

Aspect ratio determines the ratio of the longest edge length compared to shortest one as seen in Figure 3.16.

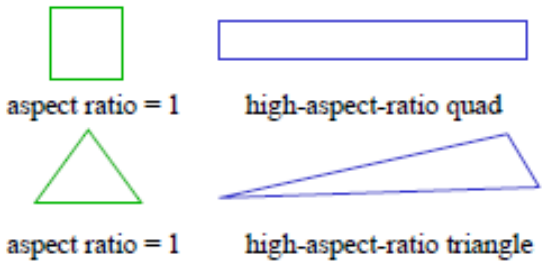

Figure 3.16 Aspect ratio comparison between various shapes

Aspect ratio should be kept as higher as possible (close to the value of 1) in order for the computational nodes to be spread more uniformly through the domain.

3.7.4 Smoothness

Smoothness is referred to the change of size in nearby cells. For better quality, when the increase of cells' size is required, it shouldn't be at instant but gradually in order to achieve better results.

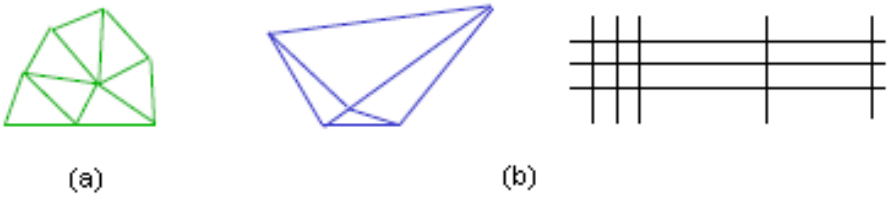

Figure 3.17 Smoothness examples: (a) Smooth change in cell size, (b) sudden change in cell size

Ideally, the maximum change in grid spacing should not be higher than 20%.

$$\frac{\Delta x_{i+1}}{\Delta x_i} \leq 1.2 \tag{142}$$

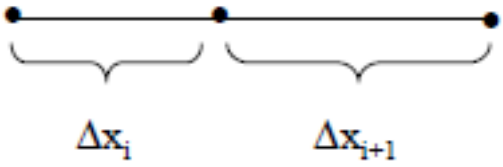

Figure 3.18 Size difference between 2 cells

Part II:
Experimental Procedure

4 Geometry Review[8]

To begin with, a test rig was design in order to measure both cavitation and jet dispersion (at future test experiments). The main goal of the rig construction, was to create a rig that the flow at the points of interests will be random, similar to a diesel fuel nozzle.

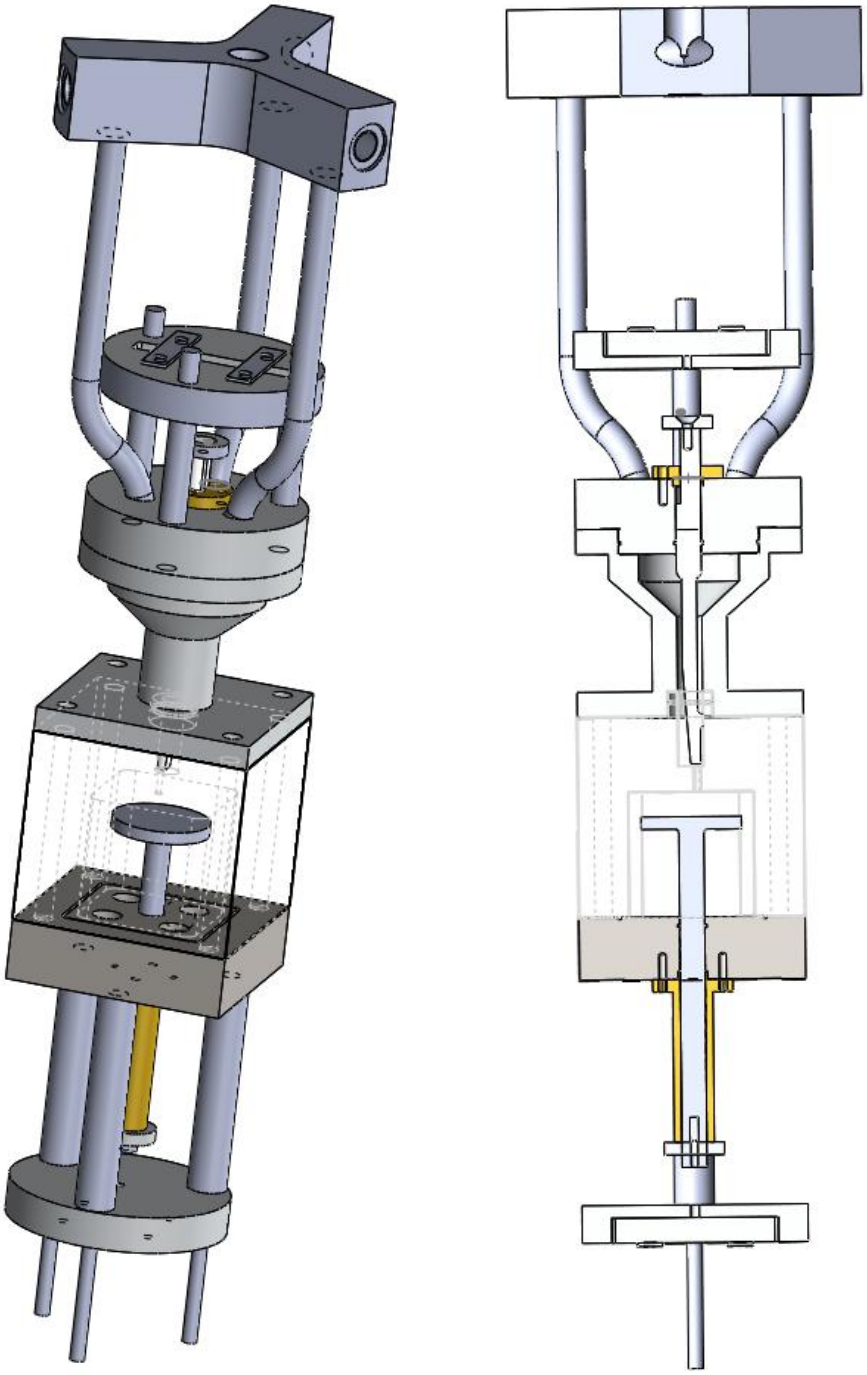

Figure 4.1 Cavitation Test Rig: (a) Isometric view, (b) Section view

[8] Complete set of schematics can be found at the end of the documentation

At the top of the rig, there is a cylindrical inlet of $15.25\ mm$ diameter. Upon entering, the fluid is travelling downside for a few millimeters and then splits up to three vertically tubes of $11.8\ mm$ diameter. Then, each tube ends up into a curved pipe travelling downside into the main area. All pipes are ending into a cone shaped area which converges into a $10\ mm$ diameter tube. At the end of that tube a smaller tube is placed, with an offset of $2.5\ mm$ and $3\ mm$ diameter which is the point of interest of the whole rig. In the center of the larger tube, starting from the cone-shaped area, a special-shaped needle is placed. The end of the needle is placed $1\ mm$ above the small tube, although the position if it can be adjusted by a micrometer attached to the other end of the needle. The needle's role is to create an asymmetrical flow right above the small tube and create a sharp change of the flow.

At the end of the smaller hole a large chamber of acrylic is placed and just below the end of the tube, a plate which can be used to measure particle dispersion of a jet stream in other experiments. The distance of the plate compared to the tube's end can be adjusted with a micrometer adjusted at one end of the plate. At the bottom of the acrylic chamber there are four outlets of $12\ mm$ diameter.

According to simulation results, bypass tubes have been added in order to eliminate cavitation inception that appeared at a side of a wall at the smaller tube. Totally

4.1 Control Volume

In order to reduce complexity and computer power needed for the CFD part, some parts of the rig have been removed. Thus, the control volume starts from the cone-shaped area until the bottom of the acrylic chamber.

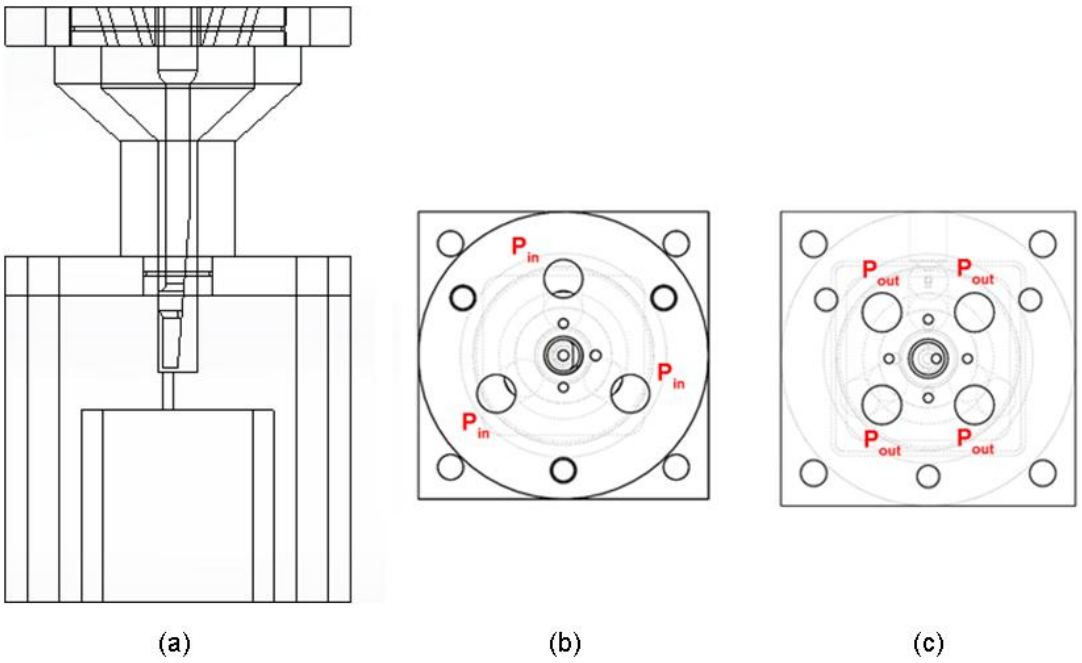

Figure 4.2 Control Volume sketches: (a) Section view, (b) Top view, (c) Bottom view

5 Solver Setup

The commercial “Fluent” solver by ANSYS has been used to run the CFD analysis. The first step to set up the solver was to scale the imported mesh in order for it, to be compatible with the original geometry.

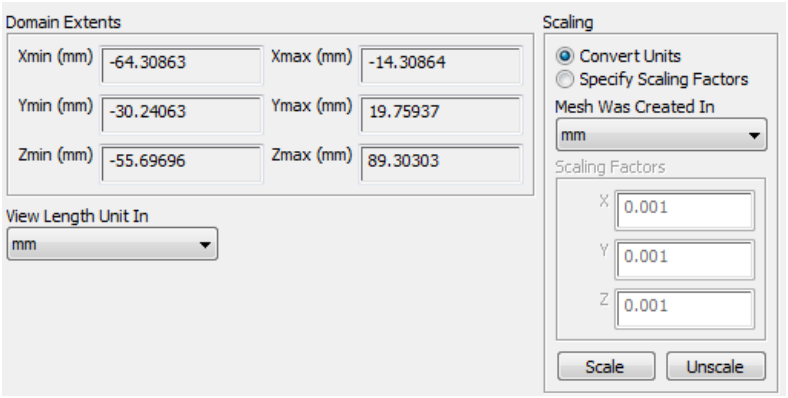

Figure 5.1 Domain scaling

After that the turbulent model wad determined by choosing the realizable $k-\varepsilon$ model with an enchant wall treatment option which offers a two-layer model with enhanced wall functions (Fluent Inc., 2006), able to increase accuracy near walls where cavitation inception will occur. The rest of the model variables have been set to default.

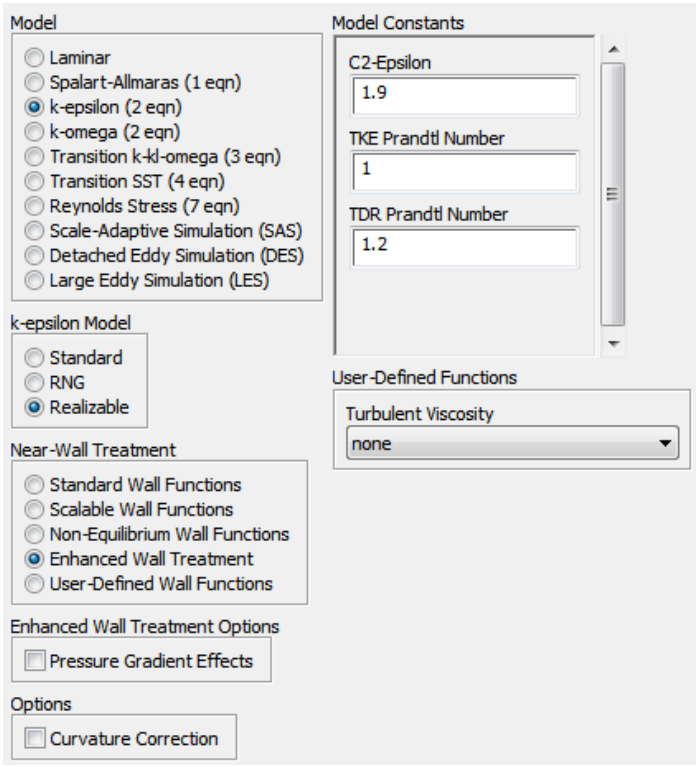

Figure 5.2 Turbulent model

Furthermore, for multiphase modeling, the mixture model has been selected with 2 discrete phases of vapor and fluid.

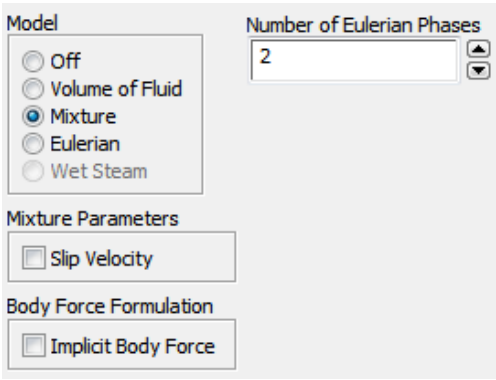

Figure 5.3 Multiphase model

For the solid part of the construction, common aluminum has been used. As the fluid, Diesel with chemical formula of $C_{10}H_{22}$ has been chosen. The properties of those elements were determined by Fluent's material library and can be seen in Figure 5.4.

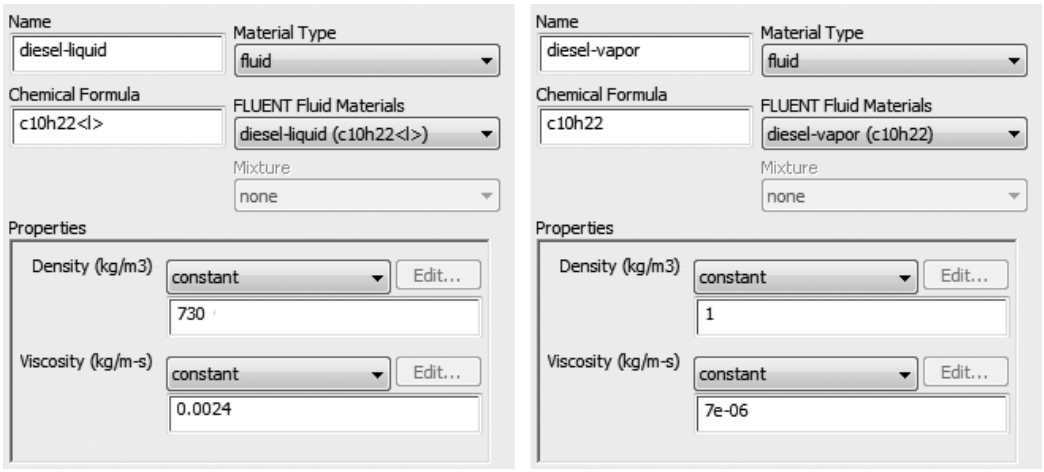

Figure 5.4 Material properties: (a) Liquid Diesel, (b) Vapor Diesel

After setting up the materials for the simulations, the two phases have to be set up separately. The liquid phase has been set up as the primary phase of the flow and the vapor phase as the secondary one. Also, the interaction between those phases has been set to mass transfer, from liquid to vapor through the process of cavitation mechanism. The simple cavitation Schnerr - Sauer model using the default parameters.

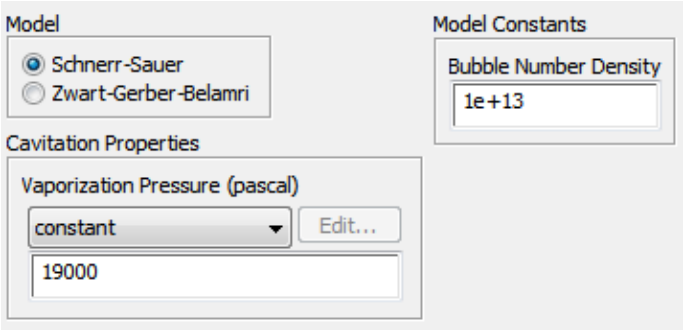

Figure 5.5 Cavitation model

In addition, the boundary conditions have been set as pressure inlets and outlets of $50\ bar$ and $1\ bar$ pressure respectively as seen in Figure 5.6.

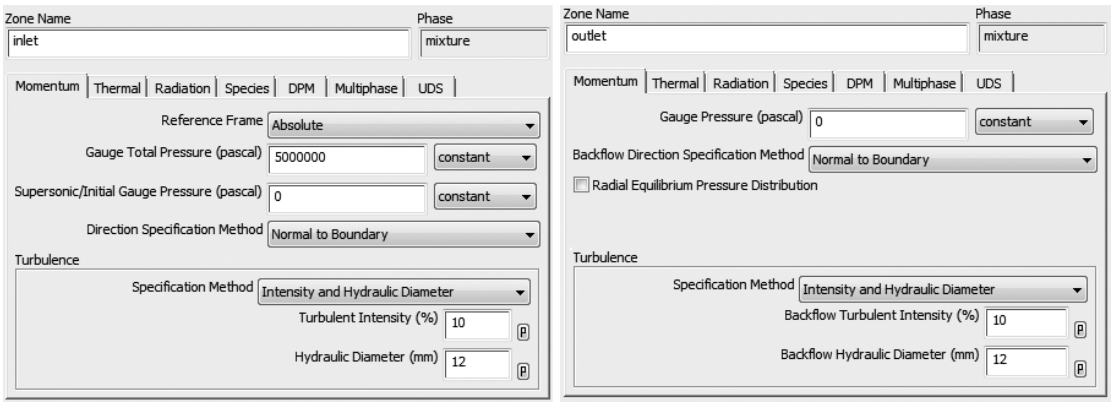

Figure 5.6 Boundary conditions: (a) Inlet, (b) Outlet

Also, all cases have run for the first few iterations (approximately 1000-1300 iterations) as a single phase models and then the multiphase model was used until convergence.

Finally, the solution method for pressure-velocity coupling and special discretization as well as under-relaxation factors have been set as seen Figure 5.7.

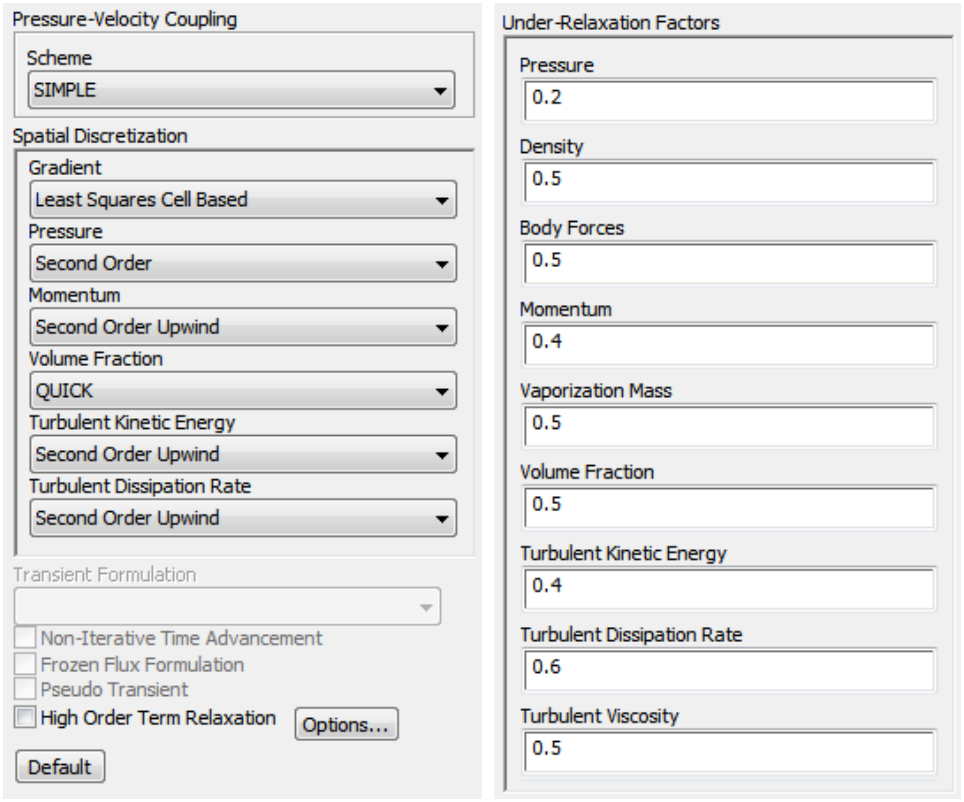

Figure 5.7 Solution parameters: (a) Solution method, (b) Under-relaxation factors

Part III:
Results Overview

6 Results

For post and pre processing ANSA and μETA of BETA CAE SA software packages have been used.

6.1 Case I: Single Hole

"Single hole" case is the simplest form in terms of geometry complexity, of all cases that have been examined. All the other cases have derived from that one, thus it will be used for comparison against other cases later on.

6.1.1 Geometry Overview

At "single hole" case, the geometry was kept the same, as reviewed at chapter 4. The needle is placed $1\ mm$ above the entrance of the tube as seen at Figure 6.1.

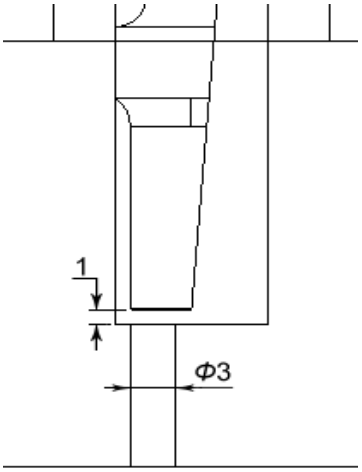

Figure 6.1 Case I: Single hole sketch

Cavitation inception is expected at the right side of the tube (following Figure 6.1 orientation) as the angle the flow has to follow is sharp and will result at a pressure drop at that region. Similarly, cavitation inception might occur at the bottom of the needle too due to the sharp angle.

6.1.2 Mesh Overview

The single hole case has approximately 3800000 elements. Around the area of interest, there is an increased density of elements compared to the rest domain. A surface is placed at the bottom of the tube, separating the tube from the chamber below of it. The surface was set as "interior" at boundary conditions field at solver software (Fluent). In result, the chamber bellow the tube, have been meshed separately, with a reduced density of elements, as there was no need for high accuracy results at that region. In addition, a minimum of 8 elements for each line of elements perpendicular to the flow had been set, in order to achieve better results.

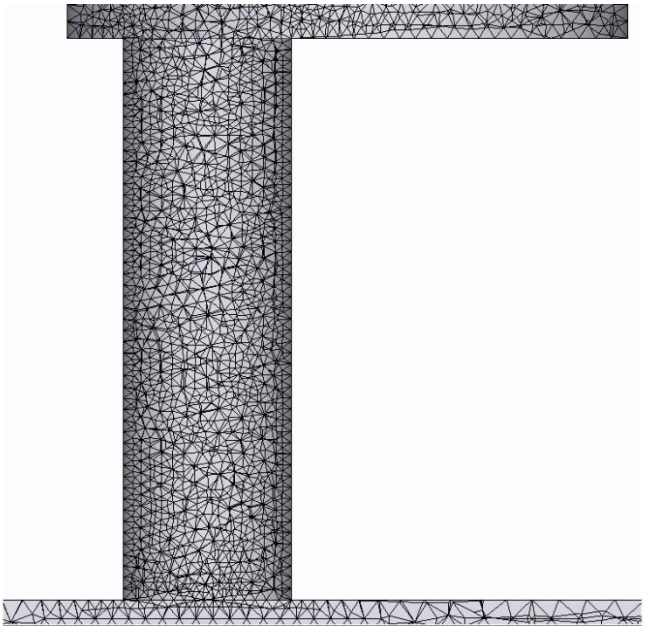

Figure 6.2 Case I: Mesh

6.1.3 Results

By applying Bernoulli's equation (19) at inlets and outlets, a theoretical mass flow value $\dot{m}_B$ can be calculated. Then, it can be compared to the mass flow rate derived by solving the CFD problem $\dot{m}_{fl}$ and use it to compare different cases.

$$CD = \frac{\dot{m}_{fl}}{\dot{m}_B} = \frac{0.32\ Kg/s}{0.6\ Kg/s} = 0.534 \tag{143}$$

Also, the cavitation number can be calculated by the following equation:

$$CN = \frac{P_{inlet} - P_b}{P_b - P_v} = \frac{50 \cdot 10^5 - 1 \cdot 10^5}{1 \cdot 10^5 - 19000} = 60.5 \tag{144}$$

As it can be seen in Figure 6.3, a high pressure jet is created inside the tube of nearly $120\ m/s$ along with a sudden pressure drop. The result of that interaction is a cavitation cloud attached around the tube's walls, starting from the region near the throttling gap till the end of the tube, as seen in Figure 6.5.

Also, it is worth mentioning that the mesh was not suitable for achieving better accuracy especially near tube's wall and at the end of the jet stream as seen in Figure 6.5b.

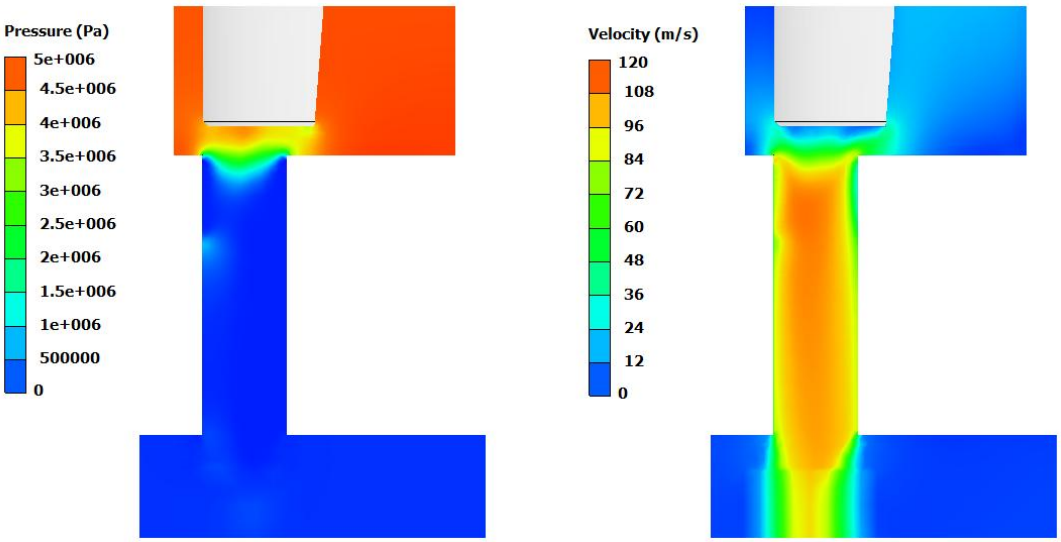

Figure 6.3 Case I: (a) Pressure plot, (b) Velocity plot

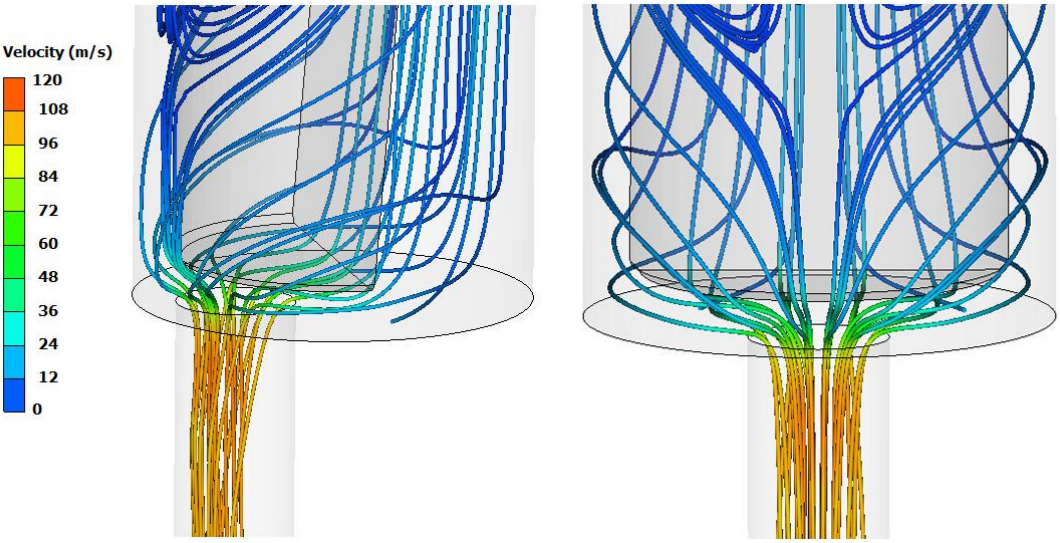

Figure 6.4 Case I: Velocity stream lines

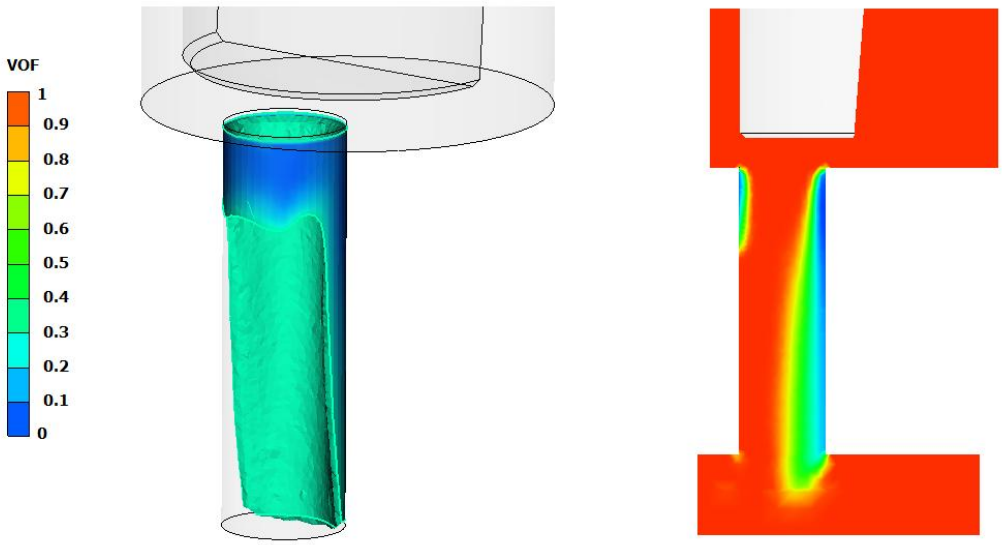

Figure 6.5 Case I: (a) VOF IsoFun (b) VOF plot

6.2 Case II: Single Bypass

6.2.1 Geometry Overview

At "single bypass" case, a small $0.5\ mm$ tube was added, $3.6\ mm$ from the center of the tube and a slope of 35^o as seen in Figure 6.6. The small tube was placed in such a way that the distance from each tube center measured on the top plane of the main tube, would be equal to 1.2 time the diameter of the main tube. The needle has been kept at the same distance of $1\ mm$, as well as the rest geometry that was kept unchanged. The angle of the added tube was limited, as there was not enough space for the CNC machine to drill at bigger angle.

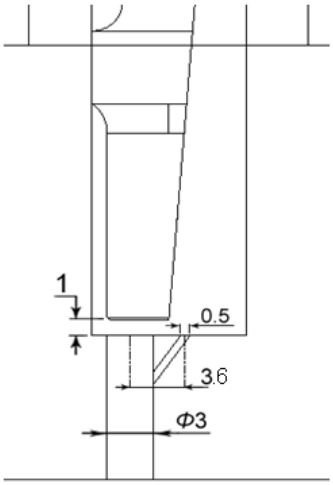

Figure 6.6 Case II: Single bypass sketch

The main purpose of tube's introduction was to create a flow bypass in order to connect the low-pressure area which resulted to cavitation inception to a higher-pressure area, which eventually will result to the elimination of cavitation inception.

6.2.2 Mesh Overview

The "single bypass" case has approximately 3900000 elements. The density of elements near the tube has been increased even more in order to achieve better results and similarly to the previous model a surface is separating the bottom chamber from the tube in order to reduce the computational nodes of the domain. The limit of 8 elements for each line of elements perpendicular to the flow has remained the same. In the bypass tube, the limit of 8 elements per line was increased to 10.

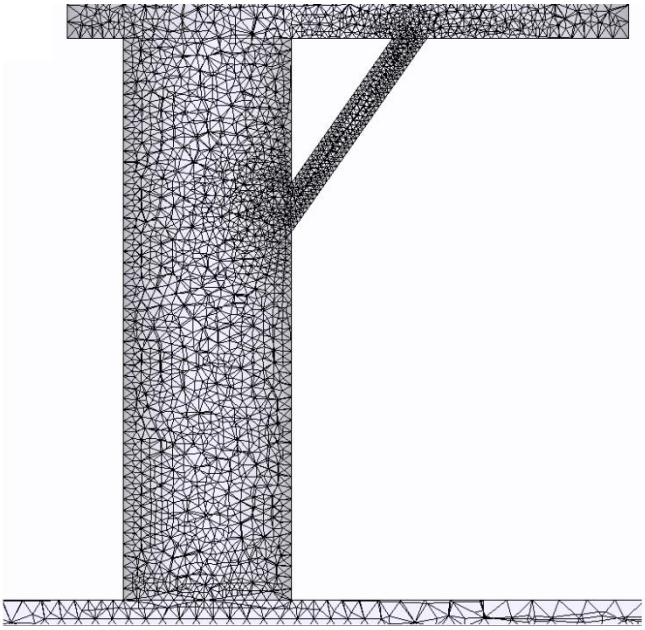

Figure 6.7 Case II: Mesh

6.2.3 Results

By calculating the flow's feature it can be noticed that the mass flow rate has increased only by 3%, which is a relatively small value and can be consider computational error. Thus, despite of the introduction of the bypass tube the mass flow rate remains unchanged.

$$\begin{cases} \dot{m}_{fl} = 0.33\ Kg/s \\ CD = 0.55 \\ CN = 60.5 \end{cases}$$

Despite of the introduction of the bypass tube, the main distribution of the flow remains the same. Pressure drop plot near the hole is the same and there is a slightly variation at the velocity distribution. A similar jet effect is generated compared to case I, while the velocity distribution is slightly changed as a result of the introduction of the bypass tube. Inside the bypass tube, a high speed flow is generated as well resulting in a get exiting the tube with high speed. Also, cavitation inception is observed inside the bypass tube which is a result of high pressure drop. The cavitation inside the main tube is not affected at any means probably due to the high speed of the fluid exiting the bypass tube, as seen in Figure 6.11.

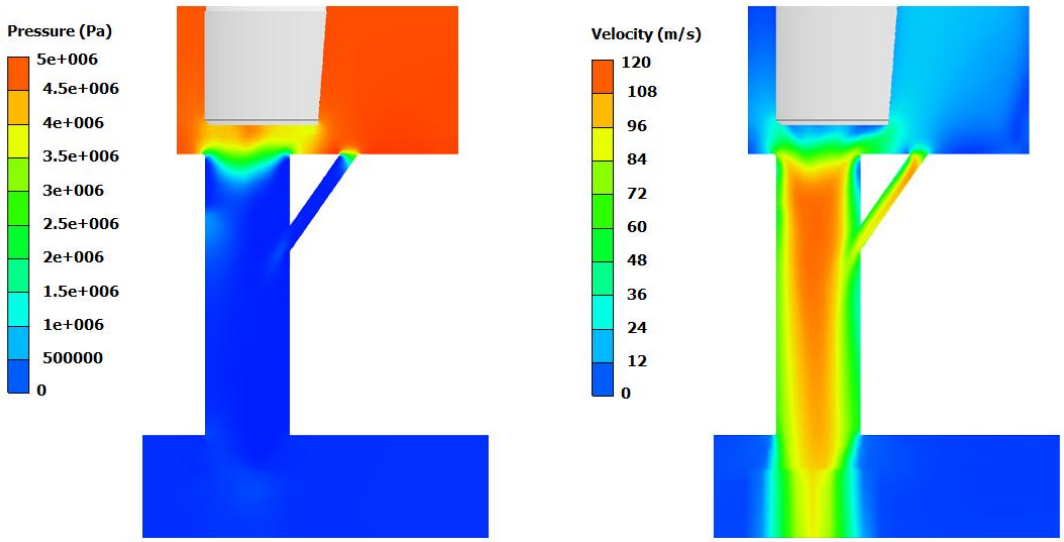

Figure 6.8 Case II: (a) Pressure plot, (b) Velocity plot

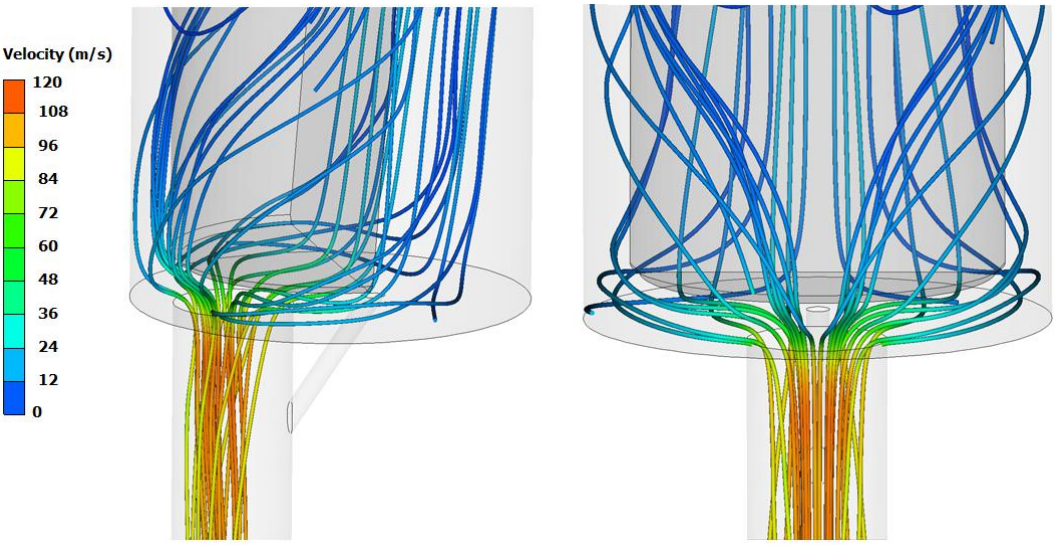

Figure 6.9 Case II: Velocity stream lines

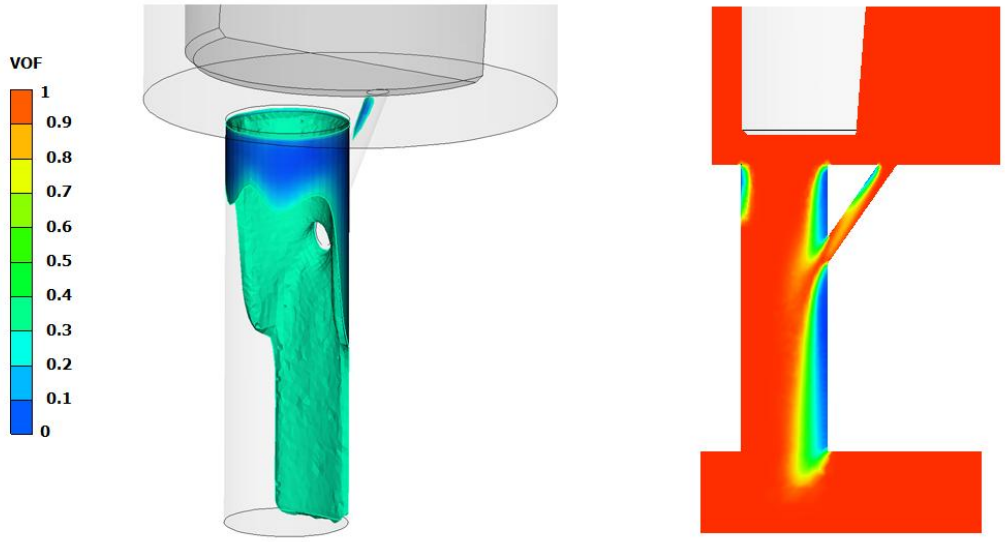

Figure 6.10 Case II: (a) VOF IsoFun (b) VOF plot

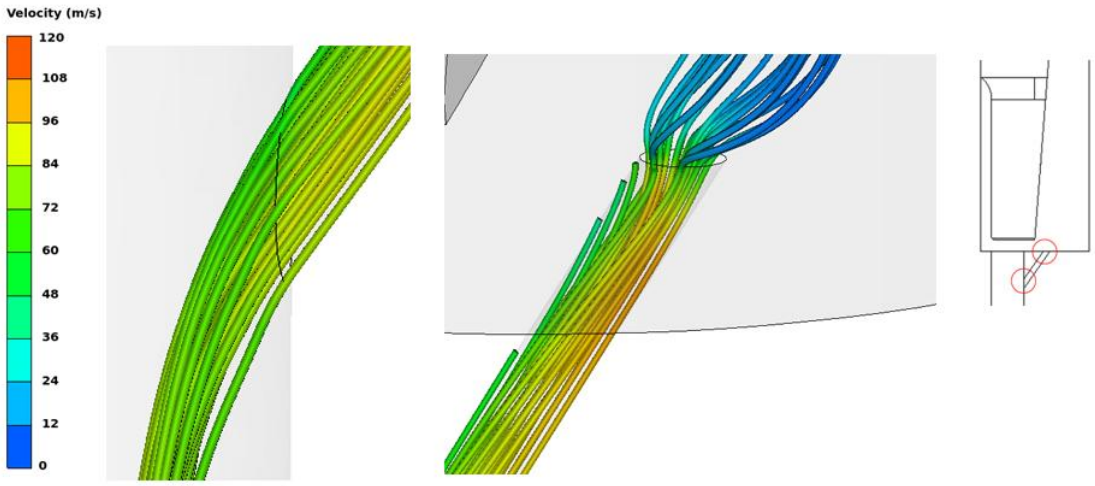

Figure 6.11 Case II: Streamlines at (a) the exit and (b) the entrance of the bypass tube

6.3 Case III: Single Bypass (Short)

6.3.1 Geometry Overview

At "single bypass - short" case, the length of the bypass tube added at case II was reduced to $2.12\ mm$ from the center of the tube. The bypass tube was placed in a way that the virtual extend of the bypass tube, will be tangent to the needles edge close to throttling gap.

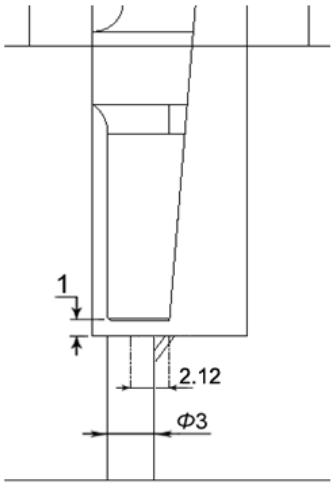

Figure 6.12 Case III: Single bypass (short) sketch

The redaction of the bypass tube's distance from the center of the main tube was expected to eliminate cavitation as it will intersect the near the leading edge with a higher pressure area. Also, it is expected that the fluid will move with a lower velocity inside the tube as the pressure difference of the entrance of the bypass tube compared to the exit will be smaller.

6.3.2 Mesh Overview

The “single bypass (short)” case has approximately 3750000 elements. The density of the mesh was kept approximately the same but boundary layers have been added at tube’s and bypass tube’s walls in order to achieve better results near the walls. In contrast with precious models, the interior surface at the bottom of the tube was removed and was meshed alongside the main domain, in order increase the quality of the results at the end of the jet stream.

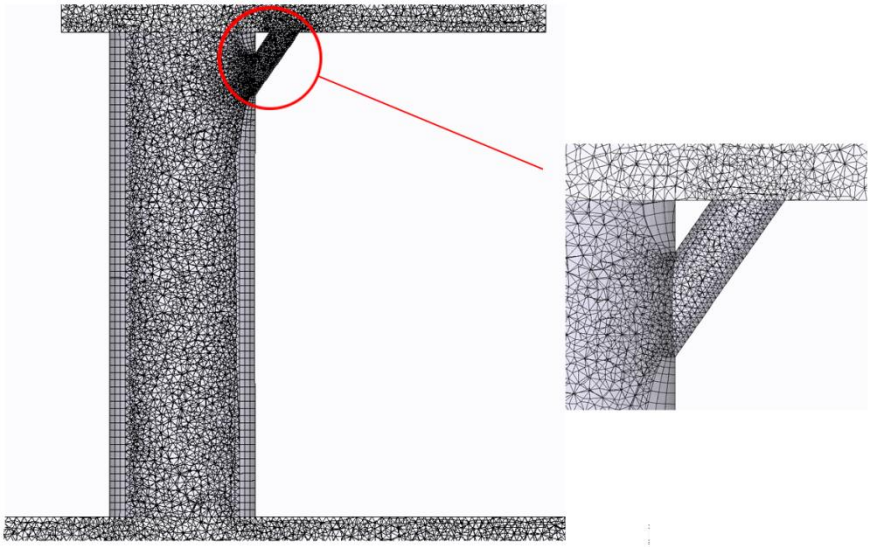

Figure 6.13 Case III: Mesh

6.3.3 Results

The mass flow rate was increased by 6.3%. Thus, it can due to the introduction of the bypass tube the sum of the throttle diameter was increased slightly and there is less resistance for the fluid to pass through.

$$\begin{cases} \dot{m}_{fl} = 0.34\ Kg/s \\ CD = 0.57 \\ CN = 60.5 \end{cases}$$

As it can be seen in Figure 6.14, a larger jet is formed in the bypass tube compared to Case II. Due to the high velocity that the fluid is exiting the bypass tube, cavitation place is still taking place at the main tube. Also, traces of cavitation inception can be seen inside the bypass tube as well. As it seems, the reduction of the length of the bypass tube didn’t help for the elimination of cavitation inception in the main tube.

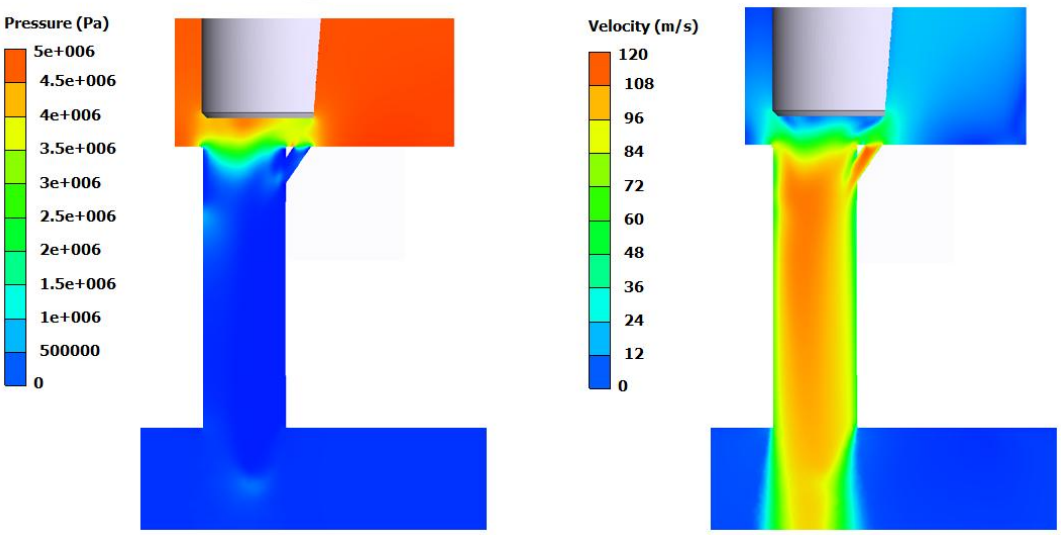

Figure 6.14 Case III: (a) Pressure plot, (b) Velocity plot

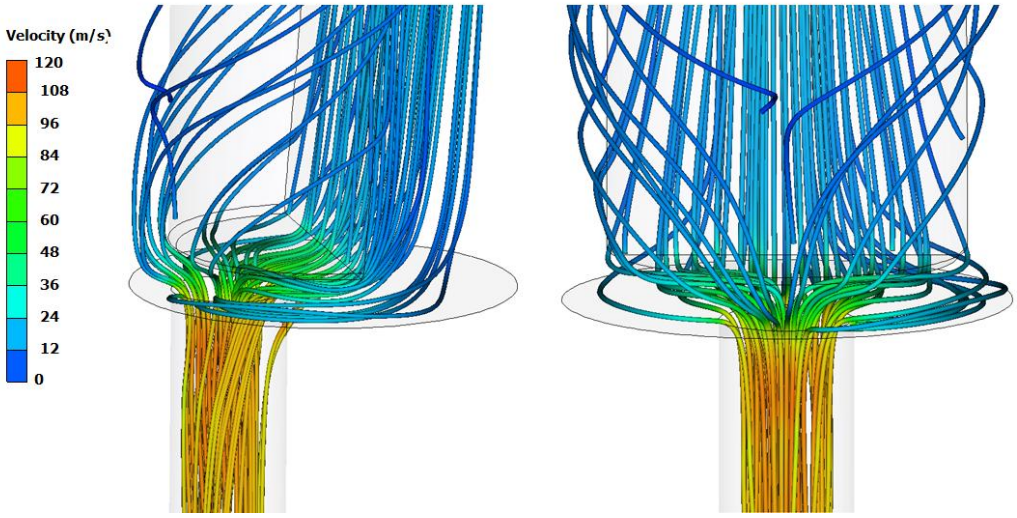

Figure 6.15 Case III: Velocity stream lines

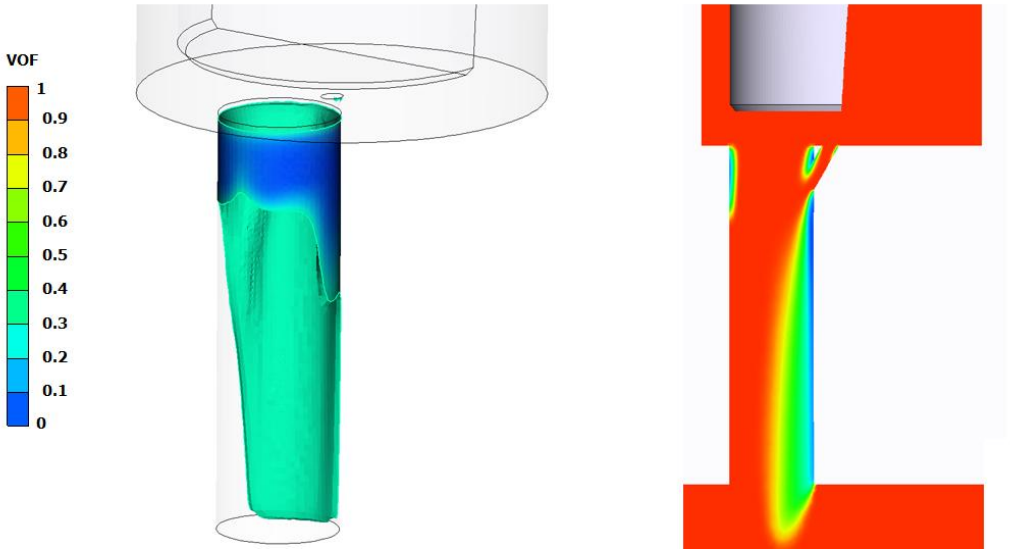

Figure 6.16 Case III: (a) VOF IsoFun (b) VOF plot

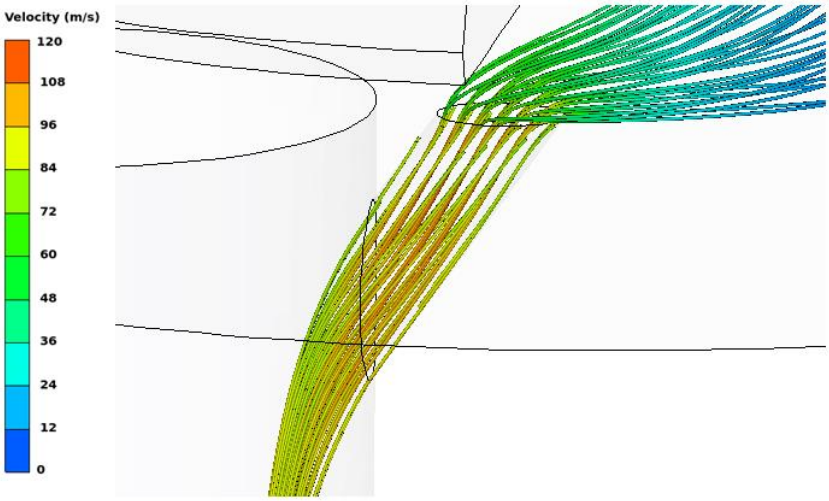

Figure 6.17 Case III: Streamlines of bypass tube

6.4 Case IV: Triple Bypass (Short)

6.4.1 Geometry Overview

At "triple bypass - short" case, the same bypass cube was kept at the minimal distance of $2.12\ mm$ from main's tube center. Also, two more identical tubes were added, placed radially from the center of the main tube. The three bypass tubes were placed 1.5 times each diameter measured from the center of the entrance of each tube. Using the arc length equation $l = 2\pi R \frac{a}{360^o}$, where R the distance between each center, l the arc length which is equal to $1.5d = 0.75\ mm$, the angle a is calculated equal to 20.4^o.

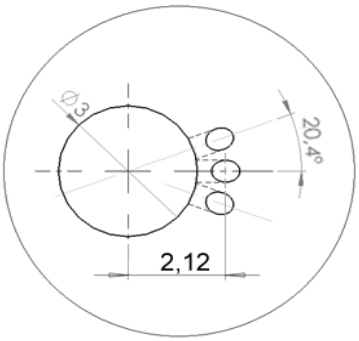

Figure 6.18 Case IV: Triple bypass (narrow) sketch

By introducing 2 more bypass tubes, it is expected to increase even further the pressure drop and eventually eliminate any cavitation inception at that point. Also, by introducing 2 more tubes it is expected for the velocity to drop slightly and create a lower-velocity jet.

6.4.2 Mesh Overview

The “triple bypass - short” case has approximately 4750000 elements. As the number of elements reveals, the density of the mesh has increased a lot. Especially near the area of interest, the density has increased from a minimum 10 elements per line of elements to 15. Also, additional boundary layers have been added near walls.

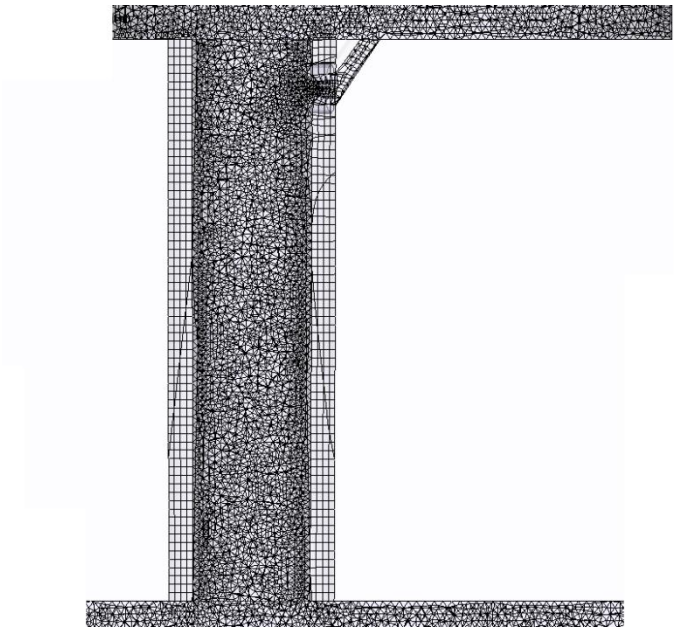

Figure 6.19 Case IV: Mesh

6.4.3 Results

By calculating the flow’s feature it can be noticed that the mass flow rate has increased even more by 9.4%, as explained in case III, the introduction of more tubes will result to the increase of throttles space and increase flow rate.

$$\begin{cases} \dot{m}_{fl} = 0.35\ Kg/s \\ CD = 0.58 \\ CN = 60.5 \end{cases}$$

Despite of the introduction of 2 more bypass tubes cavitation inception still occurs in the main tube. Although, the high speed jet, that is formed into the bypass tubes, has decreased speed compared to previous cases it’s still too fast to block cavitation inception as the pressure transition between high and low pressure regions is still too fast. Also, cavitation inception is still occurring inside all bypass tubes.

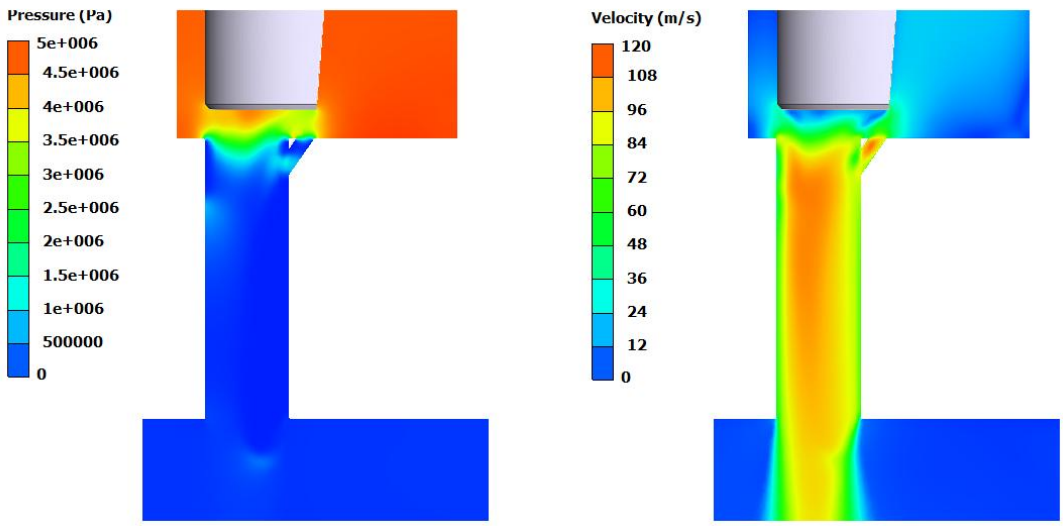

Figure 6.20 Case IV: (a) Pressure plot, (b) Velocity plot

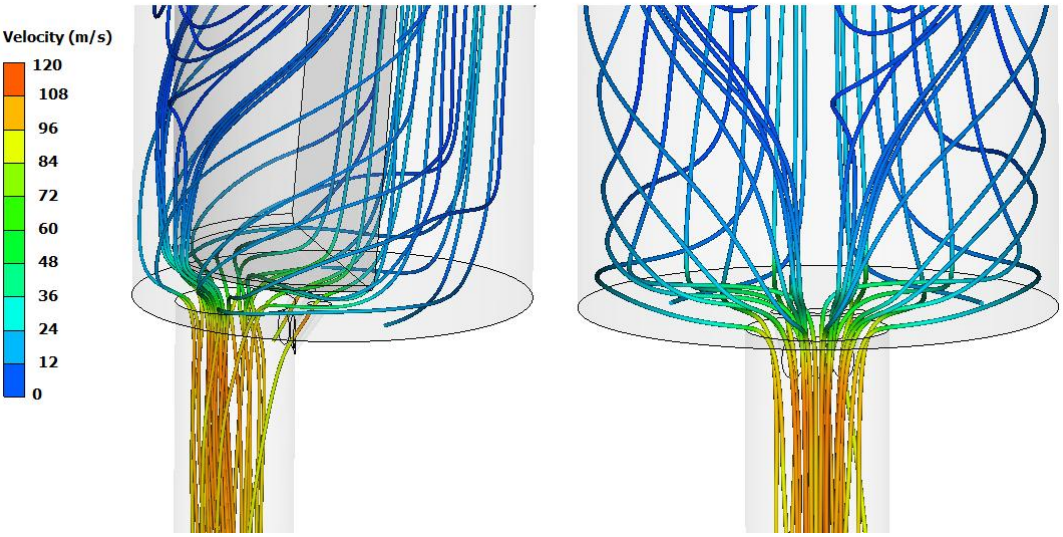

Figure 6.21 Case IV: Velocity stream lines

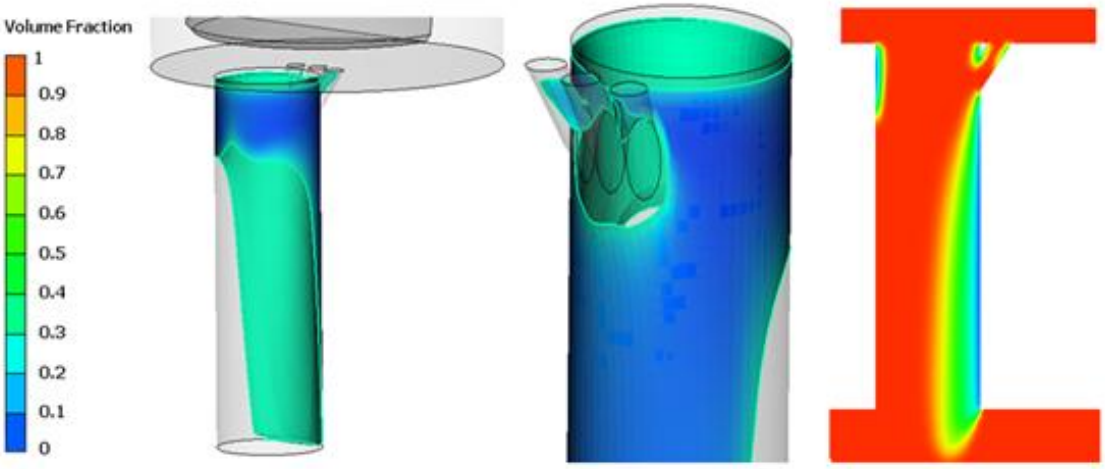

Figure 6.22 Case IV: (a) VOF IsoFun, (b) VOF IsoFun, (c) VOF plot

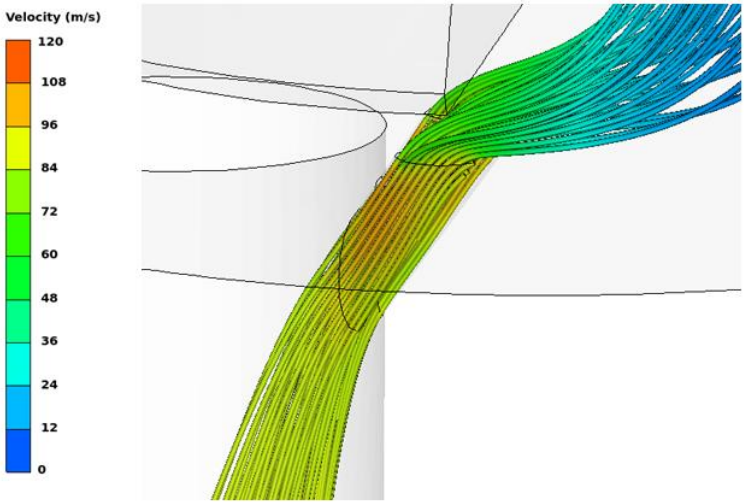

Figure 6.23 Case IV: Streamlines of bypass tubes

6.5 Case V: Triple Bypass (Wide)

6.5.1 Geometry Overview

At "triple bypass - wide" case, the positioning of bypass tubes was increased back to $3.6\ mm$ from main's tube center as the decrease in length didn't decrease cavitation inception. Also, in case IV, it was observed that the three tubes was too close near the walls of the main tube, almost touching each other. So, in case V, the radial distance of the bypass tubes was set to 1.5 times the diameter of each tube but instead of calculating this distance from the entrance of each tube, it was calculated at main's tube walls. Following the same principle as case IV, the arc case for $R = 15\ mm$ gives $a = 38.2^o$.

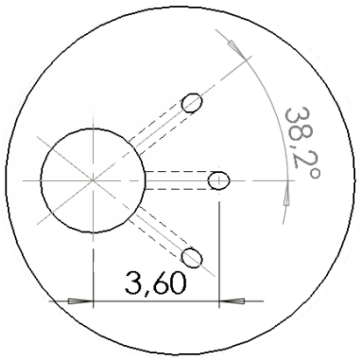

Figure 6.24 Case V: Triple bypass (wide) sketch

By increasing the distance of the entrance of the bypass tubes and the radial distance between each other, a wider area of the low pressure region will connect with higher pressure region and is expected to have a greater impact on cavitation inception.

6.5.2 Mesh Overview

The “triple bypass - wide” case has approximately 2500000 elements. Although the number of elements decreased significantly, the “quality” of the mess was increased a lot. The mesh is generally better structured, as more tet-shaped elements were used and when possible mapped-type meshed was used. The width of boundary layers was decreased which resulted to better y^+ values. Also, boundary layers were added at the rest of the domain, around needle and at the larger tube where the needle was placed. The chamber bellow the main tube was meshed separately by placing an interior surface as cases I and II, although higher density mesh were constructed bellow the main tube in order capture the jet that is created in detail. Furthermore, a mapped mesh was used for the chamber region. Those techniques reduced at nearly a half the number of elements while maintaining a well structured mesh.

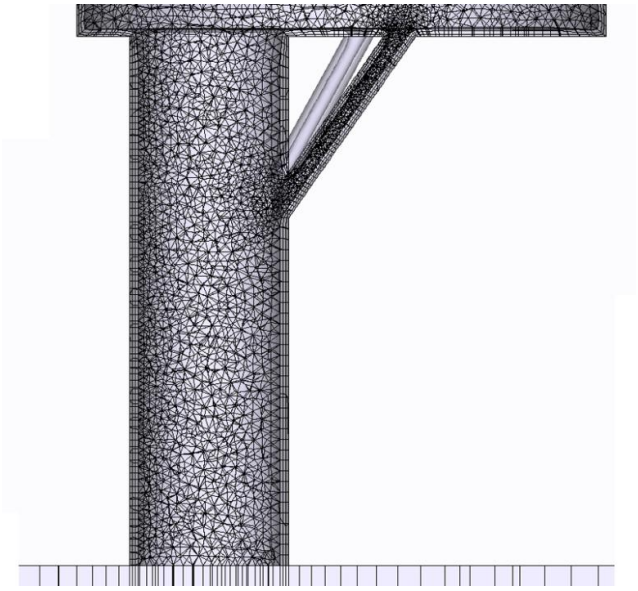

Figure 6.25 Case V: Mesh

6.5.3 Results

Instead of running the standard procedure for the geometry, it was decided to run simulations for both $5\ bars$ and $10\ bars$ back pressure. The geometry and the mesh should be kept the same and conclusively be able to understand in a better way the reasons of cavitation in the tube and how the pressure difference can affect the cavitation inception.

Back Pressure: 1 Bar

By following the same procedure, the mass flow rate is found 12.5% increased compared to case I.

$$\begin{cases} \dot{m}_{fl} = 0.36\ Kg/s \\ CD = 0.6 \\ CN = 60.5 \end{cases}$$

As it can be seen in Figure 6.26, high speed jet in bypass tubes is still formed. Although, the speed of the jet exiting the tube is slightly slower than previous cases, it's not slow enough to stop cavitation inception. Pressure plot looks similar to other cases with a fast pressure drop occurring at the entrances of the tubes. Similarly with other cases, cavitation inception both at the main tube and bypass tubes didn't affected as expected.

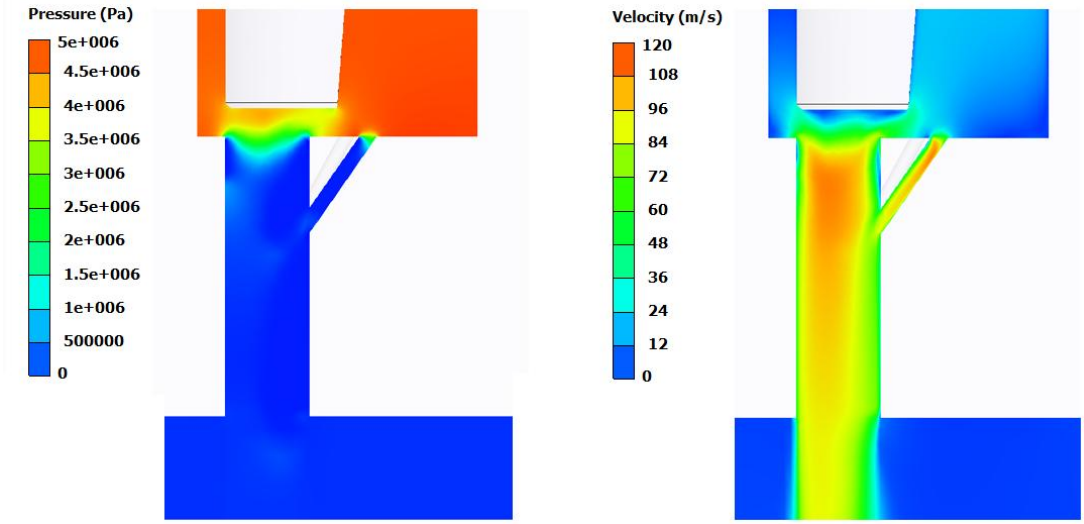

Figure 6.26 Case V: (a) Pressure plot, (b) Velocity plot

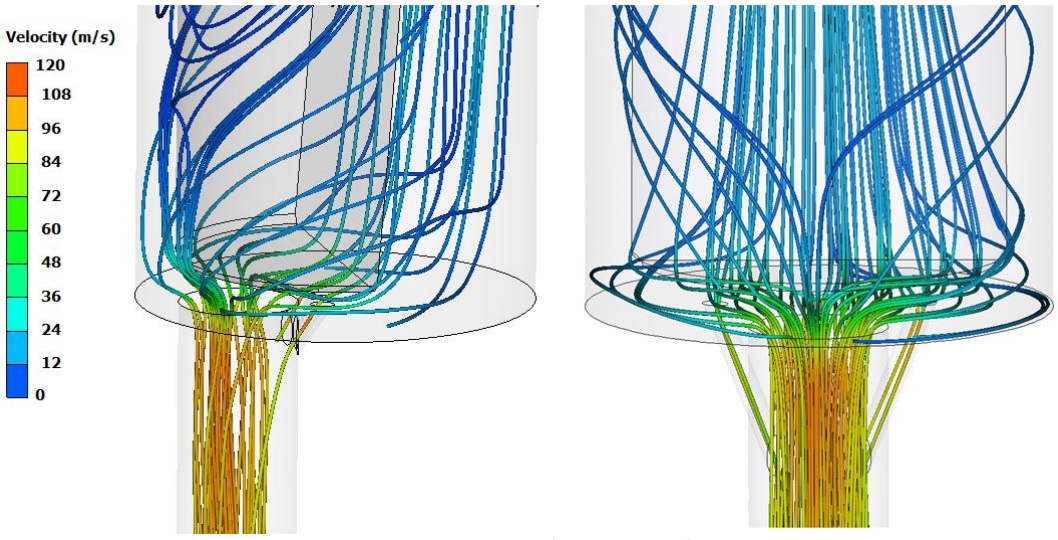

Figure 6.27 Case V: Velocity stream lines

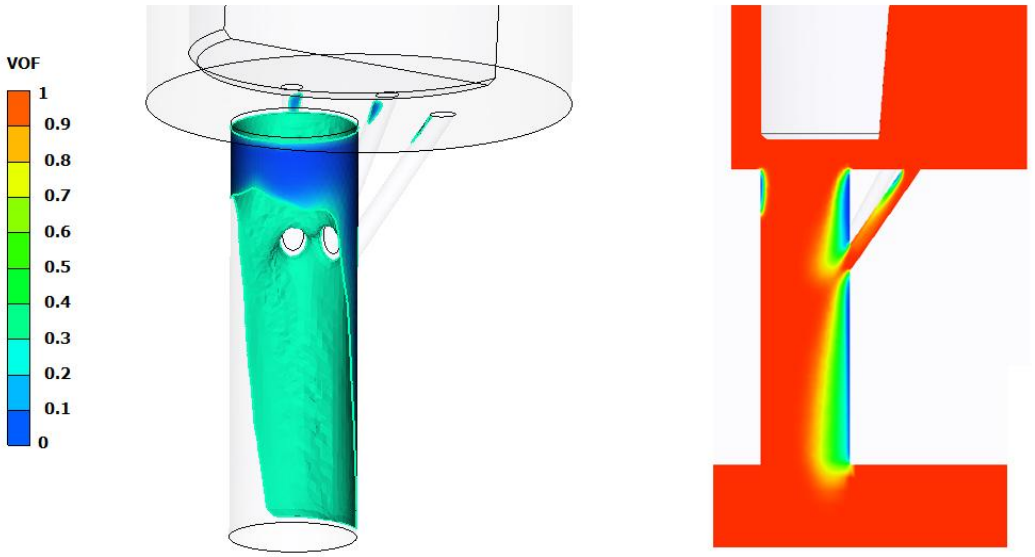

Figure 6.28 Case V: (a) VOF IsoFun, (b) VOF plot

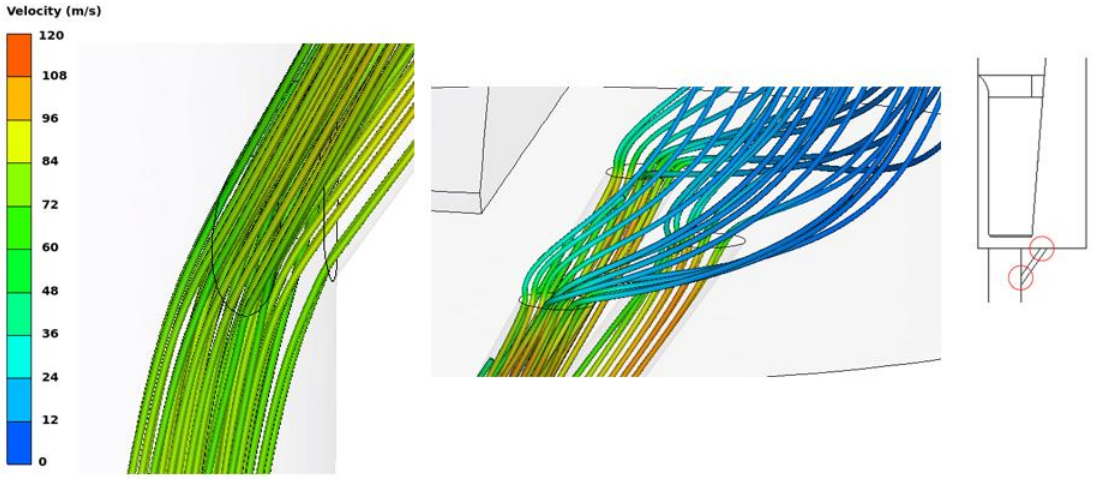

Figure 6.29 Case V: Streamlines at (a) exits and (b) entrances of bypass tubes

Back Pressure: 5 Bar

By comparing the flow features, it seems that the mass flow rate didn't change compared to 1-Bar version. This behavior is not normal and it's probably due to a choke effect. If the flow is choked, Case I should be recalculated using 5 and 10 bars for back pressure. In case of a choked flow, the results cannot be considered correct. Also, the cavitation number has been reduced significantly resulting to potentially lower or non-existed cavitation inception.

$$\begin{cases} \dot{m}_{fl} = 0.36\ Kg/s \\ CD = 0.6 \\ CN = 9.5 \end{cases}$$

By reviewing the figures below, no significant change compared to 1-Bar case can be found. Cavitation inception still appears both in bypass and main tubes. The velocity inside the bypass tubes is still too high at the exit resulting a jet stream coming out of the tube while the velocity at the main tube was reduced significantly which minimize the jet effect.

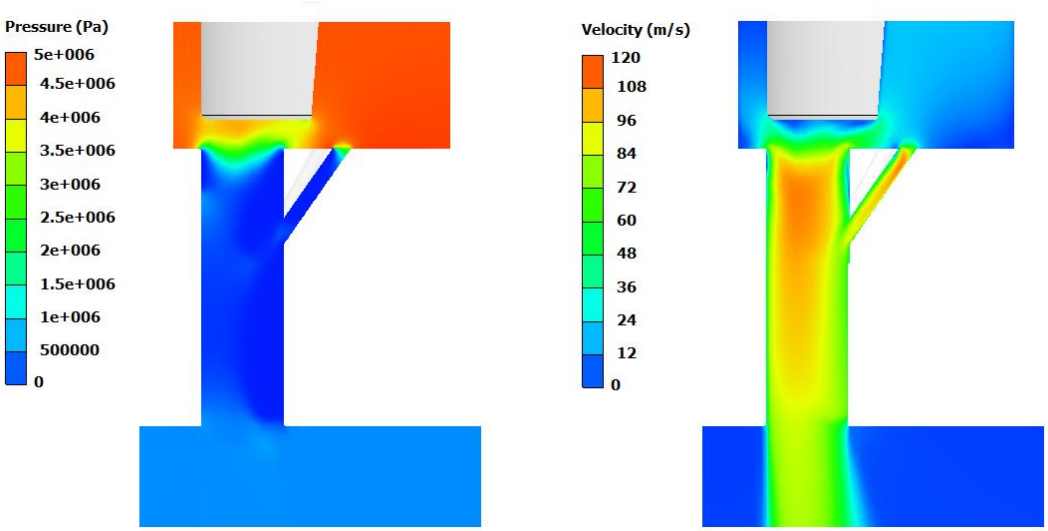

Figure 6.30 Case V (5 Bar): (a) Pressure plot, (b) Velocity plot

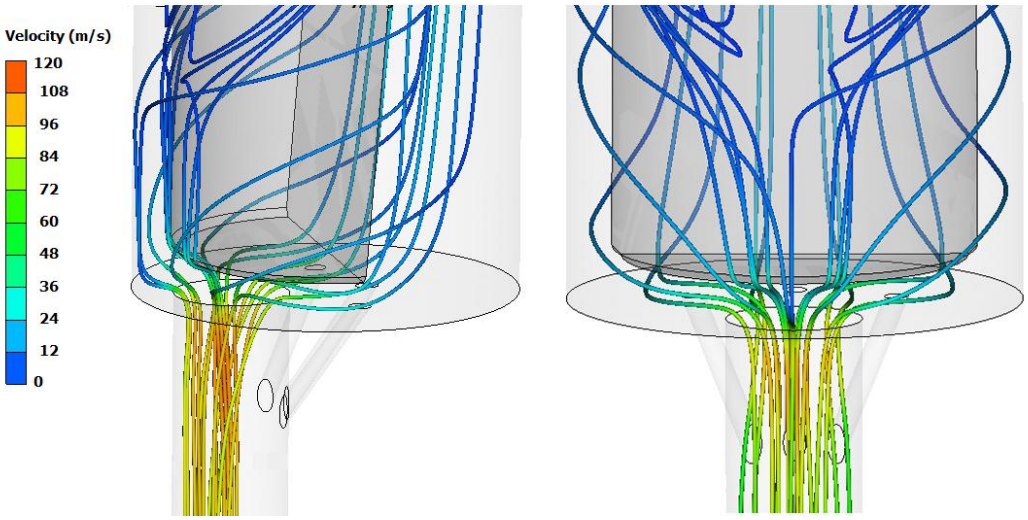

Figure 6.31 Case V (5 bar): Velocity stream lines

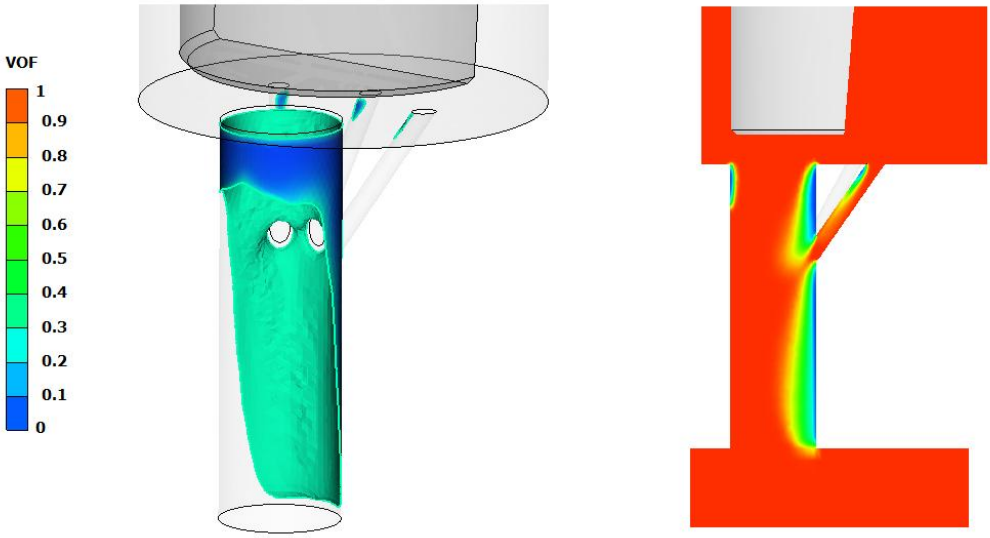

Figure 6.32 Case V (5 bar): (a) VOF IsoFun, (b) VOF plot

Back Pressure: 10 Bar

By using $10\ Bar$ as back pressure, it can be found that the cavitation number has reduced even further which indicates the probability of elimination of the cavitation inception. Although, mass flow rate has decreased only 2.5% compared to 1-Bar version that indicates that the assumption of a choked flow may be correct.

$$\begin{cases} \dot{m}_{fl} = 0.35\ Kg/s \\ CD = 0.58 \\ CN = 4 \end{cases}$$

As it can be seen in Figure 6.35, cavitation has been eliminated both inside bypass tubes and the main tube. Velocity in bypass tubes was reduced significantly, no longer generating a jet stream at the exit. Also, in Figure 6.36, it can be seen that as long as there is not a jet stream, coming out of the bypass tubes, the fluid coming out is carried away by the main flow. In result, the flow remains detached to the flow, eliminating cavitation inception at that point. Just above the bypass tube some traces of cavitation inception can be seen. This is something encouraging as it indicates that the actual reason cavitation inception stops is due to the added flow of the bypass tubes.

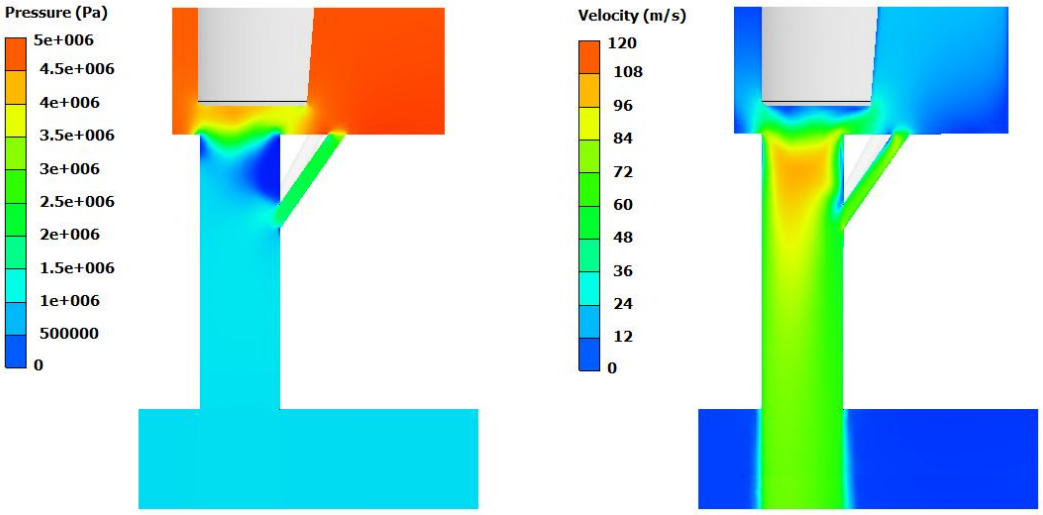

Figure 6.33 Case V (10 Bar): (a) Pressure plot, (b) Velocity plot

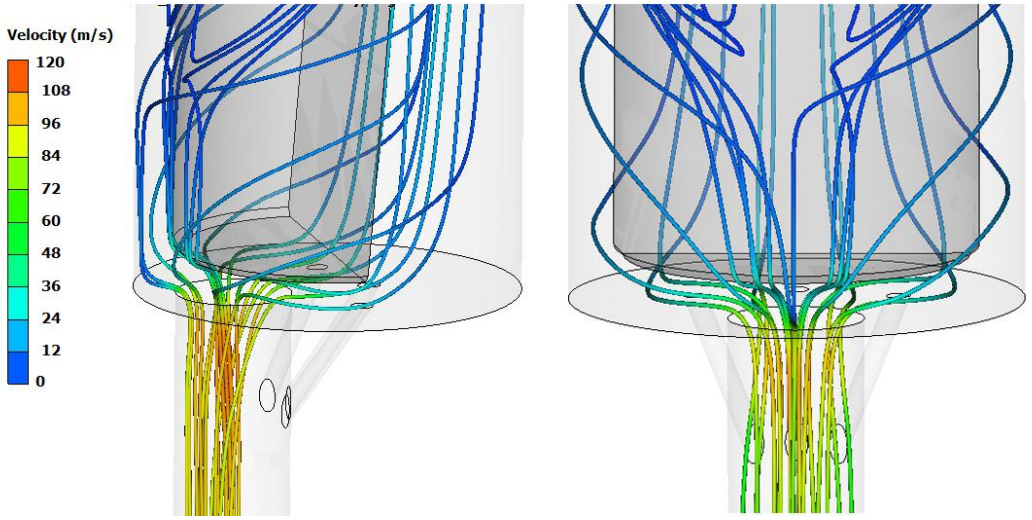

Figure 6.34 Case V (10 bar): Velocity stream lines

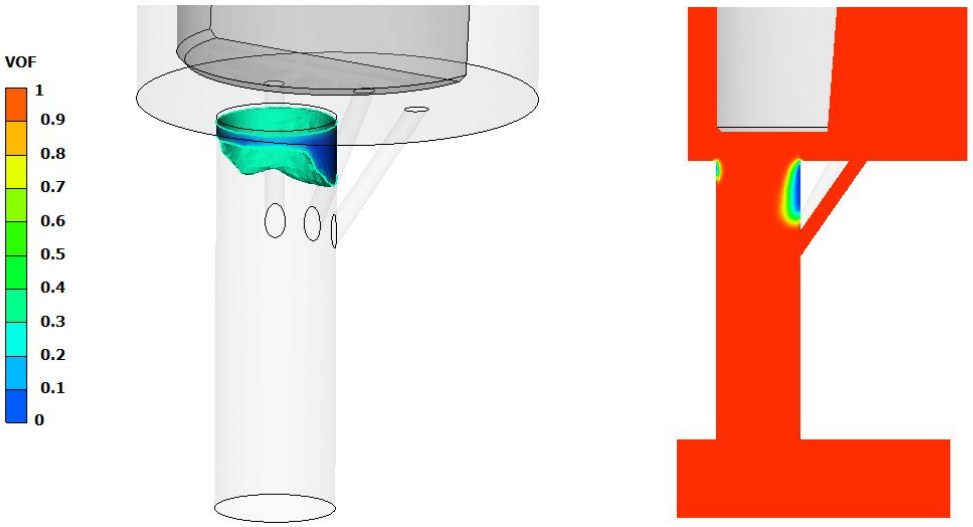

Figure 6.35 Case V (10 bar): (a) VOF IsoFun, (b) VOF plot

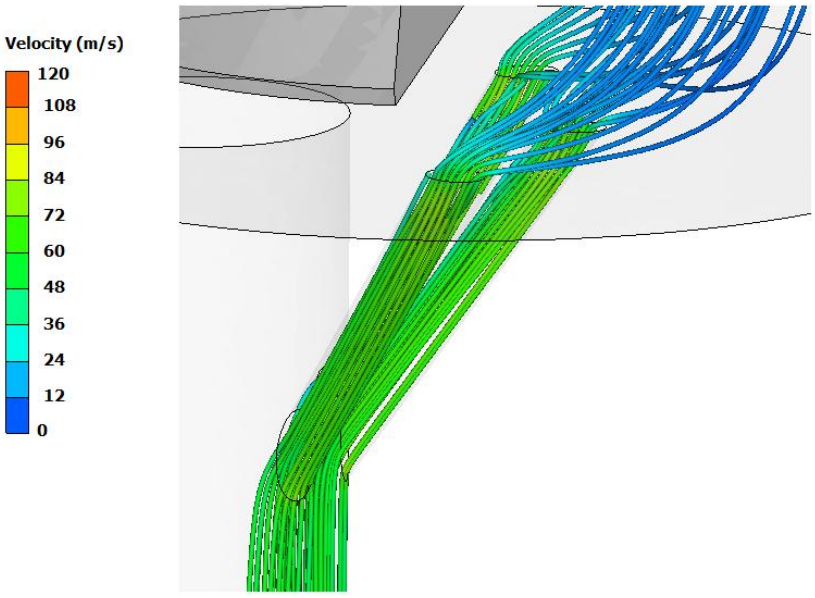

Figure 6.36 Case V (10 bar): Streamlines at bypass tubes

7 Conclusion

As it was known from the beginning that cavitation is a major issue in those prototype diesel fuel nozzles. At the initial case, cavitation inception was expected at the right side of the main tube. However, it was believed that one of the proposed cases was capable of eliminating cavitation inception.

The main reason that the expected results did not achieved is most likely the one explained in chapter 6.5.3. In case of a chocked flow, the mass flow rate is limited, thus the pressure drop did not affected by the introduction of bypass tubes. In result, the introduction of bypass tubes did not assist in a smother pressure transition. This assumption can be verified by comparing mass flow rates of case V with different back pressures. The mass flow rate remains the same despite the significant difference of inlet and outlet pressure. Also, the low CD number in every case indicates that the actual mass flow rate is much smaller compared to the calculated one.

In reality, the observation of those two variables cannot provide incontrovertible evidence that the choked flow is the reason that the geometries that used did not acted as expected. Further research has to be done, especially at the initial case with different back pressures.

Furthermore, according to case V (10 bar) simulation, it can be pointed out that the initial thought concerning ways to stop cavitation inception was correct. However, the geometry itself, introduced an unexpected factor that was not taken into account from the beginning.

In conclusion, it is safe to assume that that kind of geometry cannot be used for an extended analysis. Another geometry model should be used which will not interfere with the mass flow rate. Thus, by using that geometry the elimination of cavitation inception most likely cannot be achieved.

References

Abdulmouti, Hassan. 2014. Bubbly Two-Phase Flow: Part II- Characteristics and Parameters. *American Journal of Fluid Dynamics.* Scientific & Academic Publishing, 2014, Vol. 4, pp. 115-180. doi:10.5923/j.ajfd.20140404.01.

Anderson Jr., John D. 2010. *Fundamentals of Aerodynamics.* 5th Edition. New York : McGraw-Hill, 2010. pp. 98-116, 160-169, 180-182, 206-210. 0073398101.

Bakker, André. 2006. *Computational Fluid Dynamics.* [Presentation] Hanover : Dartmputh College, 2006. Lecture Notes.

Bergman, Theodore L., et al. 2011. *Fundamentals of Heat and Mass Transfer.* 7th Edition. s.l. : Wiley, 2011. pp. 400-413. 0470501979.

Borgnakke, Claus and Sonntag, Richard E. 2008. *Fundamentals of Thermodynamics.* 7th Edition. Michigan City : Wiley, 2008. pp. 13-17. 0470041927.

Brennen, Christopher Earls. 1995. *Cavitation and Bubble Dynamics.* Oxford : Oxford University Press, 1995. pp. 48-59, 80-93. 0195094093.

Brennen, Cristopher Earls. 2005. *Fundamentals of Multiphase Flows.* Pasadena : Cambridge University Press, 2005. pp. 100-120. 0521848040.

Chen, Ching-Jen. 1997. *Fundamentals Of Turbulence Modelling.* s.l. : CRC Press, 1997. pp. 3-6. 1560324058.

Fluent Inc. 2006. *Fluent 6.3 User Manual.* Lebanon : s.n., 2006. pp. 12.1 - 12.61.

Fox, Robert W., McDonald, Alan T. and Pritchard, Philip J. 2005. *Introduction to Fluid Mechanics.* 6th Edition. Washington City : Wiley, 2005. pp. 36-40. 0471735582.

Franc, Jean Pierre and Marie, Jean Michel. 2005. *Fundamentals of Cavitation.* 2004 Edition. New York : Kluwer Academic Publishers, 2005. pp. 16-31. 1402022328.

Franc, Jean Pierre. 2008. Fluid Dynamics of Cavitation and Cavitating Turbopumps: The Rayleigh-Plesset equation: a simple and powerful tool. *International Centre for Mechanical Sciences.* March 11, 2008, 496, pp. 1-9.

—. 2006. *Physics and Control of Cavitation.* Grenoble : University of Grenoble, 2006. pp. 9-24.

Granger, Rober A. 1995. *Fluid Mechanics.* s.l. : Dover Publications, 1995. pp. 422-425. 0486683567.

Henk, K. Versteeg and Malalasekera, Weeratunge. 1995. *An Introduction to Computational Fluid Dynamics - The Finite Volume Method.* London : Longman Scientific & Technical, 1995. pp. 5-83. 0582218845.

Koronakis, Periklis. 2001. *Applied Fluid Dynamics.* 2nd Edition. Athens : ION, 2001. σσ. 131-141. 9604114735.

—. 2009. *Fluid Mechanics.* 3rd Edition. Athens : ION, 2009. pp. 85-118. 9604114727.

Kuiper, G. 2012. *Cavitation on Ship Propellers.* Delf : TU Delf, 2012. pp. 37-46.

Obreschkow, Danail, Bruderer, Martin and Farhat, Mohamed. 2012. Analytical Approximations for the Collapse of an Empty Spherical Bubble. *Physical Review E.* 6, June 5, 2012, Vol. I, 85. arXiv:1205.4202 doi:10.1103/PhysRevE.85.066303.

Patankan, Suhas V. 1980. *Numerical Heat Transfer and Fluid Flow.* New York : CRC press, 1980. p. 102. 0891165223.

Plesset, Milton Spinoza and Hsieh, Din-Yu. 1960. Theory of Gas Bubble Dynamics in Oscillating Pressure Fields. *Physics of Fluids.* Fluid Dynamics, 1960, 3, pp. 882-892.

Salim, Salim Mohamed, Ariff, Mohd and Cheaf, Siew-Cheong. 2009. Wall y+ approach for dealing with turbulent flow over a surface mounted cube. *Seventh International Conference on CFD in the Minerals and Process Industries.* CSIRO, December 9-11, 2009, pp. 1-4.

Tanehill, John C., Anderson, Dale A. and Pletcher, Richard H. 1997. *Computational Fluid Mechanics and Heat Transfer.* 2nd Edition. London : Taylor & Francis, 1997. pp. 45-76. 156032046X.

White, Frank M. 2010. *Fluid Mechanics.* 7th Edition. Providence : McGraw, 2010. pp. 48-50. 0077422414.

Young, Donald F., et al. 2010. *A Brief Introduction To Fluid Mechanics.* 5th Edition. Jefferson City : Wiley, 2010. pp. 116-120. 0470596791.

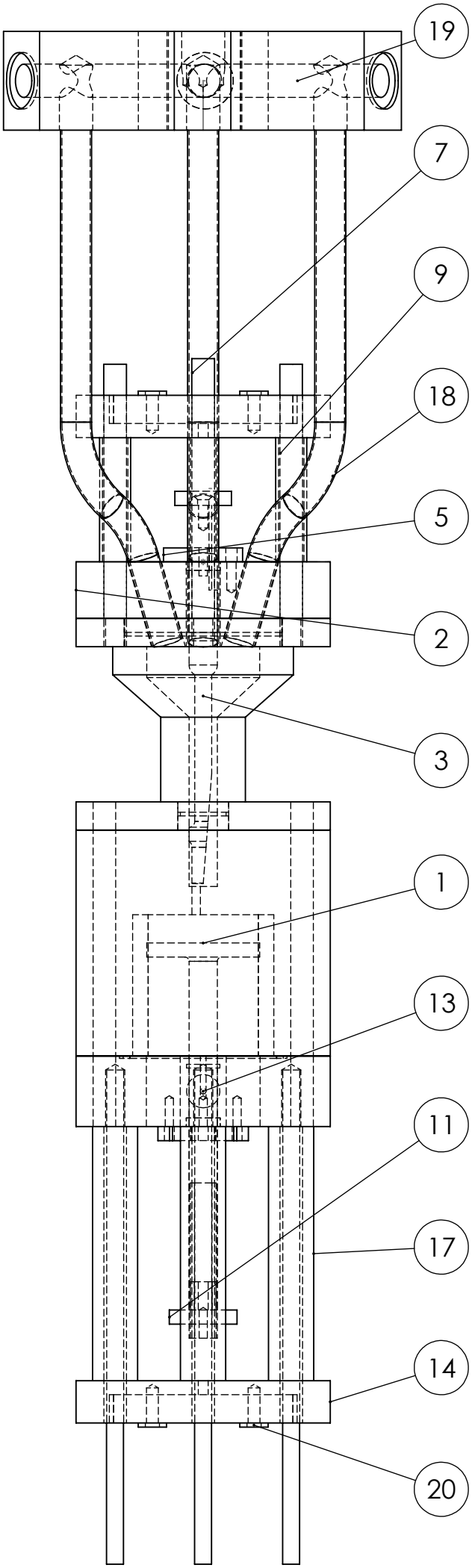

ITEM NO.	PART	QTY.
1	Chamber	1
2	Entrance	1
3	Entrance Shell	1
4	Needle	1
5	Needle Lock	1
6	Washer Spring	1
7	Holder 1	3
8	Vernier Holder	1
9	Spacer 2	3
10	440Z-3L Micrometer	2
11	Bolt	1
12	Holder 2	3
13	Micrometer Plate	1
14	Mount	1
15	Needle Lock 2	1
16	Sample Holder	1
17	Spacer 1	3
18	Pipe	3
19	Manifold	1
20	Holder 3	4

INSTITUTION:

City University London
Pireaus University of Applied Science

TITLE:

Cavitation Test Rig

DWG:

Rig Assembly

A4

SCALE:1:2

SHEET 1 OF 20

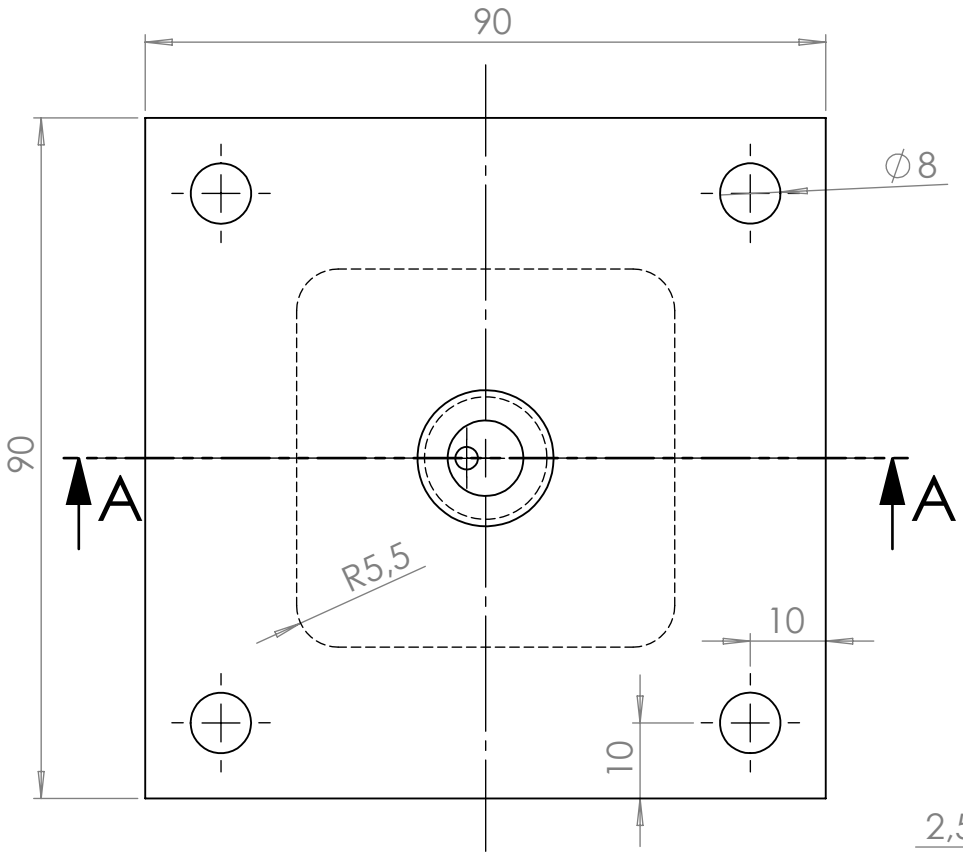

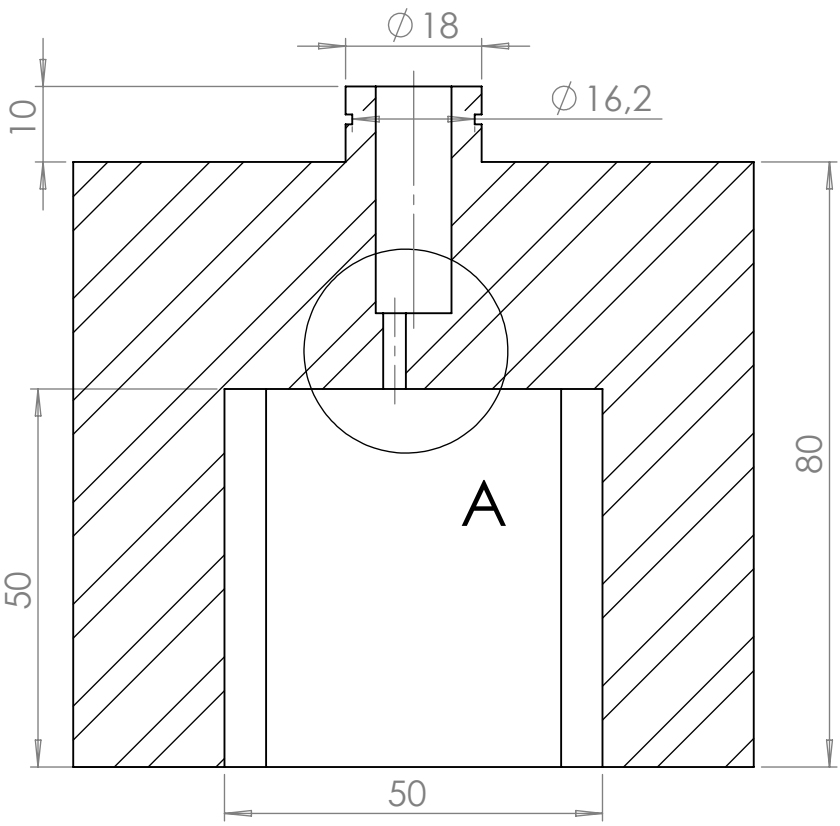

SECTION A-A

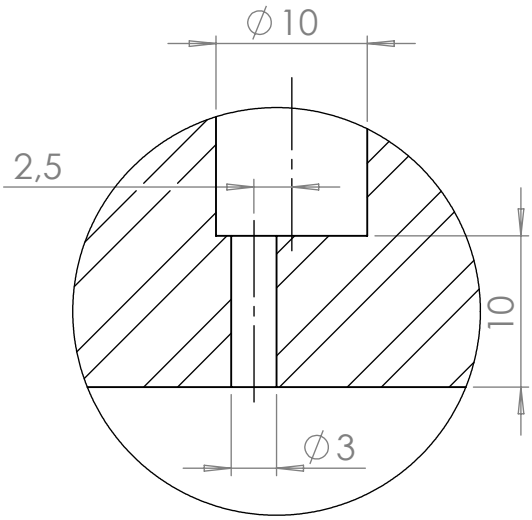

DETAIL A
SCALE 2 : 1

INSTITUTION:
City University London
Pireaus University of Applied Science

TITLE:
Cavitation Test Rig

DWG: Chamber

A4

V. 1

SCALE:1:1

SHEET 2 OF 20

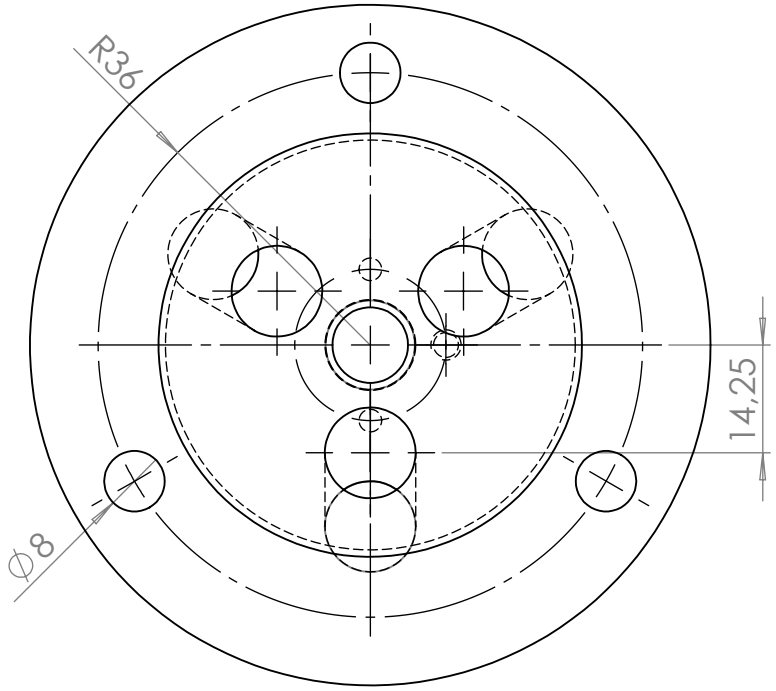

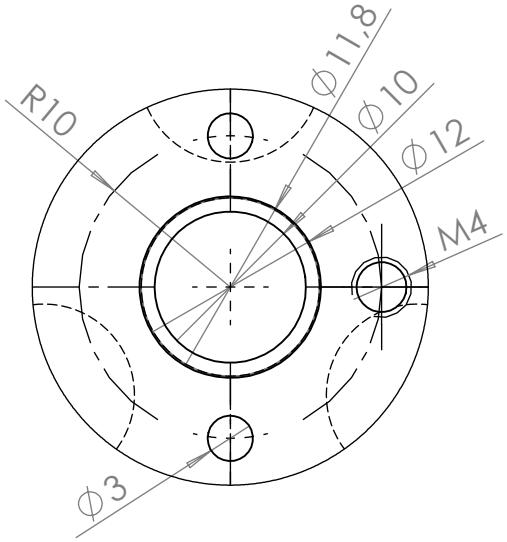

DETAIL B
SCALE 2 : 1

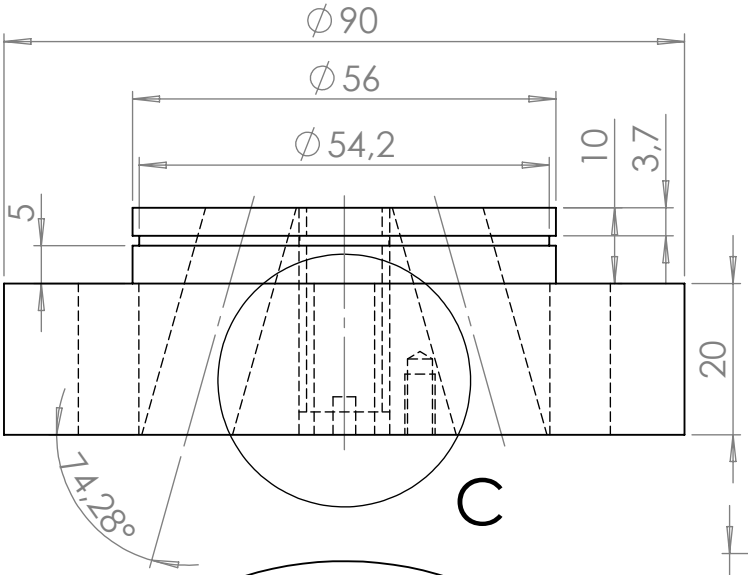

C

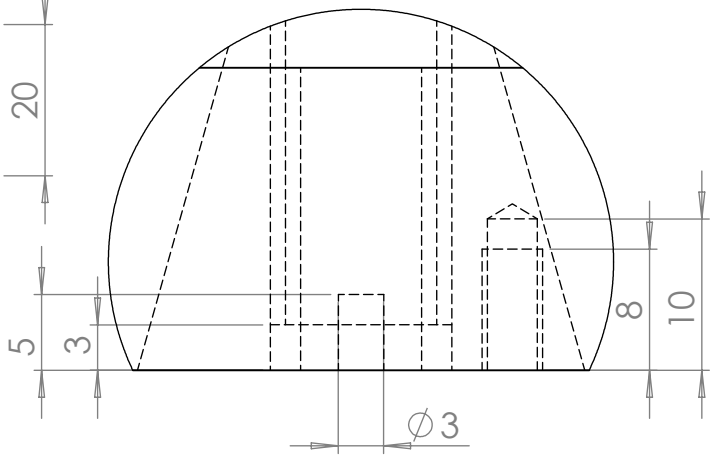

DETAIL C
SCALE 2 : 1

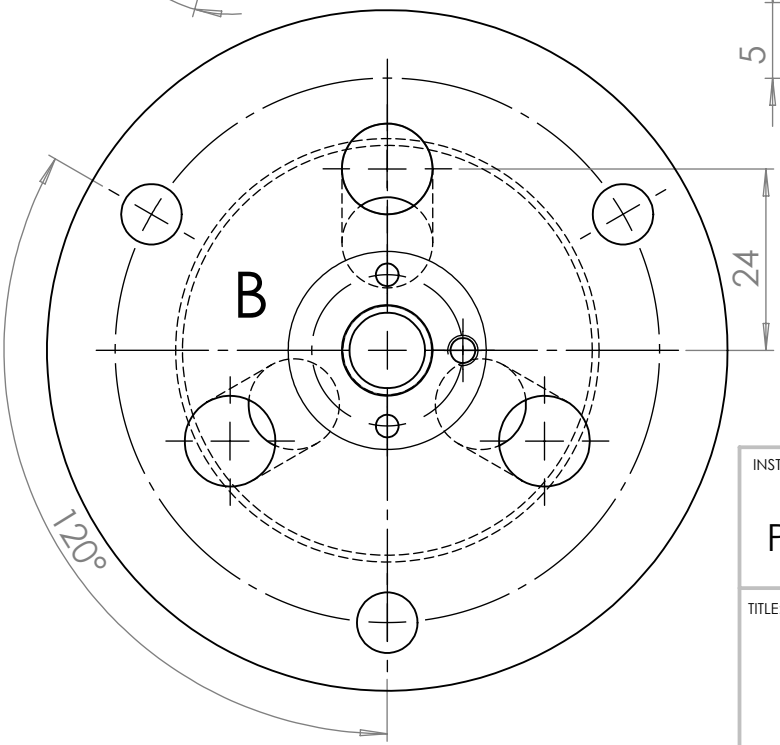

INSTITUTION:
City University London
Pireaus University of Applied Science

TITLE:
Cavitation Test Rig

DWG:
Entrance

A4

SCALE:1:1

SHEET 3 OF 20

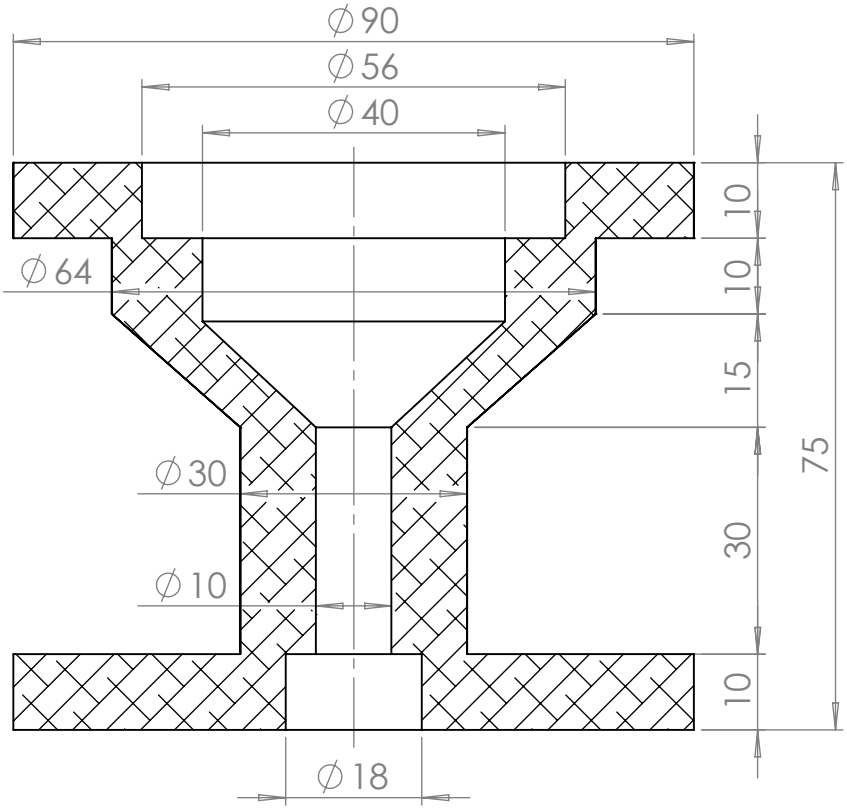

SECTION B-B

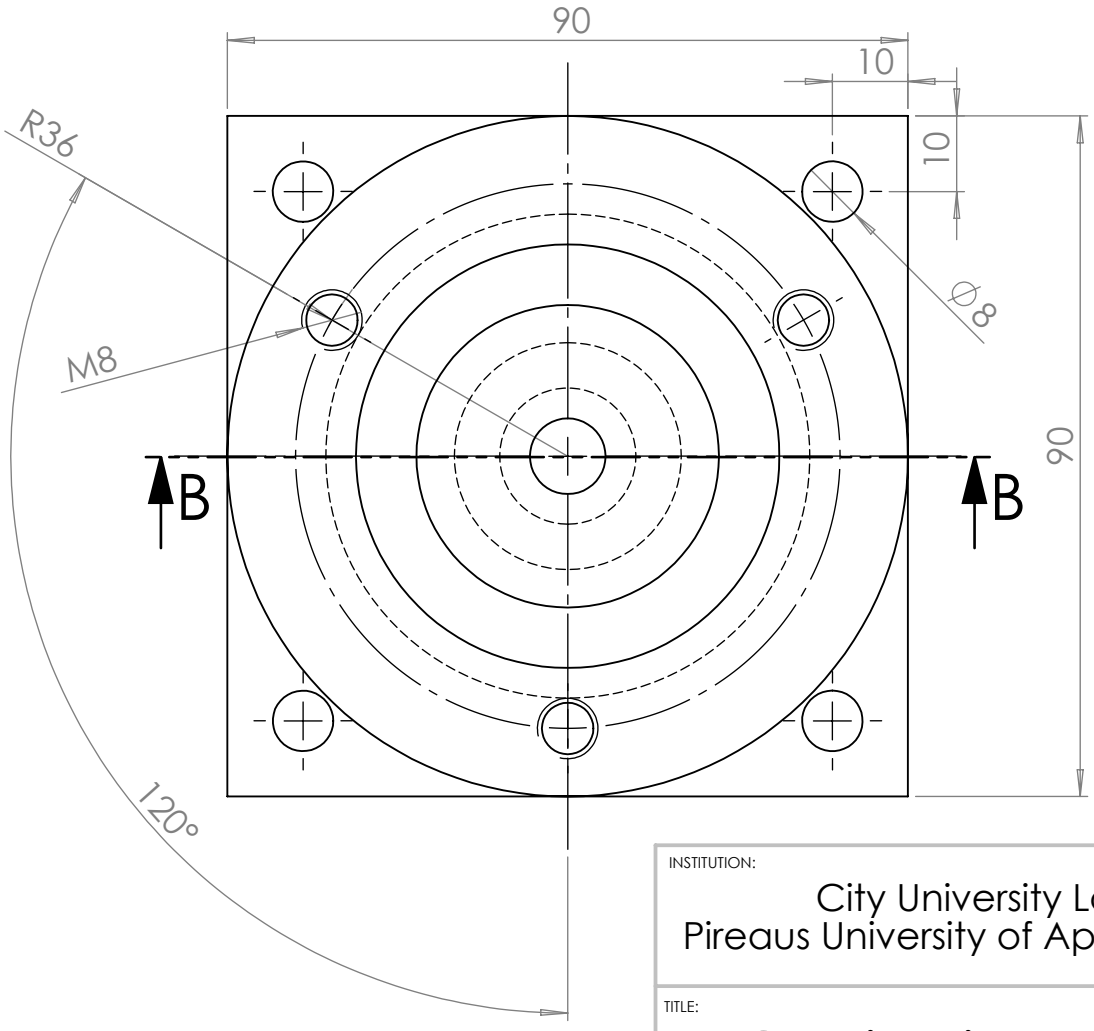

INSTITUTION:

City University London
Pireaus University of Applied Science

TITLE:

Cavitation Test Rig

DWG:

Entrance Shell

A4

SCALE:1:1

SHEET 4 OF 20

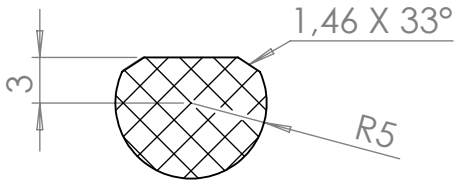

SECTION C-C
SCALE 2 : 1

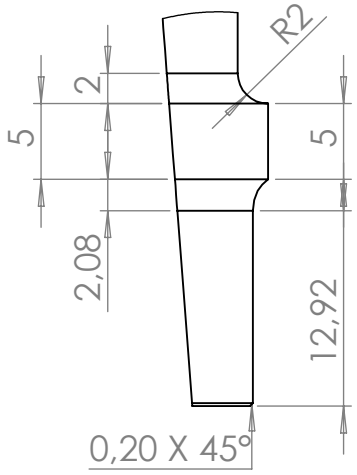

DETAIL D
SCALE 2 : 1

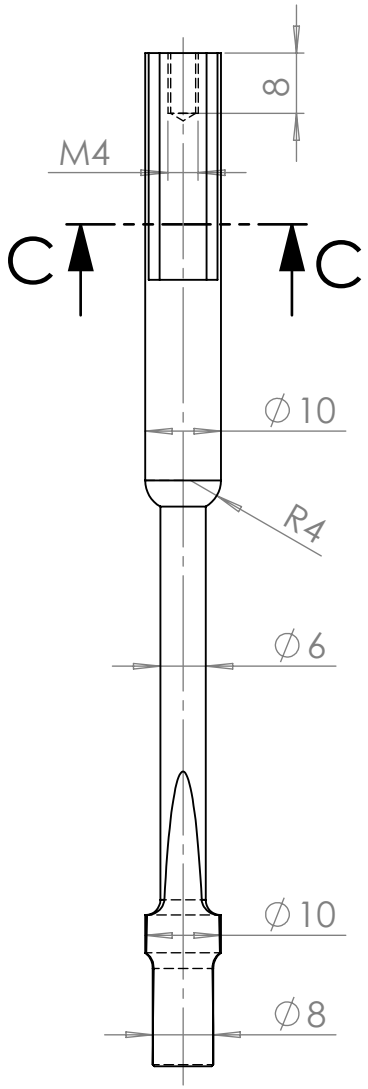

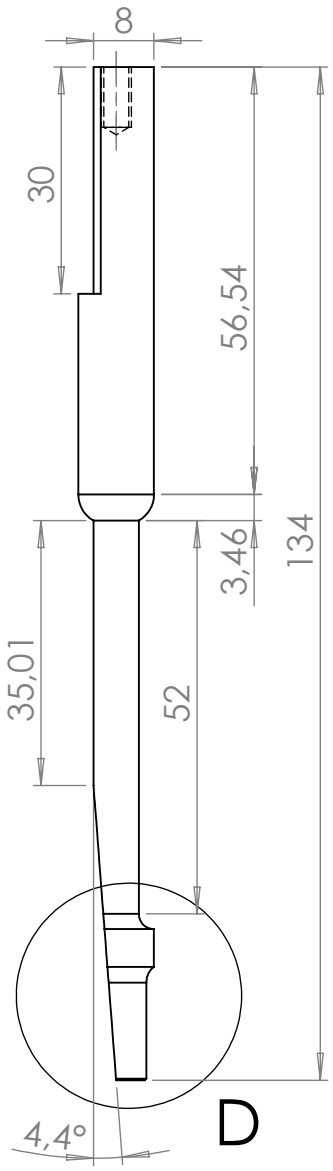

INSTITUTION:
City University London
Pireaus University of Applied Science

TITLE:
Cavitation Test Rig

DWG:
Needle

A4

SCALE:1:1

SHEET 5 OF 20

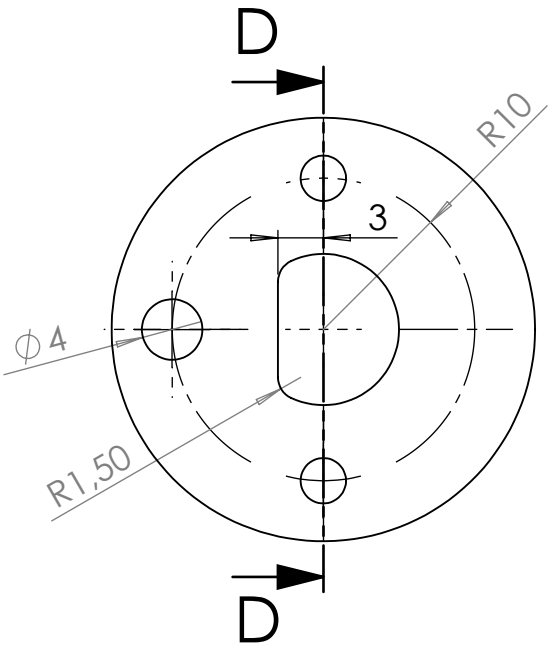

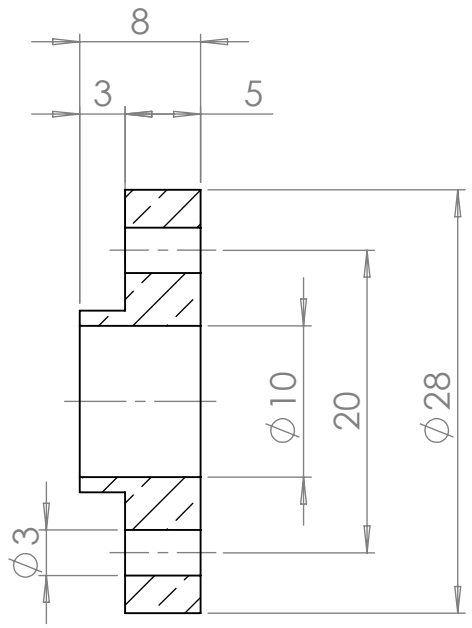

SECTION D-D

INSTITUTION:

City University London
Pireaus University of Applied Science

TITLE:

Cavitation Test Rig

DWG:

Needle Lock

A4

SCALE:2:1

SHEET 6 OF 20

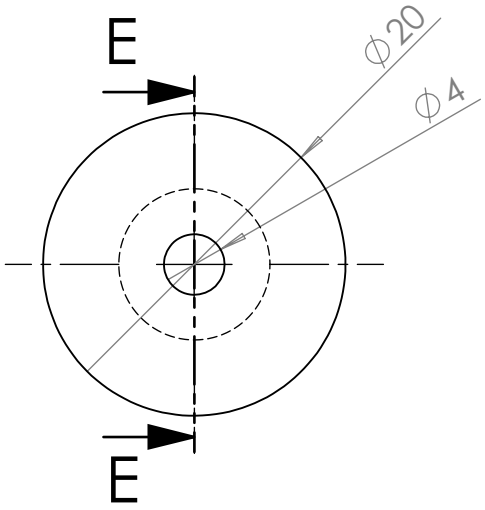

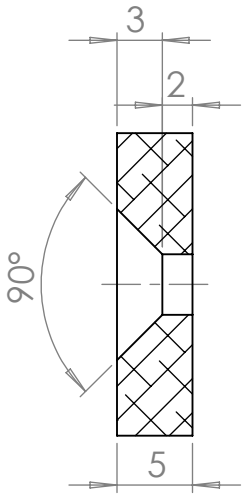

SECTION E-E

INSTITUTION:
City University London
Pireaus University of Applied Science

TITLE:
Cavitation Test Rig

DWG:
Washer Spring

A4

SCALE:2:1

SHEET 7 OF 20

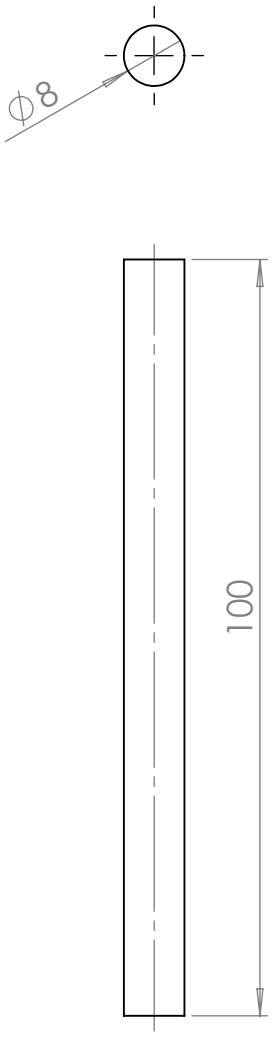

INSTITUTION:

City University London
Pireaus University of Applied Science

TITLE:

Cavitation Test Rig

DWG:

Holder 1

A4

SCALE:1:1

SHEET 8 OF 20

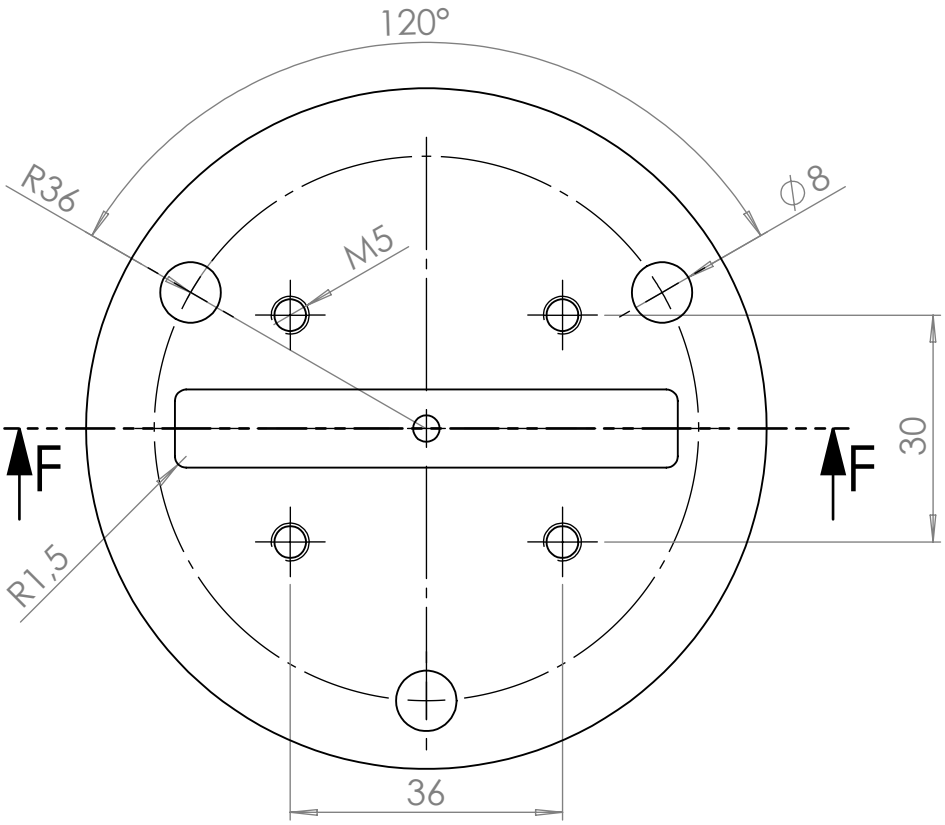

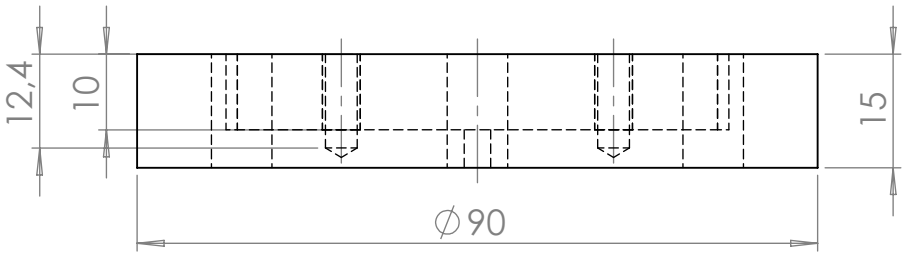

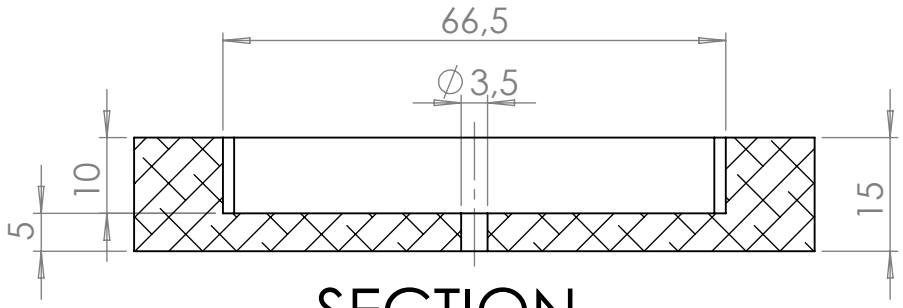

SECTION F-F

INSTITUTION:

City University London
Pireaus University of Applied Science

TITLE:

Cavitation Test Rig

DWG:

Vernier Holder

A4

SCALE:1:1

SHEET 9 OF 20

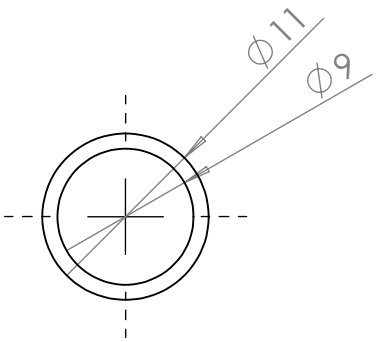

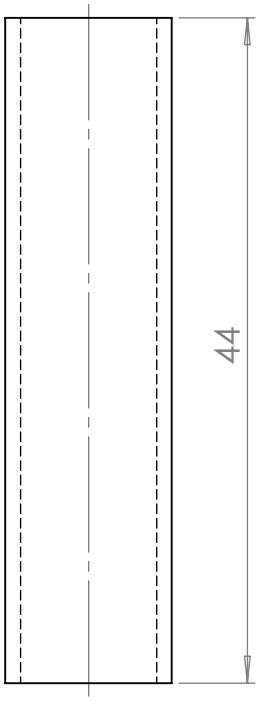

INSTITUTION:

City University London
Pireaus University of Applied Science

TITLE:

Cavitation Test Rig

DWG:

Spacer 2

A4

SCALE:2:1

SHEET 10 OF 20

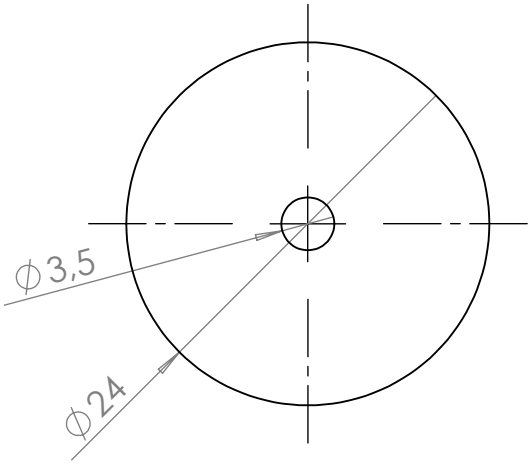

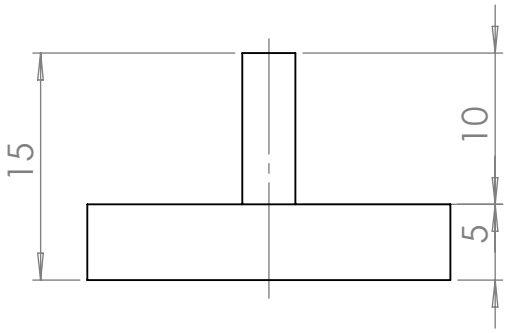

INSTITUTION:

City University London
Pireaus University of Applied Science

TITLE:

Cavitation Test Rig

DWG:

Bolt

A4

SCALE:2:1

SHEET 11 OF 20

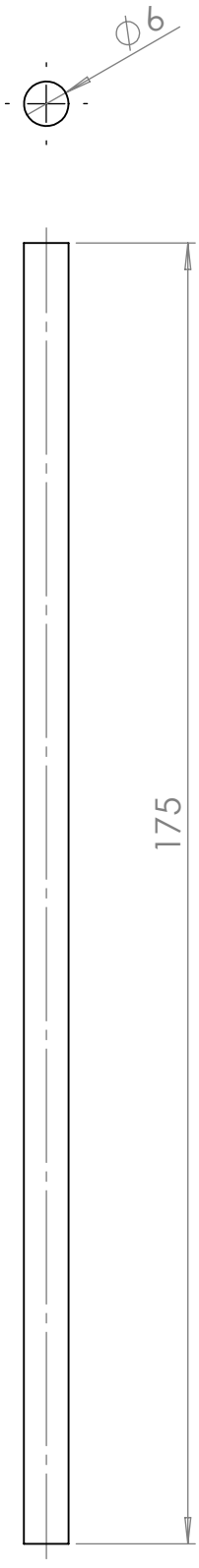

INSTITUTION:

City University London
Pireaus University of Applied Science

TITLE:

Cavitation Test Rig

DWG:

Holder 2

A4

SCALE:1:1

SHEET 12 OF 20

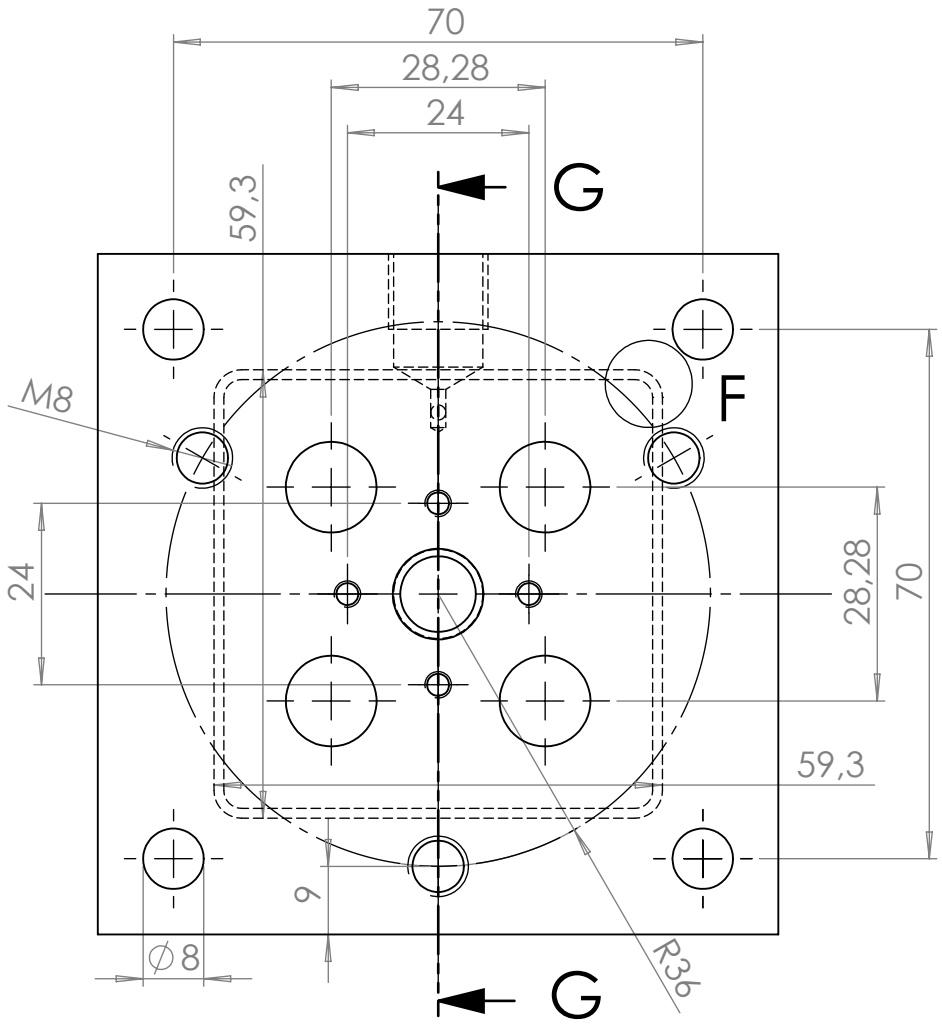

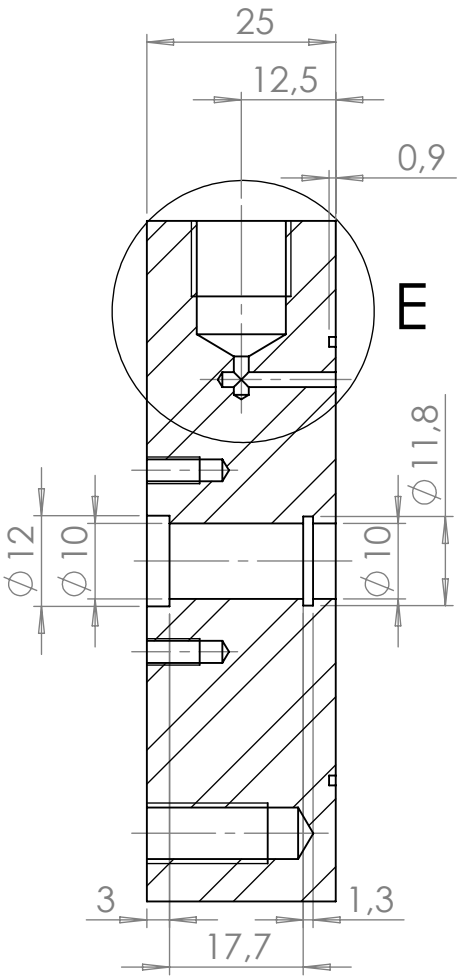

SECTION G-G

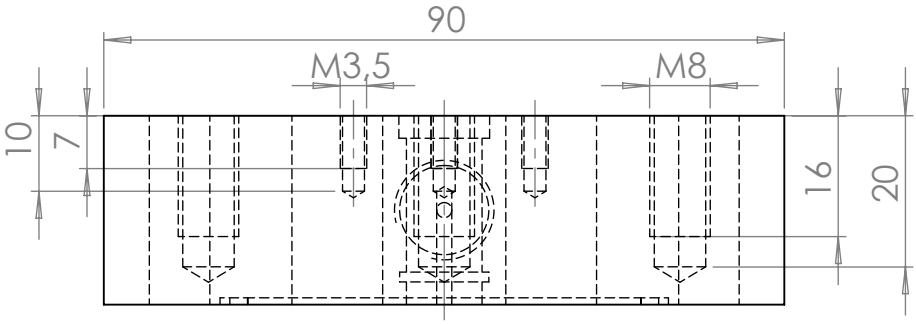

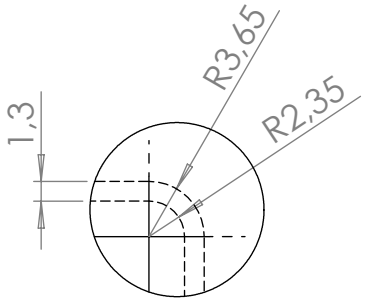

DETAIL F
SCALE 2 : 1

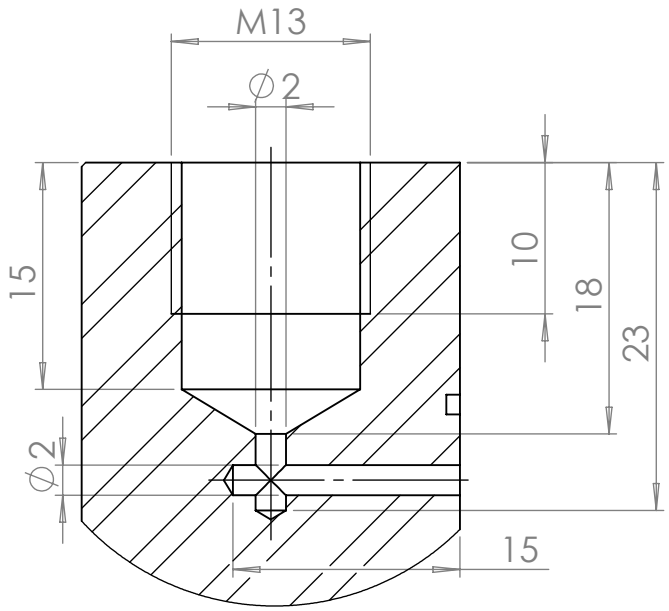

DETAIL E
SCALE 2 : 1

INSTITUTION:
City University London
Pireaus University of Applied Science

TITLE:
Cavitation Test Rig

DWG: Micrometer Plate

A4

SCALE:1:1

SHEET 13 OF 20

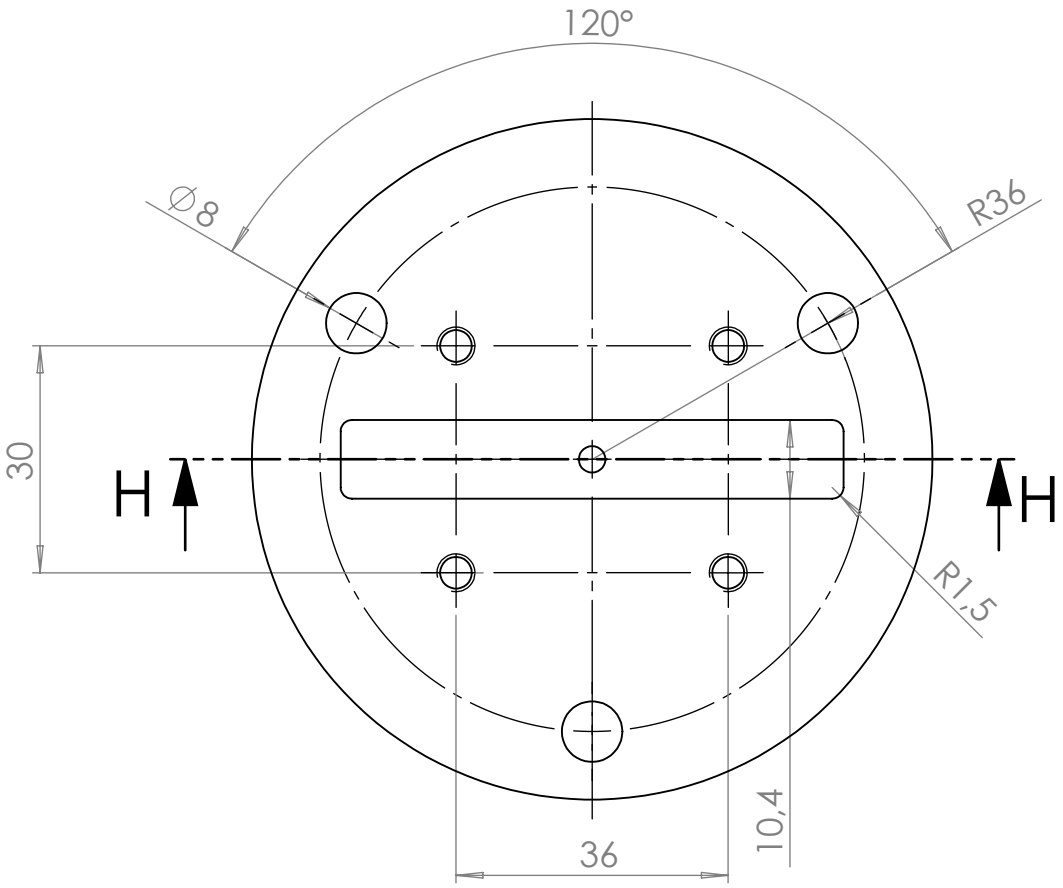

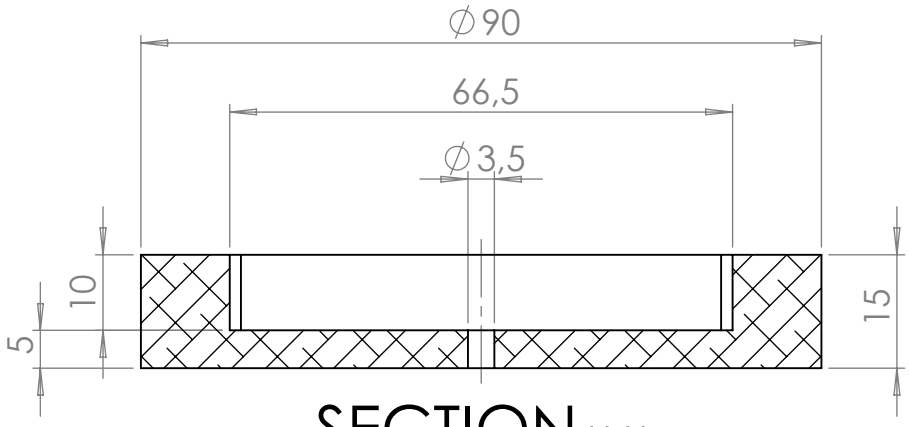

SECTION H-H

INSTITUTION:

City University London
Pireaus University of Applied Science

TITLE:

Cavitation Test Rig

DWG:

Mount

A4

SCALE:1:1

SHEET 14 OF 20

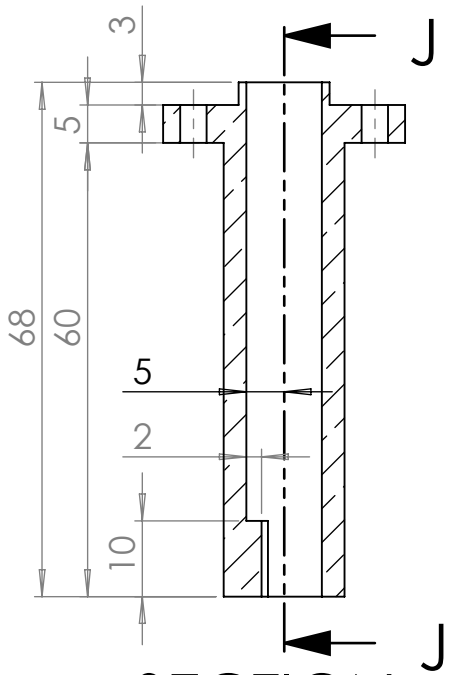

SECTION I-I

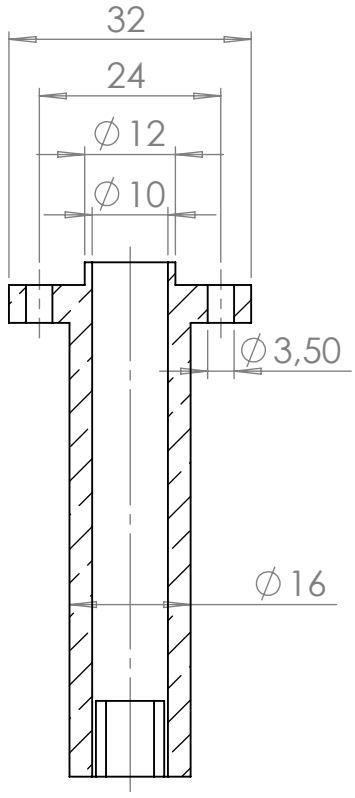

SECTION J-J

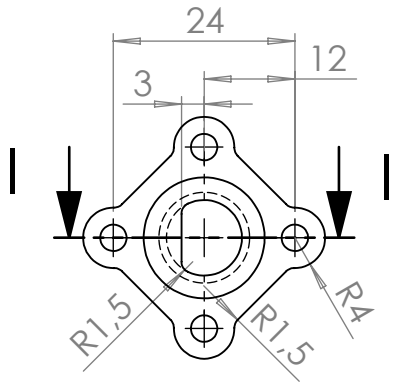

INSTITUTION:
City University London
Pireaus University of Applied Science

TITLE:
Cavitation Test Rig

DWG:
Needle Lock 2

A4

SCALE:1:1

SHEET 15 OF 20

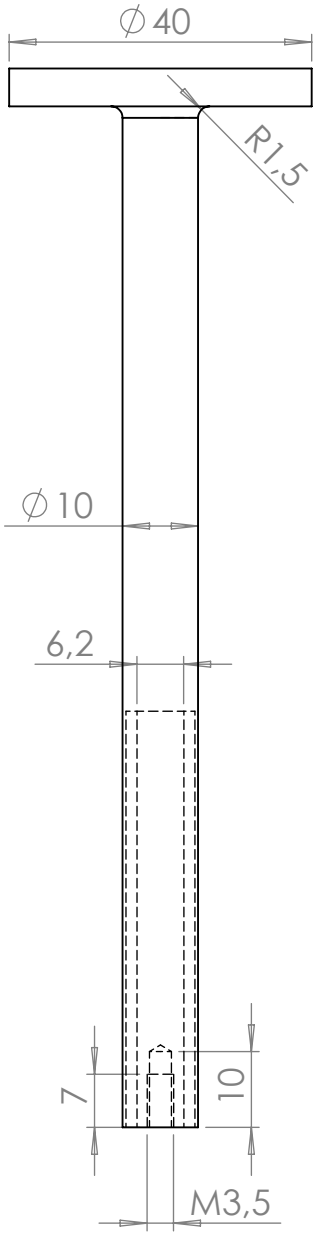

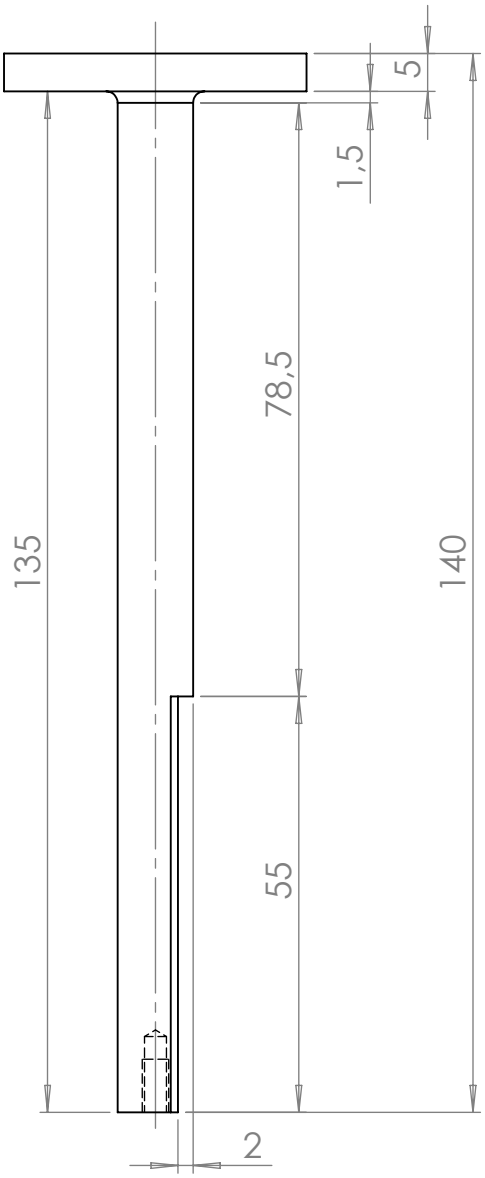

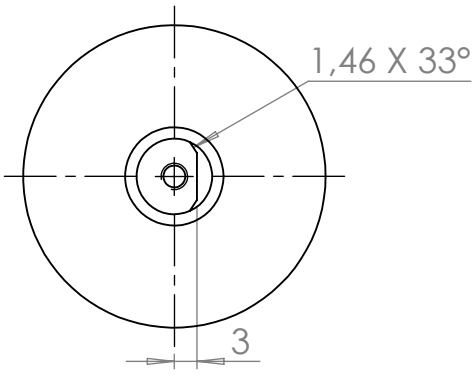

INSTITUTION:

City University London
Pireaus University of Applied Science

TITLE:

Cavitation Test Rig

DWG:

Sample Holder

A4

SCALE:1:1

SHEET 16 OF 20

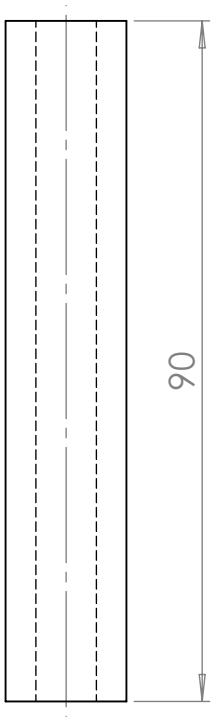

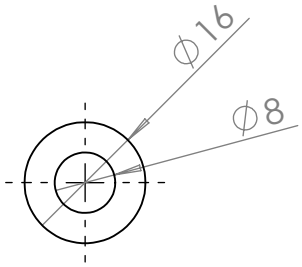

INSTITUTION:

City University London
Pireaus University of Applied Science

TITLE:

Cavitation Test Rig

DWG:

Spacer 1

A4

SCALE:1:1

SHEET 17 OF 20

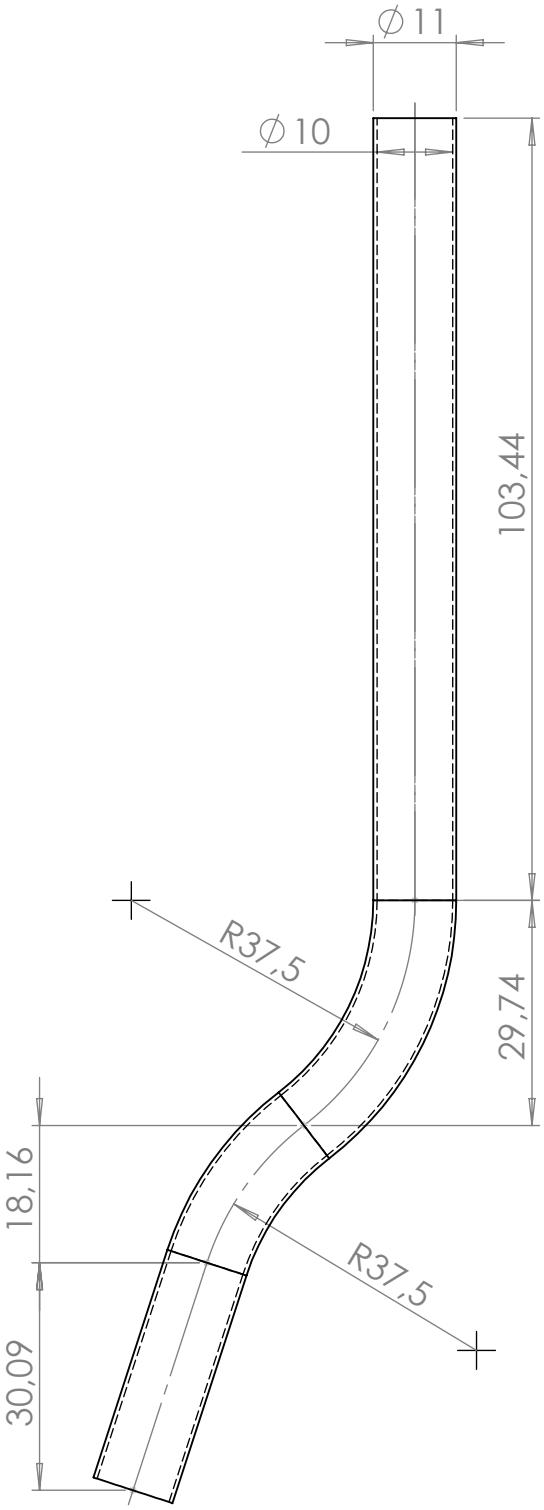

INSTITUTION:

City University London
Pireaus University of Applied Science

TITLE:

Cavitation Test Rig

DWG:

Pipe

A4

SCALE:1:1

SHEET 18 OF 20

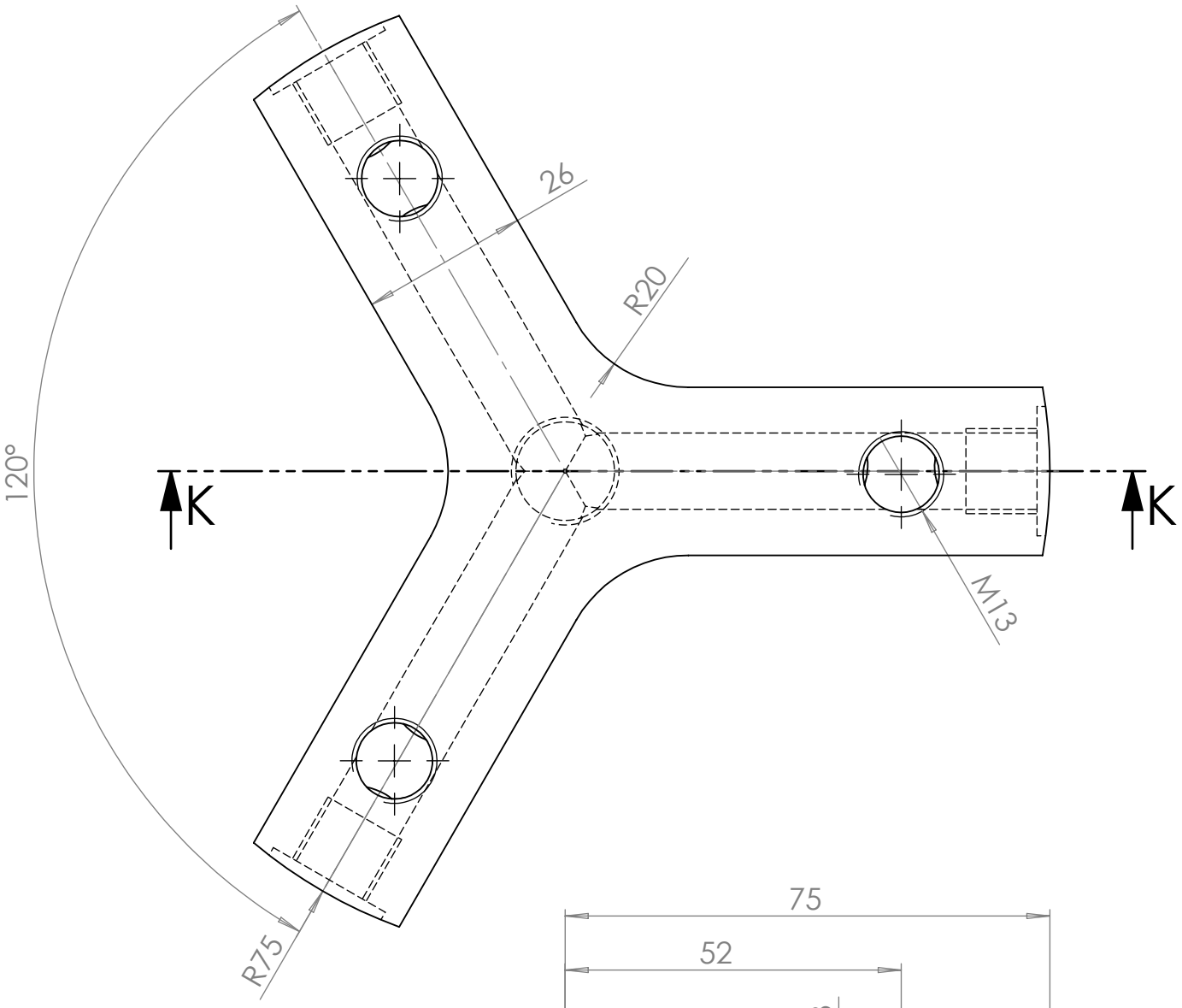

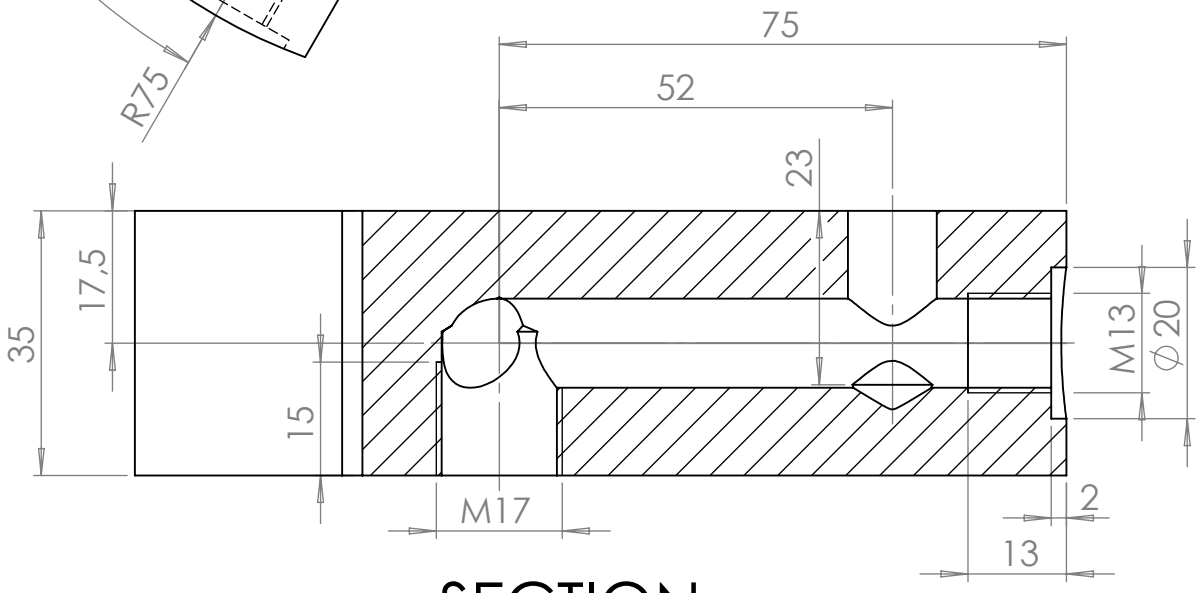

SECTION K-K

INSTITUTION:

City University London
Pireaus University of Applied Science

TITLE:

Cavitation Test Rig

DWG:

Manifold

A4

SCALE:1:1

SHEET 19 OF 20

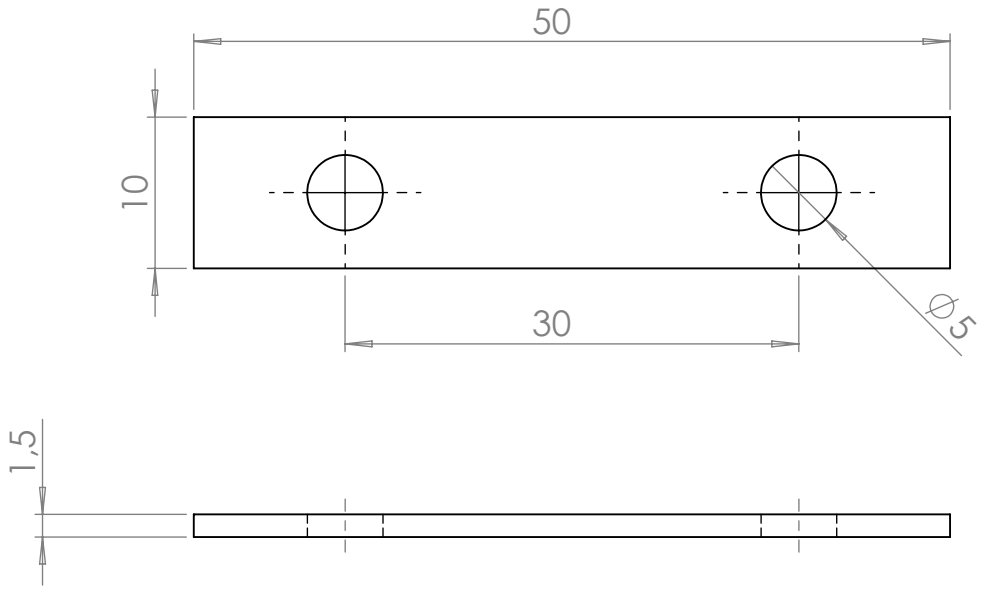

INSTITUTION:

City University London
Pireaus University of Applied Science

TITLE:

Cavitation Test Rig

DWG:

Holder 3

A4

SCALE:2:1

SHEET 20 OF 20